ACSNANO

www.acsnano.org

REVIEW

Nanoparticle Ex-solution for Supported Catalysts: Materials Design, Mechanism and Future Perspectives

Jun Hyuk Kim,[‖] Jun Kyu Kim,[‖] Jiapeng Liu,[‖] Antonino Curcio, Ji-Soo Jang, Il-Doo Kim, Francesco Ciucci,* and WooChul Jung*

Cite This: *ACS Nano* 2021, 15, 81−110

Read Online

ACCESS | Metrics & More | Article Recommendations

ABSTRACT: **Supported metal catalysts represent one of the major milestones in heterogeneous catalysis. Such catalytic systems are feasible for use in a broad range of applications, including renewable energy devices, sensors, automotive emission control systems, and chemical reformers. The lifetimes of these catalytic platforms depend strongly on the stability of the supported nanoparticles. With this regard, nanoparticles synthesized *via* ex-solution process emphasize exceptional robustness as they are socketed in the host oxide. Ex-solution refers to a phenomenon which yields selective growth of fine and uniformly distributed metal nanocatalysts on oxide supports upon partial reduction. This type of advanced structural engineering is a game-changer in the field of heterogeneous catalysis with numerous studies showing the benefits of ex-solution process. In this review, we highlight the latest research efforts regarding the origin of the ex-solution phenomenon and the mechanism underpinning particle formation. We also propose research directions to expand the utility and functionality of the current ex-solution techniques.**

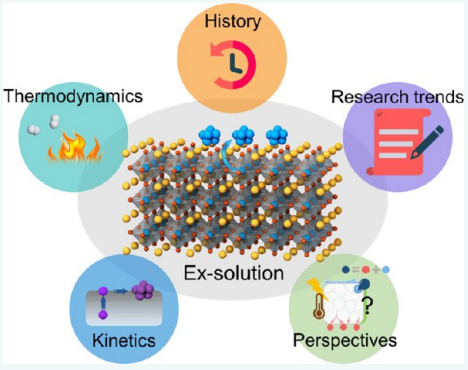

KEYWORDS: *ex-solution, nanoparticle, supported catalysts, heterogeneous catalysts, intelligent catalysts, reforming, coking tolerant, sulfur tolerant, anode, in situ growth*

INTRODUCTION

Supported catalysts are indispensable given their functions in multiple high-value catalytic processes, including those in petroleum refinery and for use in chemical fuel production, exhaust emission control, gas sensing, and energy storage and conversion, to mention a few.[1−9] In general, supported catalysts are configured as catalytically active metal particles dispersed on a functional oxide support. In a typical heterogeneous catalyst, most gas-phase reactions occur at the topmost layers of the atoms (*i.e.*, the metal−gas and metal−oxide−gas interfaces); therefore, increasing the surface area—to extend the reaction boundaries—is key to augment the catalytic activity. In this regard, making the metal particles smaller, preferably to nanoscale, is essential to secure a high surface-to-volume ratio, which draws the maximum economic utility out of the finite catalyst. Furthermore, it is of significance to ensure superior surface dispersion of nanoparticles across the support. Conventionally, this is done by impregnation, co-precipitation, or deposition techniques (*i.e.*, physical vapor deposition and chemical vapor deposition). Unfortunately, the metal nanoparticles produced with the aforementioned methods afford limited control over the size distributions, and the weak attachment between the support and metal nanoparticles often results in disappointing longevity of the catalytic system.

Alternatively, nanoparticles can be spontaneously yielded directly from the support through an "ex-solution" process (Figure 1). When certain catalytically active cations are dissolved into a supporting framework homogeneously in an oxidizing condition, they can be subsequently extruded as metallic nanoparticles upon a partial reduction process. Compared to traditional techniques, the ex-solution process offers better spreading of nanoparticles along with superior size

Received: August 24, 2020
Accepted: December 17, 2020
Published: December 28, 2020

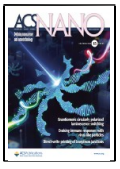

https://dx.doi.org/10.1021/acsnano.0c07105
ACS Nano 2021, 15, 81−110

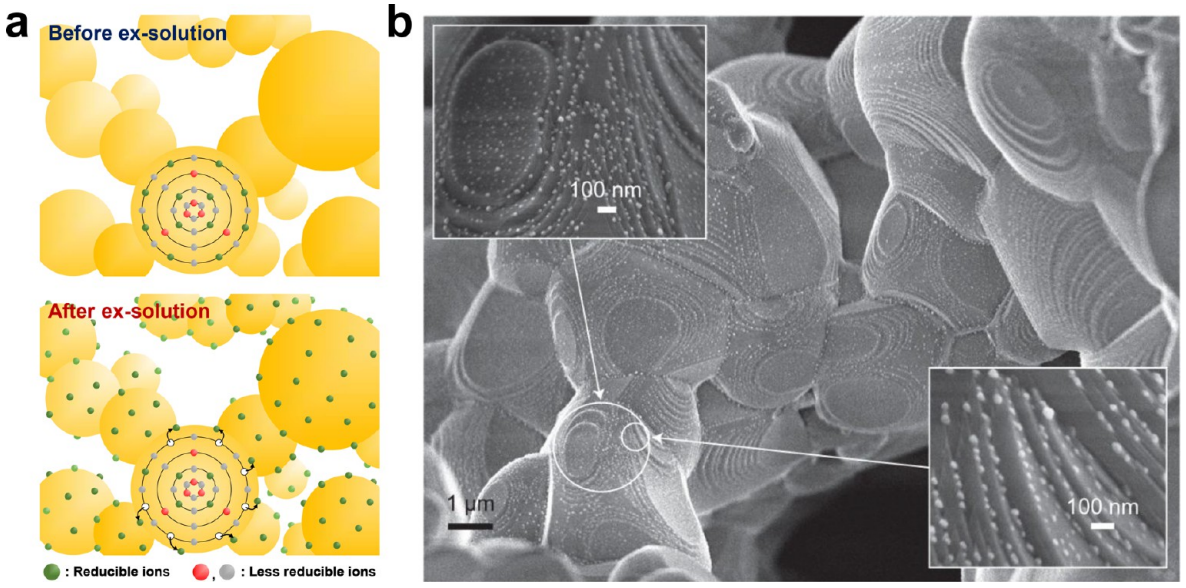

Figure 1. (a) Schematic illustration of structural evolution through the ex-solution process. Red, green, and gray balls represent different cations. Green is the most reducible ion. (b) Surface microstructure of $La_{0.8}Ce_{0.1}Ni_{0.4}Ti_{0.6}O_3$ after ex-solution by scanning electron microscope (SEM). The nanoparticles are uniformly distributed onto the supports. Panel b reprinted with permission from ref 14. Copyright 2013 Springer Nature.

uniformity and thus represents a salient advancement with regard to the preparation of best-in-class supported catalysts. Moreover, the simple and precise manufacturing methods used and the fascinating geometry of socket-anchored nanoparticles, bringing forth exceptional resistance to particle agglomeration and coking, clearly offer advantages and thus bode well for the future of heterogeneous catalysis.[10−13]

By employing the ex-solution process, significant progress has been made, especially with regard to the concept of intelligent catalysts and the development of electrodes for solid oxide electrochemical cells (SOCs). These efforts to create better SOC electrodes have been discussed at length in earlier reviews,[15−18] and interested readers are strongly encouraged to refer to the cited reviews. In this review, instead, we discuss comprehensively the current mechanistic understanding of the ex-solution phenomenon theoretically, considering atomistic and continuum models, and experimentally. Specifically, in Related Research Status, we start with a brief history of the ex-solution process, after which we overview the most important and cited studies and analyze the current research status. In Energetics and Dynamics of the Ex-solution Process, we focus on a more in-depth discussion of ex-solution energetics, the atomic origin of why ex-solution occurs, and the related dynamics and the mechanisms by which the ex-solution process proceeds. Finally, in Explaining, Why Does It Happen?, we present future perspectives on the road to expanding the utility of current ex-solution techniques, which therein includes multicomponent ex-solution processes, post-treatments, alternative attempts to obtain ex-solved particles, and computational perspectives for the material design and modeling.

RELATED RESEARCH STATUS

Originally, the term "ex-solution" was used in relation to earth sciences or mineralogy as a catch-all term related to how a homogeneous solid solution is separated into at least two different crystal structures. However, the ex-solution for the purposes of this work refers to the "selective emergence of metal nanoparticles on oxide supports upon partial reduction". Ex-solution in this sense began to be used frequently after the publishing of two monumental works by Irvine's group,[14,19] which is to tune the A-site deficiency in perovskite oxides to trigger more effective growth of metal nanoparticles. Indeed, the same phenomenon has been steadily reported in different terms thus far. For example, a concept similar to the ex-solution approach was introduced as an "internal solid-state reaction"[20] by Schmalzried and Backhaus-Ricoult, in the late 1900s (Figure 2a−c). The authors interpreted this phenomenon as chemical processes in isothermal heterogeneous systems when the reaction product (precipitates) forms in the interior of a solid. As shown in Figure 2a,b when using the (A,B)O oxide solid solution (AO is more reducible than BO), the point defect flux caused by the oxygen chemical potential difference between the external surface and the reaction front (*i.e.*, subsurface region) can form the reduced products (*i.e.*, metallic A) at the surface or in the bulk of the reactant solid solution. In particular, they classified these reactions into two types depending on whether or not the (sub)lattice of the matrix is destroyed, indicating that this is determined by the initial concentration of the reducible element, A, through a numerical calculation derived by local mass balance. Moreover, the authors have suggested that the reaction is also affected by the surface state (dense or porous), point defect concentration, mobility, and other factors. On the other hand, with regard to chemical catalysts, for example, exhaust gas emission systems, the term "intelligent catalysts" has been used to emphasize the reversibility of metal nanoparticles, in particular starting with a work reported by Nishihata *et al.*, in 2002.[6] This article reported the high durability of the $LaFe_{0.57}Co_{0.38}Pd_{0.05}O_3$ perovskite catalyst compared to the conventional impregnated Pd/Al_2O_3 type during the $CO-NO_x$ crossover point conversion lasting 100 h as shown in Figure 2d. Hence, they suggested that the reversible movement of Pd into and out of the perovskite lattice (dissolution and precipitation) suppresses Pd particle growth, leading to superior retention of

https://dx.doi.org/10.1021/acsnano.0c07105
ACS Nano 2021, 15, 81−110

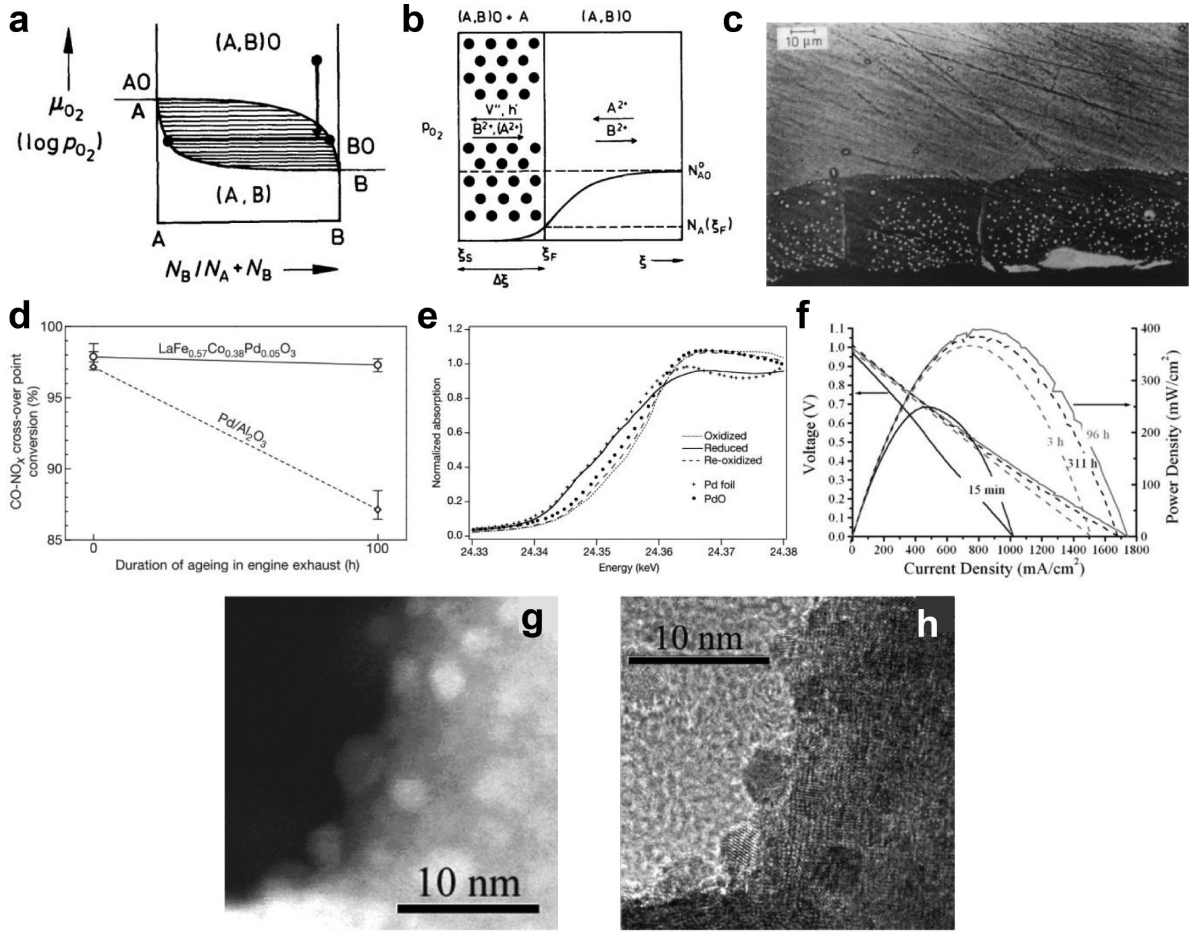

Figure 2. (a) Phase diagram and reaction path of internal solid-state reaction (in this case, internal reduction) in (A,B)O system. N_A and N_B are the numbers of A and B atoms (or ions), respectively; μ_{O_2} denotes the chemical potential of O_2; and p_{O_2} is the oxygen partial pressure. (b) Schematic of internal reduction mechanism. V″ is cation vacancy, $h^\bullet$ is hole, ζ refers the depth of oxide solid solution. ζ_S and ζ_F are the external surface and reaction fronts, respectively. (c) Scanning electron microscope images of $Mg_{0.97}Cu_{0.03}O$ after heat treatment at 1400 °C in C/CO-buffer gas for 9 h. (d) Stability tests of $LaFe_{0.57}Co_{0.38}Pd_{0.05}O_3$ and Pd/Al_2O_3 catalysts during conversion of three pollutants; carbon monoxide (CO), hydrocarbon, and nitrogen oxides (NO_x). (e) X-ray absorption near edge structure results of $LaFe_{0.57}Co_{0.38}Pd_{0.05}O_3$ and comparison with PdO and Pd foil as references. (f) *I*−*V* curves of typical solid oxide fuel cell using $La_{0.8}Sr_{0.2}Cr_{0.82}Ru_{0.18}O_{3-\delta}$ anode measuring various times after wet H_2 flow. (g, h) Scanning tunneling electron microscope and high-resolution tunneling electron microscope images of $La_{0.8}Sr_{0.2}Cr_{0.82}Ru_{0.18}O_{3-\delta}$ after reduction in H_2 for 45 h, respectively. Panels a−c reprinted with permission from ref 20. Copyright 1992 Elsevier. Panels d and e reprinted with permission from ref 6. Copyright 2002 Springer Nature. Panels f−h reprinted with permission from ref 22. Copyright 2007 Elsevier.

high catalyst activity (Figure 2e). Other terms used to describe the ex-solution are the "solid-phase crystallization" (spc) method by Takehira.[21] They prepared both perovskite- and hydrotalcite-type catalysts through the spc method and compared the catalytic activity and durability with those by the conventional impregnation method in hydrogen production reactions. They emphasized that the spc method is a highly promising route for preparing supported catalysts in the oncoming millennium. Furthermore, in the field of electrocatalysis, Barnett's group applied the ex-solution process to solid oxide fuel cells (SOFCs, the most actively grafted application), referring to this advance as the "nucleation of nanometer-scale electrocatalyst particles", in 2007.[22] They found that the maximum power density increased continuously from 250 to 390 mW cm^{-2} during the initial 100 h of SOFC operation using a typical cell employing a $La_{0.8}Sr_{0.2}Cr_{0.82}Ru_{0.18}O_{3-\delta}$ anode at 800 °C (Figure 2f). The authors suggested that the performance improvement was achieved *via* a decrease in the polarization resistance of the anode due to Ru nanoclusters, which form during the cell operation (Figure 2g,h). As such, although various terms have been used to refer to the ex-solution process, all phenomena reported this far describe spontaneous metal particle precipitation *via* results of the selective phase decomposition of an oxide solid solution according to the temperature and oxygen chemical potential.

It is important to note that the number of related works focusing on the ex-solution process has increased steeply. This means that the ex-solution technique has a pivotal role for fabricating supported catalysts. Indeed, this technology has found advanced and exciting applications in heterogeneous catalysis. However, so far, it has been mainly applied to the electrodes of high-temperature electrochemical devices due to their exclusive process conditions. For example, many researchers have utilized the ex-solution process to develop highly active and robust anodes for fuel cells operating at high temperatures and in reductive atmospheres (H_2 or C_nH_{2n+2}), representing a favorable condition for the ex-solution

https://dx.doi.org/10.1021/acsnano.0c07105
ACS Nano 2021, 15, 81−110

Table 1. Gibbs Free Energy Change of Reduction of Metal Oxides to Metal at Different Temperatures (kJ/mol)[a] (Reproduced with permission from Reference 44. Copyright 2016 Elsevier)

oxides	CaO	SrO	BaO	La_2O_3	Sc_2O_3	Fe_2O_3	Co_3O_4	NiO
300 °C	359.14	318.62	279.69	491.09	545.49	10.54	−57.67	−29.16
600 °C	343.91	305.06	268.36	472.73	525.43	−4.09	−74.96	−40.00
900 °C	328.64	291.47	256.27	456.31	507.25	−16.54	−90.78	−49.54

[a]The reaction is eq 1.

process.[23−26] Furthermore, the electrode combined with the ex-solution process has been employed in high-temperature electrolyzing systems such as those associated with CO_2,[27−29] steam,[5,30,31] electrolysis, and electrochemical gas reforming.[32] More specifically, effective promotion of electrochemical oxidation of H_2 through metal alloy nanoparticles was reported by Zhu *et al.*,[26] while greatly enhanced steam electrolysis was showcased by Tsekoras *et al.*[19] In addition to such applications, very recently, the ex-solution process has not only become actively employed as oxygen permeation membranes[33,34] and chemical looping materials[35−37] but has also been used in low-temperature reactions such as those in the CO oxidation.[38−40] Moreover, ex-solved catalysts even expand their application to aqueous solution electrolysis reactions such as nanoscale Ni ex-solution from $CaTiO_3$,[41] to toxic gas sensing materials using Ir nanoparticles socketed on WO_3, and to photocatalytic conversion processes.[42,43]

ENERGETICS AND DYNAMICS OF THE EX-SOLUTION PROCESS

When attempting to improve the performance capabilities or the utilization of supported catalysts for desired reactions in chemical and electrochemical fields, it is essential to control not only the composition, morphology, size, and number density of metal nanoparticles but also combinations of metal/oxides with functional interfaces. Because these characteristics are determined by the results of the phase instability and corresponding phase transition of the oxide solid solution, a deeper understanding of the origin and working principles of the ex-solution phenomenon is necessary to fabricate customized ex-solution catalysts. In this regard, thus far, numerous studies have been carried out, though the detailed mechanism of the ex-solution process has still remained unclear. In this section, thus, we will summarize the theoretical and empirical investigations to interpret the energetics and dynamics of the ex-solution processes reported to date.

WHY DOES IT HAPPEN?

Ex-solution refers essentially to a precipitation phenomenon of cations that are dissolved in a host oxide lattice through a reduction process of an oxide solid solution. The ex-solution generally involves four physical processes, namely, diffusion, reduction, nucleation, and growth. For the ex-solution to take place, the metal oxides (or metal ions) need to be reduced to their metallic state. Such a reaction can be written as

$$\frac{1}{x}M_xO_y + \frac{y}{x}H_2(g) = M + \frac{y}{x}H_2O(g) \quad (1)$$

Thermodynamically, the reaction in eq 1 is favorable only if the Gibbs free energy change of the reaction, $\Delta G = \sum G_{products} - \sum G_{reactants}$ is negative. In most cases, the ex-solution takes place in a reducing atmosphere (*e.g.*, H_2) to have conditions favorable for the reduction reaction. Alternatively, the eq 1 can be written in Kröger−Vink notation as follows:

$$M_M^{\times} + \frac{m}{2}O_O^{\times} = M_{ex\text{-}solution} + V_M^{m\prime} + \frac{m}{2}V_O^{\bullet\bullet} + \frac{m}{4}O_2(g) \quad (2)$$

Here, $M_M^{\times}$ and $O_O^{\times}$ are respectively the metal M and oxygen ion in oxide lattice, $M_{ex\text{-}solution}$ denotes the ex-solved metallic phase, $V_M^{m\prime}$ and $V_O^{\bullet\bullet}$ are correspondingly the cation and anion vacancies, $O_2(g)$ is oxygen gas, and m is the oxidation state of M. From a defect chemistry point of view, as shown in eq 2, when an oxide solid solution is exposed to a reductive atmosphere, the oxygen ions in the lattice are released in the form of oxygen gas, leaving positively charged oxygen vacancies and reducing metal cations to neutral species. In an oxidative atmosphere, the reduced metallic phase is dissolved again into the host oxide as a cation, if kinetics permit, and thus exhibits reversibility in redox reaction cycles. Table 1 lists the ΔG for a variety of metal oxides,[44] where we note that all alkaline earth metals (*e.g.*, Ca, Sr, Ba, and La) have $\Delta G > 0$, while most 3d transition metals, such as Fe, Co, and Ni, have $\Delta G < 0$ at temperatures higher than 600 °C (Figure 3). Therefore, the ex-solution is generally observed for the easily reducible transition metals. At higher temperatures, Fe may be also ex-solved from the host perovskite.[14,45] Although not included in Table 1, precious metals that are easily reduced are also important components of the ex-solution process.

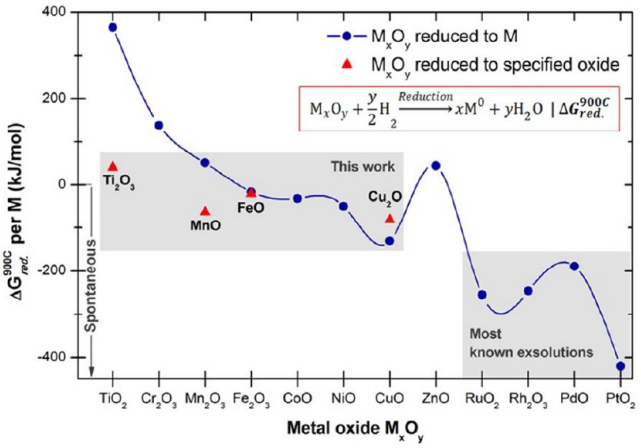

Figure 3. Gibbs free energy change of reducing transition metal oxides under reducing atmosphere at 900 °C. Inset: The reaction. Reprinted with permission from ref 14. Copyright 2013 Springer Nature.

However, the reduction properties of the metal element are not the only factor affecting the nature of ex-solution. For a stoichiometric perovskite structure, ABO_3, as a reference, the ex-solution of the B-site (reducible elements) metal may destabilize the bulk lattice structure due to the excessive loss of B-site cations (or excessive A-site cations in host lattice).[46] As such, Neagu *et al.*,[11,14,47] proposed using the A-site-deficient perovskites, $A_{1-\alpha}BO_3$, which may prevent the collapse of the

https://dx.doi.org/10.1021/acsnano.0c07105
ACS Nano 2021, 15, 81−110

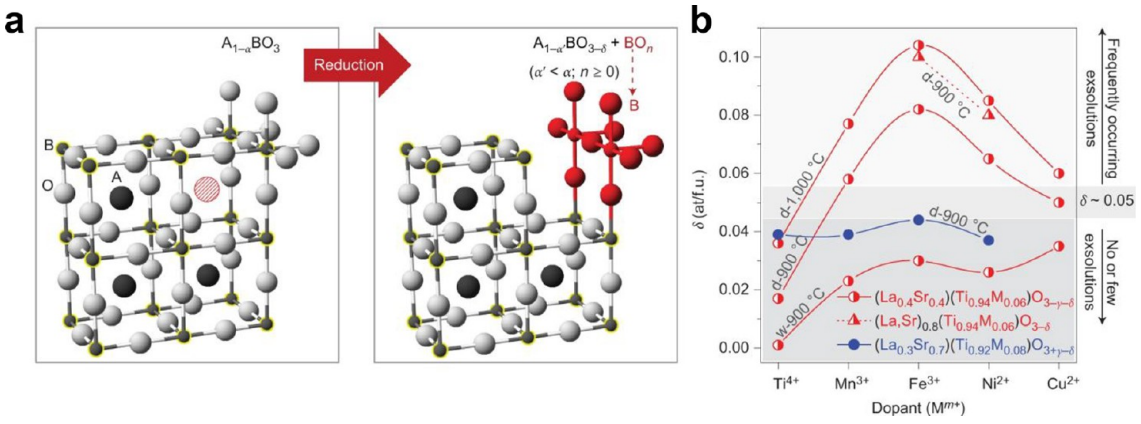

Figure 4. (a) Schematic of the B-site ex-solution process from A-site-deficient perovskite oxides under a reducing−annealing condition. (b) Extent of reduction according to various perovskite systems, dopant types (*e.g.*, Ti, Mn, Fe, Ni, and Cu) and annealing conditions. Letters d and w represent dry and wet atmospheres, respectively. Panels a and b reprinted with permission from ref 14. Copyright 2013 Springer Nature.

bulk crystal during the ex-solution, leading to more dynamic ex-solution. In addition to the A-site deficiency, the oxygen vacancies are also important in facilitating the ex-solution process.[14,48] In fact, it was described that both A-site vacancies and oxygen vacancies (or an extension of the reduction, δ) generated by reducing an A-site-deficient perovskite destabilize the overall perovskite lattice and promote excess B-site ex-solution, causing a reversion to the stoichiometric perovskite structure. This reaction can be expressed as

$$A_{1-\alpha}BO_{3-\delta} \xrightarrow{\text{ex-solution}} (1-\alpha)ABO_{3-\delta'} + \alpha B \quad (3)$$

where the left- and right-hand-side terms denote the A-site-deficient and the stoichiometric perovskites, respectively. A-site-deficient may be also understood as B-site-rich, thus increasing the predisposition of ex-solving B-site elements to re-establish the stoichiometric one. Figure 4 schematically illustrates the above-proposed ex-solution mechanism in the A-site-deficient perovskite, $A_{1-\alpha}BO_{3-\delta}$. The authors also demonstrated their principle by observing whether or not ex-solution occurs using various perovskite systems (*e.g.*, $La_{0.4}Sr_{0.4}Ti_{0.94}M_{0.06}O_{3-\gamma-\delta}$, $La_{0.46}Sr_{0.34}Fe_{0.06}Ti_{0.94}O_{3-\delta}$, $La_{0.52}Sr_{0.28}Ni_{0.06}Ti_{0.94}O_{3-\delta}$ and $La_{0.3}Sr_{0.7}Ti_{0.92}M_{0.08}O_{3+\gamma-\delta}$, M = Ti, Mn, Fe, Ni, and Cu, and γ denotes the oxygen nonstoichiometry compensated by dopants, M) and annealing conditions.

ATOMISTIC VIEW OF EX-SOLUTION

As discussed above, the thermodynamic origin of ex-solution from a macroscopic point of view is seemingly dictated by the different reducibilities of metal cations, which are also critically interdependent with the phase stability of host oxide. While the aforementioned characters on individual elements give us some general idea of why ex-solution happens, the simple metal oxides (M_xO_y) reduction model may not straightforwardly explain the ex-solution phenomena proceeding on the complex oxides posing various crystal structures and constituents. Moreover, the ex-solution process, which consists of several interrelated steps, makes the realization of mechanistic understanding elusive. Hence, comprehension of ex-solution phenomena in an atomistic scale is essential to have insights pivotal for designing material systems and approaches. In this section, we summarize the previous research which discuss ex-solution in the atomistic level.

Density functional theory (DFT)-based calculations have been employed to understand the physical mechanisms underpinning the ex-solution of nanoparticles from the host perovskite. Kizaki *et al.* did one pioneering work in this area.[49] This report suggested that the formation of nanocatalyst particles was triggered by the spinodal nanodecomposition (SND) of the host perovskite (*e.g.*, $LaFe_{1-x}Pd_xO_3$) into two different phases of $LaFeO_3$ and $LaPdO_3$. Such a phase decomposition was evaluated by the mixing energy ΔE defined as

$$\Delta E(x) = E(LaFe_{1-x}Pd_xO_3) - (1-x)E(LaFeO_3) - xE(LaPdO_3) \quad (4)$$

where $E(M)$ is the total energy of perovskite M (M = $LaFe_{1-x}Pd_xO_3$, $LaFeO_3$, or $LaPdO_3$). For $\Delta E > 0$, the system decomposes spinodally. Instead, for $\Delta E < 0$, the catalytically active nanoparticles of Pd dissolve homogeneously in the host material $LaFe_{1-x}Pd_xO_3$. The authors showed that $LaFe_{1-x}Pd_xO_3$ has a more positive ΔE than $LaFe_{1-x}Rh_xO_3$, implying that the spinodal decomposition is more pronounced for $LaFe_{1-x}Pd_xO_3$ compared to $LaFe_{1-x}Rh_xO_3$.[49] The calculation results were also consistent with the experimental observations that the $LaFe_{1-x}Rh_xO_3$ favors a homogeneous mixing with Rh atoms dispersed in the host matrix. In contrast, the self-regeneration of Pd was readily detected in $LaFe_{0.95}Pd_{0.05}O_3$.

Despite the consistency of the SND model with experiments, the model has two major shortcomings: (i) it is assumed that the catalytically active nanoparticles are in the form of a perovskite phase, $LaPdO_3$, which may be not accurate as it is generally believed that the ex-solved nanoparticles are in metallic phase;[11,14] (ii) the model did not include the influence of the surrounding atmosphere, in particular, the effect of oxygen partial pressure, p_{O_2}, and the temperature, T. In a later work, Yanagisawa *et al.*[50] proposed a thermodynamic model based on the bulk properties of the perovskite in its reduced and oxidized states. Two different reaction pathways for the reduction of B-site element into its metal phase were considered

$$A_4B_3MO_{12} \leftrightarrow \frac{3}{4}A_4B_4O_{12} + \frac{1}{2}A_2O_3 + \frac{3}{4}O_2 + M \quad (5)$$

https://dx.doi.org/10.1021/acsnano.0c07105
ACS Nano 2021, 15, 81−110

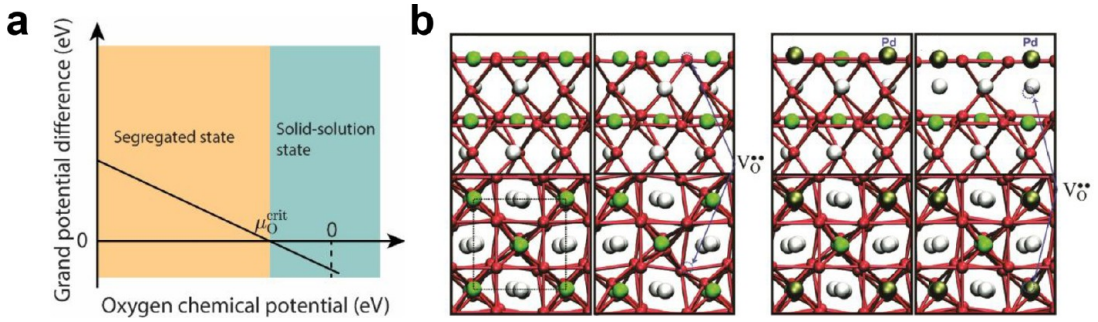

Figure 5. (a) Illustration of the segregation of precious metal in the B-site as a function of oxygen chemical potential. Adapted with permission from ref 50. Copyright 2012 American Chemical Society. (b) Side views (upper) and top views (lower) of clean $LaFeO_3$, $LaFeO_{3-y}$, $LaFe_{1-x}Pd_xO_3$, and $LaFe_{1-x}Pd_xO_{3-y}$ (001) surfaces, respectively. White, green, tan, and red balls indicate La, Fe, Pd, and O atoms, respectively. The surface unit cell used is indicated by the dotted square in the lower panel. Positions of O vacancies ($V_O^{\bullet\bullet}$) are indicated by blue dotted circles. Reprinted with permission from ref 48. Copyright 2011 American Chemical Society.

for A = A^{3+} and B = B^{3+}, or

$$A_4B_3MO_{12} \leftrightarrow \frac{3}{4}A_4B_4O_{12} + AO + O_2 + M \tag{6}$$

for A = A^{2+} and B = B^{4+}. The left- and right-hand-side terms of the above equations denote oxidized and reduced states, respectively. To address the conditions needed for the above reactions, the authors defined the grand potential difference, $\Delta\Omega$, as

$$\Delta\Omega = \Omega_{oxidized}(T, \{\mu_i\}) - \Omega_{reduced}(T, \{\mu_i\}) \tag{7}$$

where $\Omega(T,\{N_i\})$ is the grand potential for the perovskite either in the oxidized state or in the reduced state, T is the temperature, and μ_i is the chemical potential of species i. Specifically, the grand potential was calculated as

$$\Omega(T, \{\mu_i\}) = F(T, \{N_i\}) - \sum_i N_i\mu_i(T, p_i) \tag{8}$$

where $F(T,\{N_i\})$ is the Helmholtz free energy and N_i and p_i are the number of atoms of type i and partial pressure of species i. According to the definition of $\Delta\Omega$, a positive $\Delta\Omega$ means a smaller grand potential of the reduced state, predicting that the B-site element M is thermodynamically favored in its metal phase.[50] Instead, a negative $\Delta\Omega$ predicts that the M prefers the oxidized state as a solid solution in the perovskite $A_4B_3MO_{12}$. Yanagisawa *et al.* further considered the $\Delta\Omega$ as a function of μ_O, the chemical potential of oxygen, which was calculated with the following expression:

$$\mu_O(T, p_{O_2}) = \mu_O(T, p^0) + \frac{1}{2}k_BT\ln\left(\frac{p_{O_2}}{p^0}\right) \tag{9}$$

where p^0 = 1 atm, k_B is the Boltzmann constant, and $\mu_O(T,p^0)$ is the reference state of μ_O. This allows one to explore the conditions (*i.e.*, temperature and oxygen partial pressure) that are favorable for the ex-solution. The critical oxygen chemical potential, μ_O^{crit}, was defined as the μ_O that gives zero $\Delta\Omega$ (Figure 5a). When $\mu_O = \mu_O^{crit}$, the segregated state and solid-solution state of the B-site element are equilibrated. One should note that for μ_O that is smaller than μ_O^{crit}, the segregation state will be more stable; see the yellow region of Figure 5a. A more reducing atmosphere leads to a more negative μ_O, consistently with the experimental observations that lower p_{O_2} enhances ex-solution. On the basis of this model, Yanagisawa *et al.* investigated the segregation state of Pd in $LaFeO_3$ and $CaFeO_3$ perovskites. It was calculated that the μ_O^{crit} for Pd in $LaFeO_3$ is −0.93 eV, corresponding to $p_{O_2} = 10^{-3}$ to 10^2 atm at 700−1000 K, while the μ_O^{crit} for Pd in $CaFeO_3$ is −0.09 eV, corresponding to p_{O_2} around 10^{10} atm at 700−1000 K. These results explain why self-regeneration of Pd was observed only in the $LaFeO_3$-based perovskite,[6] as the required μ_O^{crit} for Pd redissolution in $LaFeO_3$ can be easily fulfilled under ambient atmosphere (p_{O_2} = 0.21 atm).

Despite the above models successfully explaining the self-regeneration of Pd nanoparticles in the $LaFeO_3$ (LFO)-based perovskites, as experimentally observed in $LaFe_{0.57}Co_{0.38}Pd_{0.05}O_3$[6] and $LaFe_{0.95}Pd_{0.05}O_3$,[51] they did not answer the question of why Pd atoms embedded deeply in the host perovskite during the redox cycle. Furthermore, these models did not consider any effects of surfaces, which typically are also important in studying the mechanism of catalysis and segregation as surfaces may behave differently from the bulk. Therefore, Hamada *et al.*[48] investigated the segregation of precious metal elements M (M = Pd, Rh, or Pt) in the LFO perovskite using slabs, as shown in Figure 5b.[48] The segregation energy, E_{seg}, of metal M is characterized by the energy difference of slabs with M atom at the surface site (E_{surf}) and in the bulk (E_{bulk}) of LFO, defined as

$$E_{seg} = E_{surf} - E_{bulk} \tag{10}$$

According to the definition, $E_{seg} < 0$ indicates that the M atom is energetically favored at the surface. The segregation energies for Pd, Pt, and Rh were computed to be −0.06, 0.23, and 0.34 eV, respectively, implying that the segregation of Pd nanoparticles is thermodynamically more favorable compared to Pt and Rh. Introducing one oxygen vacancy can drastically stabilize the structures with Pd and Pt segregated at the surface by lowering the E_{seg} to −0.88 and −1.06 eV. Hamada *et al.* further correlated the segregation energy with relevant working conditions by replacing E_{surf} and E_{bulk} in (eq 10)[48] using the grand potential Ω_{surf} and Ω_{bulk}, which are functions of μ_O as

$$\Omega_{surf/bulk} = F_{surf/bulk}(T, N_{V_O^{\bullet\bullet}}) + N_{V_O^{\bullet\bullet}}\mu_O(T, p_{O_2}) \tag{11}$$

where $F_{surf/bulk}(T,N_{V_O^{\bullet\bullet}})$ is the Helmholtz free energy of the slab with M atoms in the surface or in the bulk, $N_{V_O^{\bullet\bullet}}$ is the number of oxygen vacant sites in the system, and μ_O can be calculated using eq 9. The calculation results predicted that surface Pd is thermodynamically favored over a wide range of p_{O_2}. Instead,

https://dx.doi.org/10.1021/acsnano.0c07105
ACS Nano 2021, 15, 81−110

surface-segregated Pt is only stable below 10^{-4} atm at 1000 K (or 10^{-11} atm at 700 K). It was also predicted that the E_{seg} of Rh is positive over the entire region of p_{O_2} considered (10^{-9} to 10^{16} atm at 1000 K or 10^{-18} to 10^{17} atm at 700 K), suggesting that it is difficult to ex-solve Rh. The simulations are in agreement with experiments by Tanaka *et al.*,[52] who reported that the segregation of precious metals in LFO to form nanoparticles is facilitated in the order of Pd > Pt > Rh.

The critical role of the oxygen vacancy in stabilizing the structure with Pd at the surface was investigated by analyzing the density of states (DOS). As shown in Figure 5b, for the $LaFeO_3$ slab, the $V_O^{\bullet\bullet}$ site at the topmost surface is predicted to be the most stable position. However, for the slab with Pd at the surface, the most stable $V_O^{\bullet\bullet}$ is located in the subsurface site just beneath the surface Pd. DOS analysis indicated that the absence of subsurface O leads to the formation of the nonbonding Pd $d_{3z^2-r^2}$, which should form the weakly hybridized states with the p-state of O underneath. The formation of the nonbonding Pd $d_{3z^2-r^2}$ state effectively increases the band energy, stabilizing the structure with Pd segregated at the surface. This was also in agreement with the oxygen vacancy formation energy that the subsurface $V_O^{\bullet\bullet}$ has much lower formation energy (1.52 eV) compared to the one in the $LaFeO_3$ slab (2.13 eV). Hamada *et al.* further explored the slab models with more than one Pd atom.[48] It was predicted that when there are no oxygen vacancies or only one vacant site, the additional Pd atoms are likely found in the sublayer instead of at the surface. However, when more oxygen vacant sites are present, the slab with multiple Pd atoms at the surface stabilizes, thus forming a layer of PdO_2 at the surface. This was also confirmed in the FeO_2-terminated surfaces of $LaFe_{1-x}Pd_xO_3$ by the same research group.[53] As such, the authors then speculated that a layer of $LaPdO_{3-\delta}$ in the vicinity of the $LaFeO_3$ surface would be formed during the sample preparation because considerable amounts of $V_O^{\bullet\bullet}$ were introduced. The $LaPdO_{3-\delta}$ layer can, in turn, facilitate the self-regeneration of the active Pd particles in redox cycles.

Another important experimental observation is that nanoparticles may prefer to ex-solve on specific facets (*e.g.*, (110) surface as for bulk powder sample).[11] Gao *et al.*[44,54] systematically investigated the effects of surface orientation and the defect chemistry on ex-solving Ni nanoparticles from the host perovskites with slab models. The authors first evaluated the E_{seg} of Ni in $SrTiO_3$ perovskite and observed that the (100) surface gives the smallest E_{seg} (−1.25 eV), which may be attributed to the significant surface charge redistribution. The calculations predicted that Ni segregation is particularly favored in the (100)-oriented and SrTiO-terminated surfaces of $SrTiO_3$. It is noteworthy that this orientation was also consistent with the experiments by previous observation because the (100) surface of $SrTiO_3$ in this work is identical to the (110) orientation of the primitive cell of $La_{0.52}Sr_{0.28}Ti_{0.94}Ni_{0.06}O_{3-\delta}$.[11] Gao *et al.* further evaluated the influence of defect chemistry on E_{seg} and concluded that A-site deficiency and O vacancies promote the segregation of Ni, whereas the substitution of Sr with La hinders it. The weakened tendency for Ni to be on the surface may be due to the Coulombic attraction between the bulk $La_{Sr}^{\bullet}$ and Ni_{Ti}'', thus preventing the Ni segregation at the surface. Here the $La_{Sr}^{\bullet}$ and Ni_{Ti}'' are denoted with Kröger−Vink notation.[55] The detrimental effects of $La_{Sr}^{\bullet}$ were further confirmed by experiments with $La_{0.08}Sr_{0.72}Ti_{0.9}Ni_{0.1}O_{3-\delta}$ and $Sr_{0.8}Ti_{0.9}Ni_{0.1}O_{3-\delta}$.[54] It was observed that the energetics of Ni segregation might be closely correlated with the surface metal/oxygen atomic ratio.[54] Specifically, the (100) SrTiO-terminated slab of $SrTiO_3$, which has a higher ratio of metal to oxygen, shows an enhanced Ni segregation compared to that of the (100) O_2-terminated slab. This was attributed to the surface charge redistribution. Indeed, in the (100) SrTiO-terminated slab, Ni shows a much lower effective Bader charge than Ti (1.15 *vs* 1.81 at the surface and 1.30 *vs* 2.29 in the bulk). As such, ex-solving Ni toward the surface can effectively compensate for the positive charge of the slab if all atoms remain at their nominal valence state as in bulk. This, in turn, lowers the total energy and thus stabilizes the structure. Such a charge redistribution also explained the effect of A-site deficiency on Ni ex-solution. The A-site deficiency in $SrTiO_3$ can be also regarded as Sr vacancy, V_{Sr}'', which formally has a −2 charge. It was predicted that the most stable position of the Sr vacant site is at the top surface, which can effectively compensate for the charge of (100) SrTiO-terminated slab, thus favoring the Ni segregation. Hence, the E_{seg} with the V_{Sr}'' at the surface was calculated to be −1.78 eV, 0.53 eV smaller than the one without V_{Sr}''. The beneficial effect of A-site deficiency was also verified by the experimental observations on $Sr_{0.8}Ti_{0.9}Ni_{0.1}O_{3-\delta}$. The oxygen vacancies $V_O^{\bullet\bullet}$ were also studied, and it was found that the most stable O vacant site is the one closest to Ni_{Ti}'', probably due to the Coulombic attraction between the positively charged $V_O^{\bullet\bullet}$ and negatively charged Ni_{Ti}''. Using a similar approach as the one followed by Hamada *et al.*[48] Yanagisawa *et al.*[50] and Gao *et al.*[54] predicted that the segregation energy decreases (−3 eV) with the μ_O. Therefore, under reducing conditions, more O vacancies would be introduced, and the ex-solution of Ni toward the surface would also be facilitated.

In addition to the simple perovskite of ABO_3, ex-solution was also observed in the double perovskite $AA'BB'O_{6-\delta}$.[56−59] However, the mechanism behind the ex-solution process in the layered perovskite has rarely been explored. Sun *et al.* experimentally observed the Co ex-solution process in real time with the $Pr_{0.5}Ba_{0.5}Mn_{0.9}Co_{0.1}O_3$ perovskite by *in situ* transmission electron microscopy (TEM).[59] By combining a thermogravimetric analysis (TGA), TEM observations, and DFT calculations, they also suggested that the crystal reconstruction of Co-doped double perovskite $Pr_{0.5}Ba_{0.5}Mn_{0.9}Co_{0.1}O_{3-\delta}$ in the cubic phase to form a layered oxygen-deficient structure of $PrBaMn_{1.8}Co_{0.2}O_{5-\delta}$ in the orthorhombic phase, may facilitate the segregation process. Under reducing atmosphere, a large number of oxygen vacancies were introduced in the PrO_x plane together with the reduction of Co^{3+} to Co^{2+} or Co^0, thus forming the metallic Co nanoparticles. They later carried out the DFT calculations for the Co vacancy formation energy in both structures and found that the layered perovskite $PrBaMn_{1.8}Co_{0.2}O_{5-\delta}$ favors the formation of Co vacancy with a lower energy cost (3.62 eV) compared to the pristine $Pr_{0.5}Ba_{0.5}Mn_{0.9}Co_{0.1}O_{3-\delta}$ (4.82 eV). The lower vacancy formation energy may be attributed to the decreased number of O surrounding Co in the oxygen-deficient layered structure $PrBaMn_{1.8}Co_{0.2}O_{5-\delta}$, thus weakening the bonding energy that stabilizes Co and facilitating the Co ex-solution.[59]

Similarly, Kwon *et al.*[58] observed the ex-solution of nanoparticles in the layered perovskite $PrBaMn_{1.7}M_{0.3}O_{5+\delta}$ (M = Mn, Co, Ni, and Fe), and they further explored the ex-solution mechanisms in this type of perovskite as well as the

https://dx.doi.org/10.1021/acsnano.0c07105
ACS Nano 2021, 15, 81−110

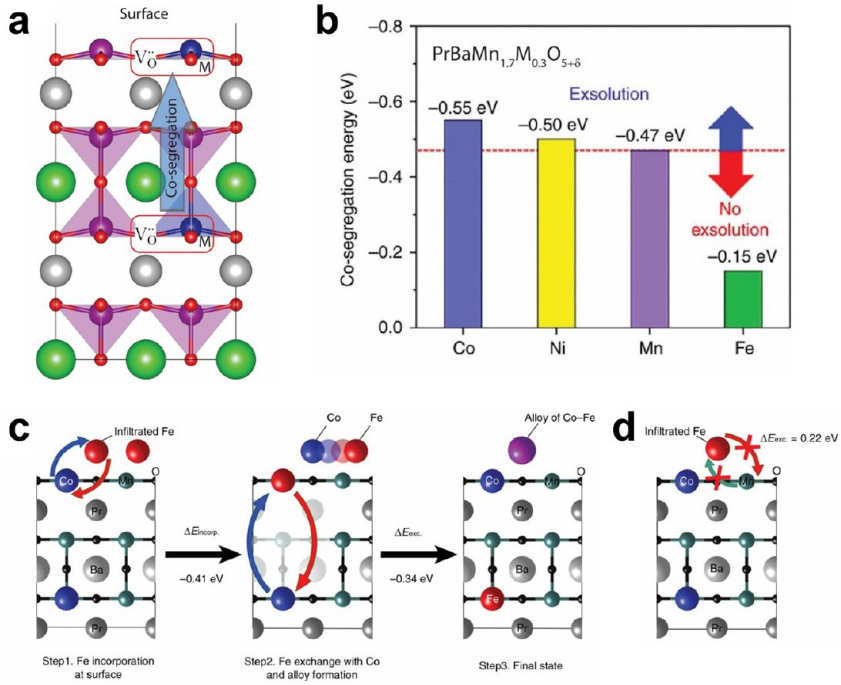

Figure 6. (a) Schematic illustration of the model used for the calculations of co-segregation energy. Pr, Ba, Mn, M (Mn, Co, Ni, and Fe), and O atoms are shown as gray, green, dark blue, purple, and red, respectively. The inset red boxes indicate the co-segregation of B-cation with an oxygen vacancy. (b) Comparison of the co-segregation energy with the dopant (M) materials. Reproduced with permission from ref 58. Copyright 2017 The Authors under a Creative Commons CC-BY 4.0 (https://creativecommons.org/licenses/by/4.0/), published by Springer Nature. (c) Topotactic ion-exchange energetics for the mechanism of particle ex-solution *via* Fe infiltration on the surface. (d) Unfavorable incorporation energy of infiltrated Fe with Mn of the top surface. Reproduced with permission from ref 57. Copyright 2019 The Authors under a Creative Commons CC-BY 4.0 license (https://creativecommons.org/licenses/by/4.0/), published by Springer Nature.

ex-solution trends of these transition metals. The authors hypothesized that the ex-solution in this type of material was triggered by the simultaneous introduction of oxygen vacancies and B-site metal vacancies (named co-segregation). The ex-solution reaction can be expressed as

$$M_{Mn}^{\times} + O_O^{\times} = MO + V_O^{\bullet\bullet} + V_{Mn}^{''} \quad (12)$$

$$MO = M_{(\text{metallic ex-solution})} + \frac{1}{2}O_2 \quad (13)$$

The ex-solution was characterized by the co-segregation of B-site transition metal element M together with the nearby oxygen vacancy,[58] as shown in Figure 6a. The co-segregation energies for Co, Ni, Mn, and Fe in the $PrBaMn_{1.7}M_{0.3}O_{5+\delta}$ are −0.47, −0.55, −0.50, and −0.15 eV (Figure 6b), suggesting that the ex-solution of Co or Ni is more favorable compared to that of Mn or Fe. After the co-segregation of the B-site element M and O vacancy at the surface, the oxide MO would be further reduced into its metallic phase following (eq 13). To facilitate this reaction, the O vacancy formation near the segregated M-site at the surface should be favorable.[58] The authors further calculated the formation energy of oxygen vacancies at different sites and confirmed that the vacant site near the surface M is the most stable position. The energy required to form the O vacancy at the surface decreases as follows Mn > Fe > Ni > Co, suggesting that the conversions of the segregated NiO and CoO into their metals may be easier compared to the FeO and MnO in the $PrBaMn_{1.7}M_{0.3}O_{5+\delta}$ layered perovskite. Such a preference order of ex-solution was also confirmed in experiments, where ex-solved nanoparticles were observed in $PrBaMn_{1.7}M_{0.3}O_{5+\delta}$ (M = Mn, Co, Ni) and the fuel cells with $PrBaMn_{1.7}Co_{0.3}O_{5+\delta}$ (PBMCo) and $PrBaMn_{1.7}Ni_{0.3}O_{5+\delta}$ anodes showed much higher maximum power densities (1.15 and 1.12 W/cm^2 in humidified H_2 at 800 °C, respectively) than the ones with $PrBaMn_{1.7}Fe_{0.3}O_{5+\delta}$ (PBMFe, 0.69 W/cm^2) and $PrBaMn_{1.7}Mn_{0.3}O_{5+\delta}$ (0.66 W/cm^2).[58] Since Co cation has a lower co-segregation energy (−0.55 eV) compared to Fe (−0.15 eV), the ex-solution of Co from the PBMCo is much easier than Fe from the PBMFe.[58] As such, the same group[57] further proposed the concept of topotactic ion exchange for PBMCo (*i.e.*, replacing the Co cations in PBMCo by Fe) which can be introduced by infiltration. The reaction for the topotactic ion exchange in the PBMCo can be expressed as

$$Co_{Co}^{\times} + O_O^{\times} + FeO_{(\text{infiltrated})} = CoO_{(\text{ex-solved})} + V_O^{\bullet\bullet} + Fe_{Co}^{\times} \quad (14)$$

As one can observe, the incorporated Fe cations are at the Co-sites in the bulk PBMCo, whereas the Co would be segregated toward the surface and be reduced into Co metals following (eq 14). DFT calculations predicted that the deposited Fe incorporates into the near-surface of PBMCo through the cation exchange with surface Co. This cation exchange is thermodynamically favored with an energy cost of −0.41 eV for Fe occupying the surface Co-site in the PBMCo slab, as shown in step 1 of Figure 6c. After the incorporation of the surface Co-site, the further exchange between the Fe and the bulk Co is also energetically favorable with an exchange energy of −0.34 eV; see step 2 of Figure 6c, implying that Co ex-solution can be facilitated by the incorporation of Fe. On the other hand, the incorporation of Fe with the Mn in the PBMCo is endothermic with an exchange energy of 0.22 eV

https://dx.doi.org/10.1021/acsnano.0c07105
ACS Nano 2021, 15, 81−110

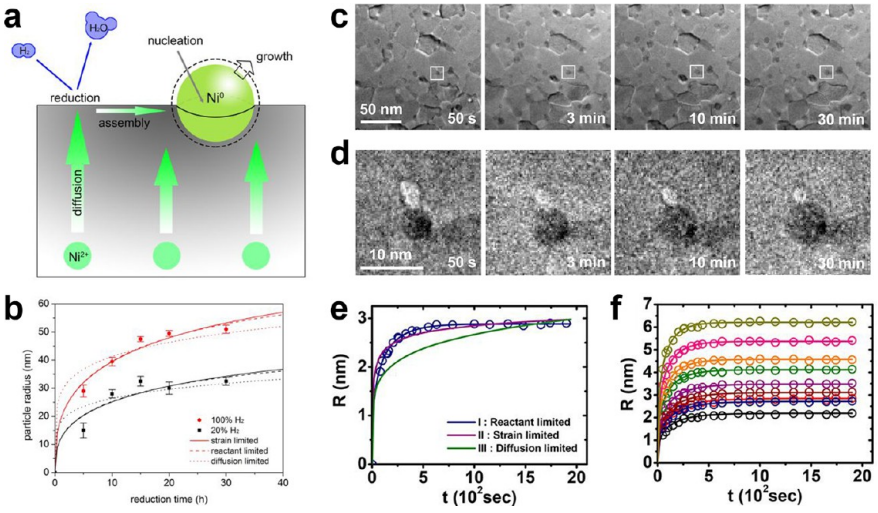

Figure 7. (a) Illustration of the ex-solution process, diffusion, reduction, nucleation, and growth. (b) Average particle size and fitting curves with the strain-limited model (solid line), reactant-limited model (dashed line), and diffusion-limit model (dotted line). Panels a and b reproduced with permission from ref 44. Copyright 2016 Elsevier. (c) Series of *in situ* transmission electron microscopy (TEM) images of ex-solved Co particles from $SrTi_{0.75}Co_{0.25}O_{3-\delta}$ thin film with time at 800 °C. (d) Magnified TEM images of the boxed regions in panel c at the corresponding times. (e, f) Radius evolution of the Co particle in panel d and selected particles according to time with the fitted curves. Panels c–f reproduced with permission from ref 39. Copyright 2019 American Chemical Society.

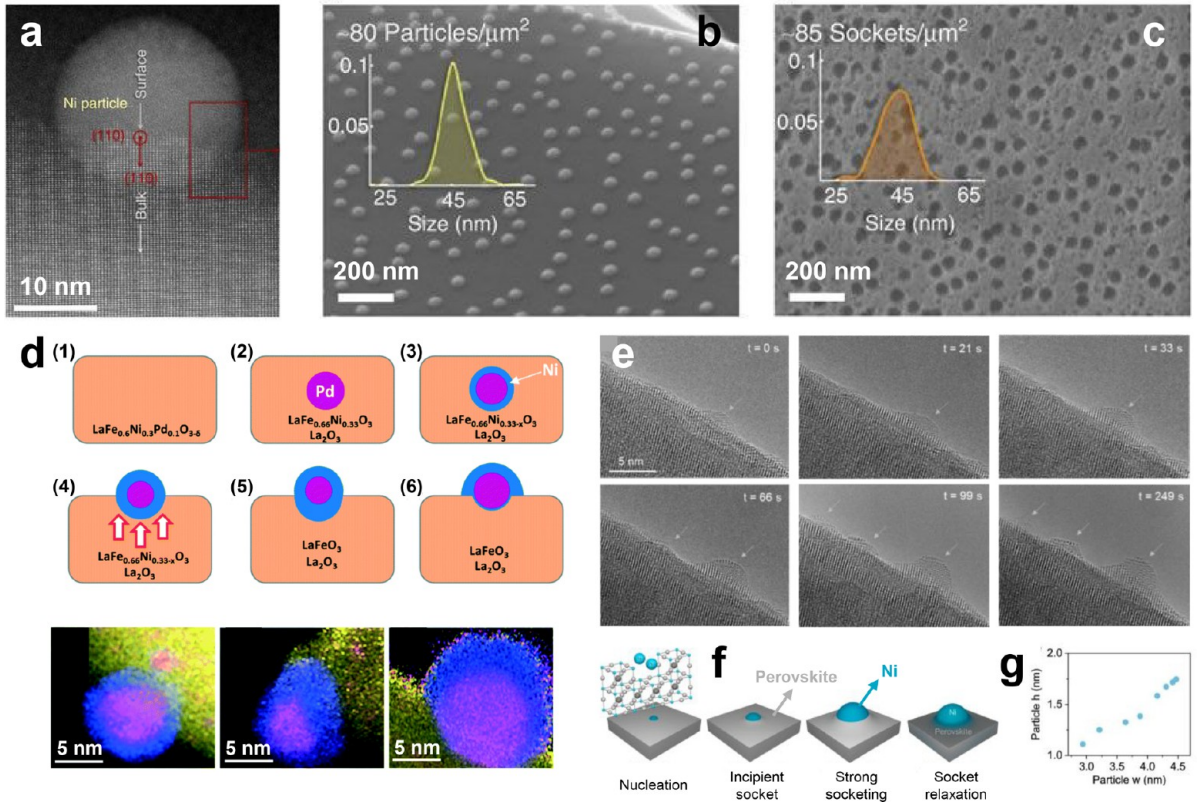

Figure 8. (a) Transmission electron microscopy (TEM) image of ex-solved Ni particles on a (110) perovskite surface. (b, c) Scanning electron microscopy (SEM) images of ex-solved Ni particles before and after etching in HNO_3. The insets show the corresponding size distributions of the particles and sockets. Panels a–c reproduced with permission from ref 11. Copyright 2015 The Authors under a Creative Commons CC-BY 4.0 license (https://creativecommons.org/licenses/by/4.0/), published by Springer Nature. (d) Schematic illustration of core–shell ex-solution from $LaFe_{0.6}Ni_{0.3}Pd_{0.1}O_{3-\delta}$. The EDX-STEM images describe the last three stages. Reproduced with permission from ref 64. Copyright 2018 The Royal Society of Chemistry. (e) *In situ* TEM observation of Ni ex-solution from $La_{0.43}Ca_{0.37}Ni_{0.06}Ti_{0.94}O_3$ perovskite at 900 °C under H_2 with different times, *t*. (f) Suggested particle growth and socket formation process during the ex-solution process. (g) Plot of the ex-solved particle height (*h*) and width (*w*). Panels e–g reproduced with permission from ref 65. Copyright 2019 American Chemical Society.

https://dx.doi.org/10.1021/acsnano.0c07105
ACS Nano 2021, 15, 81–110

(Figure 6d), suggesting that Fe would selectively replace the Co during the topotactic ion-exchange reaction (eq 14). The calculation results were also supported by the experiments that the PBMCo infiltrated with 12 wt % Fe reached the maximum power density of 1.83 W/cm^2 in humidified H_2 at 800 °C.[57]

KINETICS OF EX-SOLUTION

Although the atomistic models have been applied to understand the mechanisms underpinning the ex-solution of nanoparticles, these models can hardly shed light on the kinetics of ex-solution. A deeper understanding can be gained from continuum models. Under the framework of classical nucleation theory, ex-solution can be understood as a chemically driven heterogeneous phase transformation involving several separate physical processes: (i) diffusion of metal ions M^{n+} to the surface, (ii) reduction of M^{n+} into M^0, (iii) assembly of M^0 and nucleation, and (iv) the growth of metal nanoparticles.[44,60] Figure 7a schematically illustrates the four processes during ex-solution, taking Ni in $La_{0.4}Sr_{0.4}Sc_{0.9}Ni_{0.1}O_{3-\delta}$ as an example. In order to ex-solve the nanoparticles of Ni at the surface, the Ni^{2+} ions in the bulk first diffuse from the bulk to the surface of the perovskite and subsequently reduce to Ni^0 metal under the reducing atmosphere. After that, the Ni^0 assembles and forms small nanoparticles, which grow in size as a function of the treatment time.

A variety of intrinsic and extrinsic parameters may influence the nanoparticle nucleation and growth. Intrinsic properties include the surface characteristics such as orientations, porosity, and roughness,[61] mechanical stresses, and related strains,[12] wetting properties,[62] and the presence of defects such as A-site and oxygen vacancies and dislocations.[11,14,63] Extrinsic factors, such as the characteristics of the environment in which ex-solution occurs (*e.g.*, gas partial pressure), treatment time, and temperature, may determine the particle size growth.[44] Regarding the growth of nanoparticles size, Gao *et al.*, proposed three different models based on different mechanisms: (a) the strain-limited; (b) reactant-limited; (c) diffusion-limited.[44] For those three different analytical models, the particle size evolution follows

$$r = r_{\text{s-lim}}\left(\ln\left(1 + \frac{t}{\tau_{\text{s-lim}}}\right)\right)^{1/3} \tag{15a}$$

$$r = r_{\text{r-lim}}\left(1 - \exp\left(-\frac{t}{\tau_{\text{r-lim}}}\right)\right)^{1/3} \tag{15b}$$

$$r = r_{\text{d-lim}}\left(\frac{t}{\tau_{\text{d-lim}}}\right)^{1/6} \tag{15c}$$

where $r_{\text{s-lim}}$, $r_{\text{r-lim}}$, $r_{\text{d-lim}}$, and $\tau_{\text{s-lim}}$, $\tau_{\text{r-lim}}$, $\tau_{\text{d-lim}}$ are the characteristic radii and characteristic time scales for the strain-limited model, reactant-limited model, and diffusion-limited model, respectively. Figure 7b shows the growth of Ni nanoparticles from $La_{0.4}Sr_{0.4}Sc_{0.9}Ni_{0.1}O_{3-\delta}$ under different reducing atmospheres as a function of reduction time. One can notice that the best fitting was obtained using the strain-limited and reactant-limited models. In this regard, recently, Jo *et al.* observed the growth of the Co ex-solution process in real time using very dense, flat, and polycrystalline $SrTi_{0.75}Co_{0.25}O_{3-\delta}$ thin films and *in situ* TEM and quantitatively analyzed the size, number density, and amounts of ex-solved particles (Figure 7c–f).[39] It was confirmed that the particle growth follows the reactant-limited case with these samples and the given conditions. Furthermore, they succeeded, in extracting the growth activation energy and ex-solution enthalpy values experimentally by combining them with the defect chemical model, as expressed in eq 2.

In contrast to deposited particles, ex-solved particles have a fascinating geometry, termed the socketed structure, which is submerged at around 30% into the oxide support (Figure 8a). The particles have an epitaxial structure with regard to the oxide. This phenomenon is well-described in the literature.[11] Neagu *et al.* confirmed that the sockets (or pits) which form due to the etching of the ex-solved Ni particles on $La_{0.52}Sr_{0.28}Ni_{0.06}Ti_{0.94}O_3$ in HNO_3 have similar sizes and number densities compared to pristine ex-solution particles as shown in Figure 8b,c. However, there remains much debate as to why socket formation occurs and the details of its process, though several studies have investigated these factors. Oh *et al.*[12] carried out finite element simulations based on the strain field and also observed the surface of $La_{0.4}Sr_{0.4}Ti_{0.97}Ni_{0.03}O_{3-\delta}$ pellet through atomic force microscopy (AFM) to analyze surface morphology evolution during ex-solution process. It was suggested that the metallic phase was nucleated from the subsurface, subsequently moving to the surface. The formed metal particles deform the surrounding oxide and induce an elastic strain in the system. When the particles migrate from the matrix to the surface, the particles' surfaces are no longer constrained and the elastic energy decreases. However, the migration of particles to the surface will lead to an increase in the surface energy. As a result, there is an interplay between the surface free energy and the strain energy associated with the metal particles. In the strain-field model, the authors found that the movement of a metal particle toward the surface is accompanied by the formation of a pit on the surface. Eventually, when the nucleus grows beyond the critical size, the nanoparticle emerges from the formed pit, leading to the experimentally observed particle-in-a-pit morphology. A similar result was suggested by Buharon *et al.*[64] The authors reported through a TEM analysis in the $LaFe_{0.6}Ni_{0.3}Pd_{0.1}O_{3-\delta}$ system that Pd nuclei were formed at the subsurface in the oxide with Ni wrapped around the Pd, leading to the Pd–Ni core–shell structure and ultimately moving toward the surface of the oxide (Figure 8d). Thus far, this mechanism is widely known in related fields; however, it is also suggested that nucleation into the subsurface of the oxide and the corresponding movements are energetically unfavorable compared to nucleation at the surface. In this regard, recently, Neagu *et al.* observed and suggested different socket formation mechanisms using environmental TEM.[65] They observed that the initially formed nuclei do not move (Figure 8e,f), grow isotropically (Figure 8g) in the same location, and push the oxide supports, resulting in a volcano-shaped socket.

Alternatively, the kinetics and microstructure evolution of the B-site segregation and nucleation in perovskite structure may be well-explained under the phase-field framework. Starting from the "Poisson–Cahn" theory, which has been used to understand the segregation of defects in the surface layer of perovskites,[66–69] Jiang *et al.*[70] developed a microscale phase-field model for A-site-deficient perovskite $A_{1-x}(B_{1-x}M_x)O_{3-\delta}$ to illustrate the ex-solution processes, including the segregation of B-site element M in the surface layer, the segregation-mediated spinodal (nucleation) on the surface, and

https://dx.doi.org/10.1021/acsnano.0c07105
ACS Nano 2021, 15, 81–110

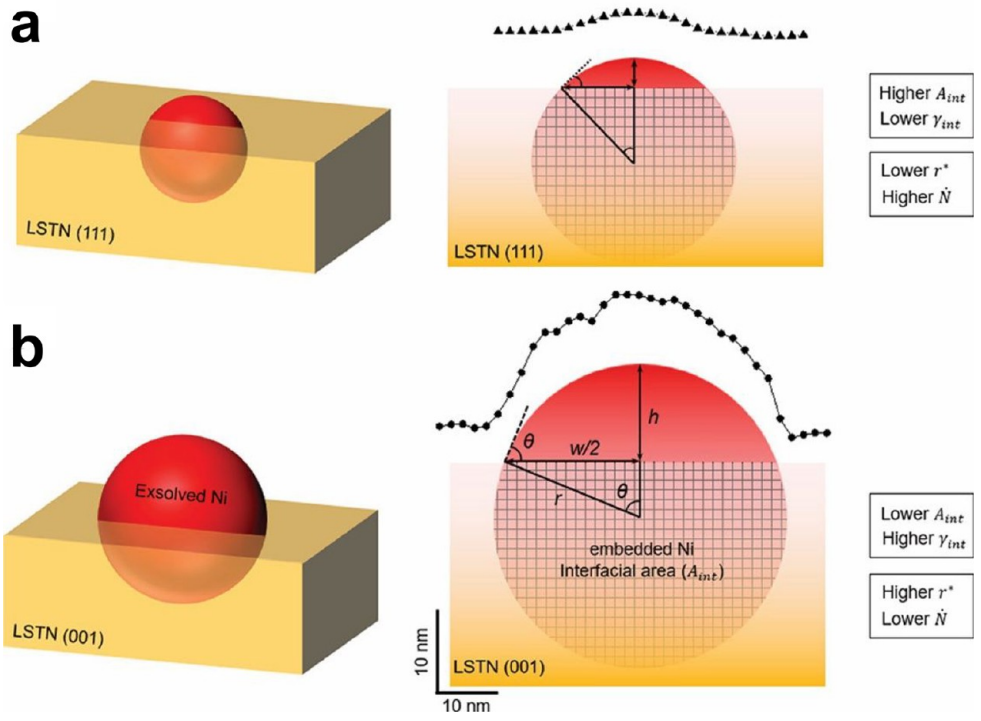

Figure 9. Illustration of ex-solved Ni nanoparticles on the thin films of $La_{0.2}Sr_{0.7}Ti_{0.9}Ni_{0.1}O_{3-\delta}$ (LSTN) with different orientations: (a) LSTN (111); (b) LSTN (001). The left panels show the 3D view, while the right panels show the cross-section view. Reproduced with permission from ref 74. Copyright 2019 American Chemical Society.

the coarsening of the B-site metal nanoparticles. In this model, the host perovskite was assumed as a solid solution with pores (denoted with P) and the surface layer was modeled as a diffuse interface. Additionally, the defect interactions and the gradient energy terms were also taken into account in the chemical potential of the species. In specific, the perovskite matrix (PM phase), $A_{1-x}(B_{1-x}M_x)O_{3-\delta}$ was modeled as a three-element solid solution of $\{x_P P + (1 - x_P)xM + (1 - x_P)(1 - x)ABO_{3-\gamma}\}$ or $\{x_P P + x_M M + x_A A\}$, where x_A, x_M, and x_A are the molar fractions of pores, B-site element M, and the stoichiometric perovskite $ABO_{3-\gamma}$ without M (denoted as A). For the PM phase, the molar fraction of A is near to 1 with $x_A = (1 - x_P)(1 - x) \approx 1$.[70] Upon reduction, the M ex-solves from the PM surface to form the nanoparticles (NPs), which are rich with M with $x_A = (1 - x_P)(1 - x) \approx 1$. Besides, the environment (EN phase) was modeled as pore rich, $x_P \approx 1$. Therefore, the PM, NP, and EN phases can be represented as the solutions of A, M, and P elements with the corresponding equilibrium compositions, respectively. The homogeneous Gibbs free energy per mole of solution can be calculated as

$$g = \sum_{i=A,M,P} (\mu_i^0 x_i + x_i RT \ln x_i) + \sum_{i=A,M,P} \sum_{j>i} x_i x_j L_{ij} \quad (16)$$

where μ_i^0 is the standard chemical potential, R is the gas constant, T is the temperature, and L_{ij} is the interaction energy between components. In this model, the authors suggested that L_{ij} is correlated to the oxygen partial pressure p_{O_2} and a lower p_{O_2} induces higher L_{ij}. In order to trigger ex-solution, the PM phase should be driven away from the equilibrium state *via* two paths. One path is to drive the PM phase to a metastable or even an unstable state. The other path is to increase the concentration of M in the PM phase such that PM is destabilized. In practice, the first path can be realized by increasing the interaction energy L_{ij} to be more positive, which can be achieved by lowering the p_{O_2}.[11,14,47] The second path can be reached by decreasing the standard chemical potential of M in the surface region $\mu^0_{M,surf}$ than that in the bulk $\mu^0_{M,bulk}$, (*i.e.*, lowering the segregation energy of M μ^{seg}_M ($\mu^{seg}_M = \mu^0_{M,surf} - \mu^0_{M,bulk}$) to be more negative).[70] On the basis of this model, Jiang *et al.* concluded that the ex-solution of the B-site dopant M results from the spinodal decomposition, as triggered by surface segregation and expansion of the chemical spinodal region. The impact of p_{O_2} was also investigated using the phase-field model. It was found that lowering the p_{O_2} can drastically promote the kinetics of nucleation and increase the number of ex-solved particles. This is also consistent with the experiments that almost all ex-solution procedures were observed under reducing atmosphere with low oxygen partial pressure.[11,14,47,71,72] They also discovered that an increase in the fraction of M in the B-site can accelerate the kinetics of nucleation and increase the coverage of stable ex-solved particles, the stable surface coverage, and the size and the surface area of the ex-solved particles.[70] The simulation results are also supported with experimental evidence that a higher number of finer Ru nanoparticles could be observed as Ru increased in concentration the $(La, Sr)(Cr, Ru)O_{3-\delta}$ perovskite.[73] As concluded by Jiang *et al.*,[70] p_{O_2} plays a critical role in influencing the nucleation and growth of nanoparticles in the ex-solution. However, the quantitative correlations between p_{O_2} and the ex-solved nanoparticles were still not addressed. Equivalently, the above phase-field model did not answer the question of why metallic Fe ex-solves on the surface of $Sr_{0.95}Ti_{0.3}Fe_{0.63}Ni_{0.07}O_{3-\delta}$ (STFN) anode, whereas Fe prefers to be in the bulk of $SrTi_{0.3}Fe_{0.7}O_{3-\delta}$ (STF) anode under the same

https://dx.doi.org/10.1021/acsnano.0c07105
ACS Nano 2021, 15, 81−110

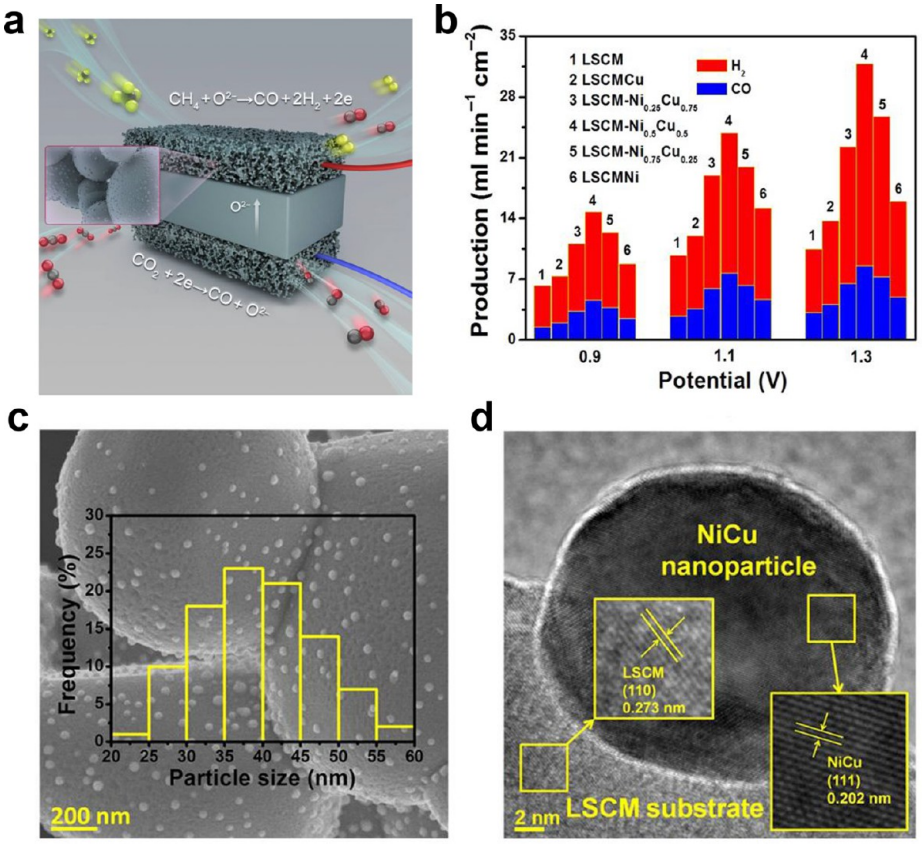

Figure 10. (a) Schematic of the electrochemical CO_2/CH_4 reforming process in a solid oxide electrolyzer to produce syngas. CO_2 electrolysis is performed on the cathode, whereas the electrochemical oxidation of CH_4 is performed on the anode. (b) CO production and H_2 production at the anode with various anode materials. (c) SEM images of the reduced LSCM-$Ni_{0.5}Cu_{0.5}$. (d) Transmission electron microscopy microscopic results of the reduced LSCM-$Ni_{0.5}Cu_{0.5}$. Reproduced with permission from ref 80. Copyright 2018 The Authors under a Creative Commons CC-BY 4.0 license (https://creativecommons.org/licenses/by/4.0/), published by American Association for the Advancement of Science.

reduced conditions, as observed experimentally.[26] In principle, for a low enough p_{O_2}, both cations (Fe and Ni, in the analyzed case) undergo complete ex-solution. Instead, a high p_{O_2} is detrimental to the ex-solution and may prevent both cations to be segregated. To quantitatively determine the effects of p_{O_2} on the ex-solution and answer the question that under which condition which cation would be ex-solved, Zhu *et al.*[26] developed a regular solution model to predict the equilibrium composition of Fe−Ni alloyed nanoparticles ex-solved from STFN. The composition of Fe in the ex-solved $Ni_{1-x}Fe_x$ alloy was derived as the following expression

$$x \exp\left[\frac{\Omega(1-x)^2}{RT}\right] \approx \left(\frac{p_{O_2}^{red}}{p_{O_2}}\right)^{3/4} \quad (17)$$

where Ω is the binary alloy interaction parameter, $p_{O_2}^{red}$ is the critical oxygen partial pressure for reduction of Fe in the undoped oxide, such as STF, and p_{O_2} is the effective oxygen partial pressure during ex-solution. The model predicted that metallic Fe is present in the ex-solved nanoparticles if $p_{O_2} > p_{O_2}^{red}$. For example, under reducing condition, (*i.e.*, $p_{O_2} = 4 \times 10^{-20}$ atm (10% H_2/3% H_2O/87% Ar) at 850 °C), the model predicted the composition of ex-solved nanoparticles as $Ni_{0.7}Fe_{0.3}$, in reasonable agreement with the XRD measurement of $Ni_{0.72}Fe_{0.28}$. Additionally, the model indicates that the Fe content x decreases as p_{O_2} increases, as shown in eq 17, suggesting that the composition can be well-controlled by tuning the p_{O_2}.

Besides the factors considered so far, the orientation of the host lattice surface and the lattice strain are the other two key factors influencing the energetics of the ex-solution. Recently, two studies explored the influence of these two parameters on ex-solving Ni particles from $La_{0.2}Sr_{0.7}Ti_{0.9}Ni_{0.1}O_{3-\delta}$ (LSTN) thin films.[60,74] Kim *et al.* systematically investigated the impact of surface orientation on ex-solution by carrying out both experiments and theoretical calculations based on classical homogeneous nucleation theory.[74] Experimentally, LSTN were deposited on different substrates to obtain LSTN thin films with different orientations. The authors observed that the surface orientation is closely related to the interfacial energy γ_{int}, thus leading to varied nanoparticle size distribution as well as other properties of the ex-solved Ni. In particular, the obvious difference in the particle contact angles and the corresponding interfacial areas observed by AFM, as schematically illustrated in Figure 9. Figure 9 strongly supported the claim that the γ_{int} is altered with different orientations. Compared to the (001) orientation, the (111) orientated thin film gives a larger area-normalized interfacial area A_{int}, resulting in a relatively smaller γ_{int}. As suggested by Kim *et al.*, a smaller γ_{int} lowers the nucleation barrier and decreases the size

https://dx.doi.org/10.1021/acsnano.0c07105
ACS Nano 2021, 15, 81−110

of the nucleus.[74] Furthermore, a small γ_{int} also accelerates the nucleation, thus increasing the particle population density in the (111) oriented film. This was also confirmed by experimental observations that the ex-solved nanoparticles at the (111) oriented thin film showed the largest number, the smallest size, the deepest embedment, and the smallest and most uniform interparticle distance. In related work, Han *et al.* explored the impact of lattice strains.[60] The lattice strain in the LSTN thin films was tuned by adjusting the lattice mismatch between the LSTN crystal and the substrates. The authors noticed that misfit-strain energy plays a key role in controlling the size and the population density of ex-solved nanoparticles in the presence of lattice strains. Specifically, a compressive strain leads to a higher degree of strain relaxation, thus resulting in a reduced critical radius, r^*, of the ex-solved nanoparticles, as well as a reduced nucleation barrier. This was also verified in the experiments that a larger number of ex-solved particles were observed in the compressive-strained films compared to the tensile-strained ones.[60]

PERSPECTIVE ON FUTURE RESEARCH DIRECTIONS

In the previous section, we focused on scientific endeavors to understand the phenomenology of ex-solution. While these efforts significantly deepen our knowledge regarding the ex-solution process, the formidable potential of ex-solution technique is not fully explored as of present. Thus, in this section, we review applications of the ex-solution process which may guide the future research directions,[3,47,75] and aim to offer possible topics to be uncovered in the future.

MULTICOMPONENT EX-SOLUTION

The ex-solution of single-phase metal nanoparticles has been investigated intensively. However, great outlooks are further anticipated *via* multicomponent ex-solution such as alloy. Alloys refer to a mixture of more than one metal component. By forming an alloy, each element often brings individual characteristics to constitute advanced physical and chemical properties that a pure metal cannot possess. Hence, investigating multicomponent ex-solution techniques may demonstrate improved catalytic properties.

One can cite the example of the NiCu alloy. Ni is renowned for its high catalytic activity toward H_2 oxidation but it is also highly vulnerable to coke formation.[76,77] On the other hand, Cu has relatively dull selectivity toward H_2 evolution but remains strong in a CO_2/CO stream with excellent coking resistance.[78,79] Therefore, blending the two different metal components to lend their own benefits would be one logical means of crafting a superior catalyst. In light of that, Lu *et al.* demonstrated a highly efficient electrochemical reformer of CH_4/CO_2 through the $Ni_{1-x}Cu_x$ alloy ex-solution process by utilizing $La_{0.75}Sr_{0.25}Cr_{0.5}Mn_{0.5}O_{3-\delta}$ (LSCM) as a host oxide (Figure 10).[80] This advanced conceptual solid-oxide electrolyzer device based on the alloy ex-solution showed stable performance for 300 h of continuous elevated-temperature operation (800 °C), providing a practical route to curtail greenhouse gases while also producing high-value syngas simultaneously. The augmented catalytic activity due to the synergy of Ni and Cu is shown in Figure 10b. Indeed, the overall production rate of H_2/CO is higher compared to when Ni or Cu nanoparticles are used alone. Particularly, as the $Ni_{1-x}Cu_x$ ratios are varied, the electrochemical performance outcomes also change, and the optimal ratio as reported by these researchers was $Ni_{0.5}Cu_{0.5}$. Therefore, it seems that not only the choice of elements is important, but also the ratio of the constituents is key to maximize the catalytic efficiency, and the composition of the alloy should be chosen judiciously.

However, even with the excellent prospects of alloy as described above, the search for an ideal recipe remains challenging, as it entails a skillful balancing act. Unlike the single metal ex-solution process with low segregation energy, the energetic landscape of the alloy ex-solution process can be highly complex given that the segregation energy levels of individual elements are distinct.[58] Thus, an advanced model of energetics and growth kinetics for multicomponent nanoparticles should be developed in the future. This should consider the fact that two different metal heterogeneous nucleation reactions are available (*i.e.*, concurrently, disproportionately, and also selectively depending on the reducibility of ex-solutes and the condition of ex-solution undertaken), which also accompanies the metal cation-exchange process in the nanoparticles. The development of such a model will lead to more intuitive control of alloy nanoparticles regarding their size, compositions, structure, and morphology.

Moreover, immiscibility between the metal components is another important issue to determine whether the metal ex-solutes will form a homogeneous alloy. Indeed, Li *et al.* detail the co-ex-solution process of Pd and Fe in which the elements did not form a solid solution but were anchored individually on the oxide support of $La_{0.8}Sr_{0.2}Fe_{0.9}Nb_{0.1}Pd_{0.04}O_{3-\delta}$.[81] Similarly, Pd and Ni do not form a homogeneous alloy but rather take the shape of a core−shell structure, as reported by Buharon *et al.*[64] The scenario becomes more complicated when more than two constituents form alloy. For the $Cu_{1-x}Ni_xFe_2O_4$ spinel oxide, Kang *et al.* reported the two different phases of ex-solved alloys: independent Cu-rich and Fe-rich ternary CuFeNi alloys during a reductive heat treatment.[82] Therefore, while finding the combination of elements to form alloy nanoparticles is pivotal to achieve the required properties demanded by specific applications, the conventional heuristic design may be a time- and resource-consuming task. So far, the experimentally confirmed ex-solved binary alloys are NiCu,[80,83] CuFe,[84] CoFe,[45,57,85−89] CoNi,[10,56,90,91] NiFe,[13,23,26,84,92−98] Pt_3Ni,[99] ReFe,[96] RhNi,[100] and RuFe,[101] and the ternary alloys are CuFeNi,[82] and ReNiFe[96] (Figure 11). Taking into account that possible candidates of metal ex-solutes are Fe, Co, Ni, Cu, Ru, Rh, Pd, Ag, Re, Ir, Pt, and Au, among others, combinations of two to construct a binary system will number more than 66 types, emphasizing the fact that only limited alloy compounds are confirmed empirically as of the present. Therefore, dedicated computational efforts such as high-throughput DFT calculations and building databases will be important to offer key insights into the future to obtain the segregation energies of alloys from parent scaffolds, phase diagrams of multiple components, and the electronic structure of the alloy for estimations of the expected catalytic activity.[56] These databases then can be used to explore an even larger computational space by artificial intelligence. Through these efforts, a library of the alloy ex-solution process can be realized eventually, which may guide researchers to find ideal combinations of elements with optimized compositions to form ex-solved alloy catalysts.

In fact, predictions of superior alloys based on computational resources was applied in the SOFC field. For instance, Liu *et al.* conducted an *ab initio* analysis to find sulfur-tolerant material systems, such as Ni-metal (M) alloys (Figure

https://dx.doi.org/10.1021/acsnano.0c07105
ACS Nano 2021, 15, 81−110

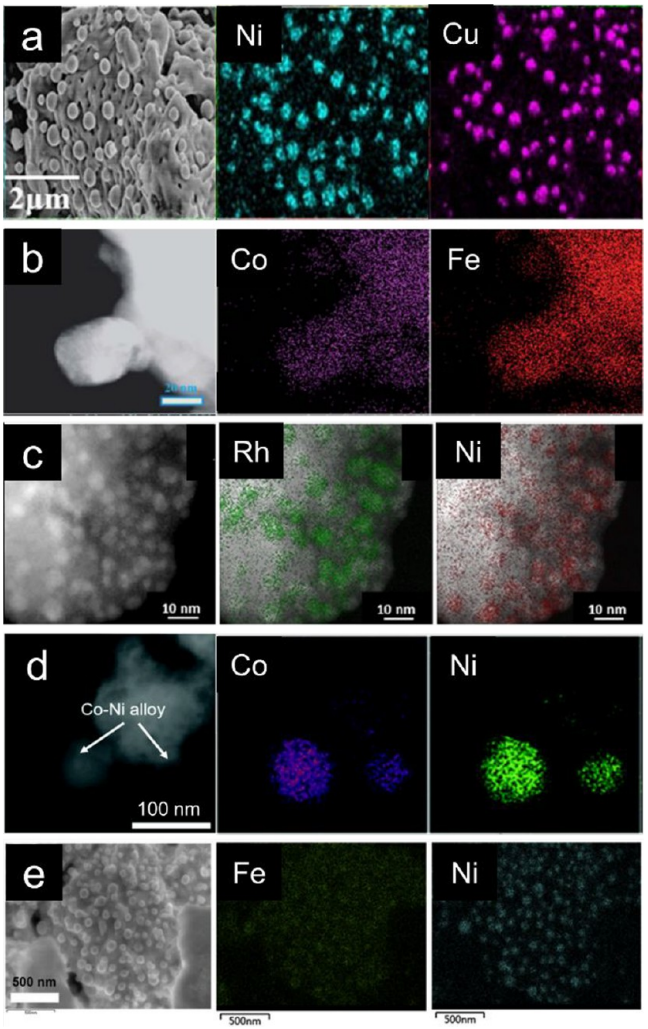

Figure 11. Reported cases of ex-solved nanoalloys discovered with EDX analysis: (a) NiCu, (b) CoFe, (c) RhNi, (d) CoNi, and (e) NiFe. Panel a reproduced with permission from ref 83. Copyright 2015 The Authors under a Creative Commons CC-BY 4.0 license, published by Springer Nature. Panel b reproduced from with permission ref 86. Copyright 2017 Royal Society of Chemistry. Panel c reproduced with permission from ref 100. Copyright 2018 American Chemical Society. Panel d reproduced with permission from ref 56. Copyright 2018 Royal Society of Chemistry. Panel e reprinted with permission from ref 98. Copyright 2018 Elsevier.

12).[77,102] According to this analysis, alloying Ni metals with Cu, Ru, Rh, Pd, and Ag may significantly lower the sulfur adsorption energy. However, it is important to note that DFT predictions do not satisfactorily explain the abnormally high sulfur-tolerance of NiFe and NiCo ex-solved nanoalloys.[10,13] On the basis of theoretical calculations, these combinations of metals should have similar, or even worse, sulfur resistance compared to Ni alone. This peculiar behavior of ex-solved alloys, which diverges from theoretical expectations, may stem from the sulfur-tolerant parent oxide or from the socket geometry, which imparts "strong-metal-support interaction". Nevertheless, the detailed mechanism is unclear and requires further scientific investigations.

The reversibility of the ex-solved alloy is also a particularly important topic to be looked at. Accordingly, Lai and Manthiram investigated the $La_{0.3}Sr_{0.7}Cr_{0.3}Fe_{0.6}Co_{0.1}O_{3-\delta}$ to investigate the regeneration mechanism of ex-solved CoFe alloy nanoparticles.[103] During the reoxidation process, it is found that temperature is of key importance to determine the reincorporation rate of the ex-solved particles. Specifically, reoxidizing the samples (which was initially reduced with 5% H_2/Ar at 700 °C) at 700 °C for 24 h with ambient air only offers a limited reincorporation rate which results in small flakes of $CoFeO_x$ remained on the parent oxide surface. However, the sample which was reoxidized at 800 °C shows a complete ingress of the ex-solved alloys. A similar conclusion was further derived from Lv *et al.*, but this time the evidence was supported with an *in situ* instrument of environmental SEM.[29] Similarly, the reoxidation of CoFe alloy leads to flat $CoFeO_x$ at 600 °C; however, when the temperature ascends to 800 °C, the irregular-shaped $CoFeO_x$ particles restored back to the parent oxides. These results give us a critical rationale on how to regenerate ex-solved alloys. While the findings are interesting, however at this moment, it is unclear that the aforementioned reoxidization mechanism will be universal to all ex-solved alloys except CoFe.

POST-TREATMENTS WITH NON-METALS FOR ENHANCING FUNCTIONALITIES

As mentioned in the previous section, the utility of ex-solved nanoparticles can be largely customized by alloying one metal to another. The aforementioned methods are primarily based on the *in situ* growth of multicomponent particles in partial reduction from the host oxide, where desired alloy-catalyst cations are already dissolved as a solid solution. In this section, we discuss post-treatments to adapt ex-solved nanoparticles to nonmetals (such as O, P, and S) to expand certain catalytic activities.

For zero-carbon emission energy, H_2 is of high significance as a future energy carrier.[104] One of the promising routes to obtain H_2 is by water splitting, and therefore great interest has been focused on developing suitable photo/electrocatalysts (*i.e.*, hydrogen evolution reaction (HER) and oxygen evolution reaction (OER)) for this application. Because the conventional Pt, Ir-based catalyst has limited scalable production stemming from the high cost and the scarcity of noble metal elements, finding non-noble metal catalysts is urgent. To date, many candidate materials, including perovskite oxides,[105−107] transition metal oxides, phosphides,[108] and sulfides[109] have been reported. Given the fact that the perovskite/metal nanoparticle interface can often be an active site to adsorb H* reaction intermediates,[110] extruding transition metal nanoparticles from the perovskite oxide support and further modifying transition metals into phosphides and/or sulfides can offer an alternative approach to design functional hybrid catalysts for water splitting. Regarding this strategy, there are a few pioneering works available in the literature. RuO_2 is known to have good catalytic activity toward the OER. To take advantage of this binary catalyst, Jiang *et al.* initially ex-solved metallic Ru from $La_{0.9}Fe_{0.92}Ru_{0.08}O_3$ and then oxidized the sample to generate RuO_2 nanoparticles anchored on perovskite oxides (Figure 13a).[111] Consequently, improved OER performance could be demonstrated with the RuO_2-perovskite hybrid catalyst. For photocatalysts, a transition metal disulfide such as WS_2 has a small band gap which encompasses the entire solar spectrum. Therefore, Sun *et al.* proposed a cocatalyst/semiconductor hybrid architecture realized by means of a postgrowth process (Figure 13b).[43] In their method, W-doped $SrTiO_3$ initially undergoes a reductive heat treatment (5% H_2/N_2 at 800 °C, 10 h) to exclude W nanoparticles. Thereafter, by treating the

https://dx.doi.org/10.1021/acsnano.0c07105
ACS Nano 2021, 15, 81−110

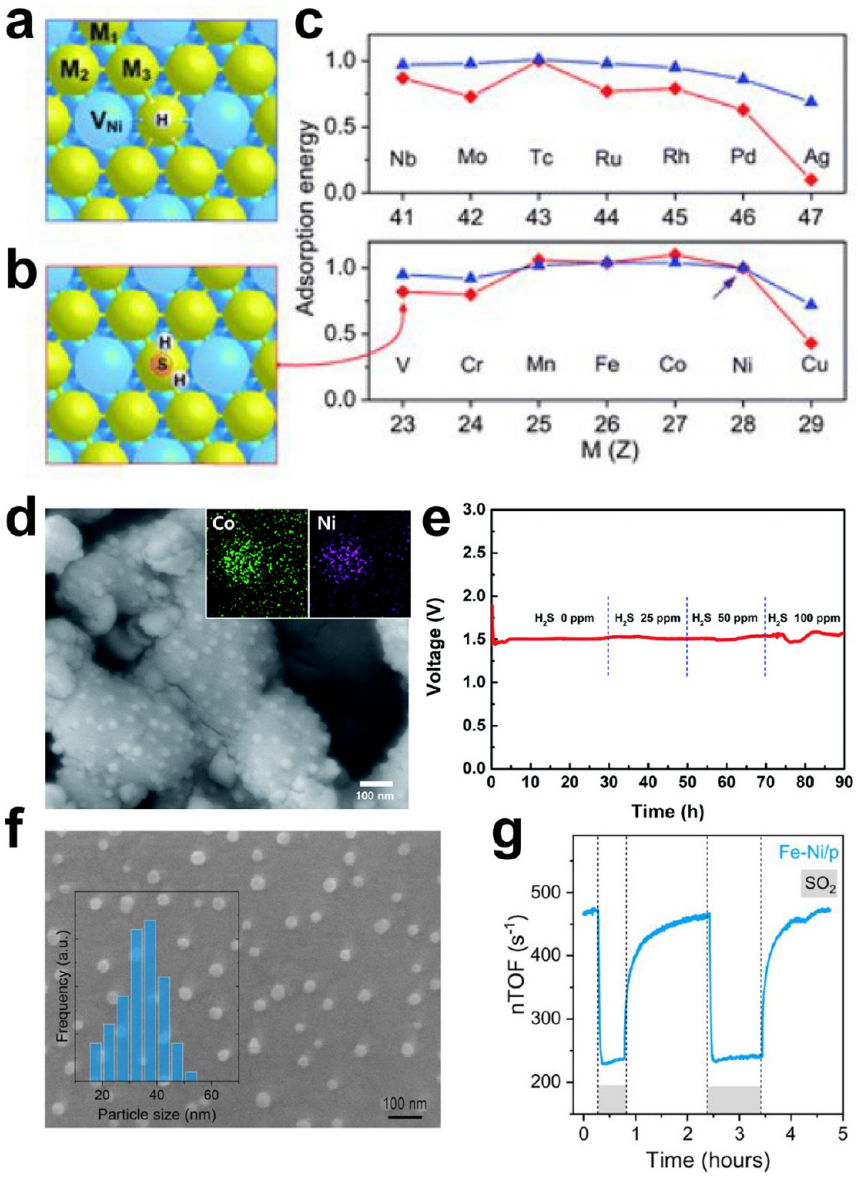

Figure 12. Top views of (a) adsorbed hydrogen and (b) adsorbed H_2S on modified Ni(111) with various 3d and 4d metals (Ni−M). Solid gray balls (V_{Ni}) are Ni defects on the topmost layer. (c) Normalized adsorption energy levels relative to that on pure Ni(111) for H_2S* (red diamonds) and H_2* (blue triangles) on modified Ni(111) with various 3d and 4d transition metals. Panels a−c reproduced with permission from 77. Copyright 2011 Royal Society of Chemistry. (d) SEM images of CoNi ex-solved $La_{1.2}Sr_{0.8}Co_{0.4}Mn_{0.6}O_4$ and EDS elemental mapping of Co and Ni. (e) Voltage profile of the single cell with the CoNi ex-solved $La_{1.2}Sr_{0.8}Co_{0.4}Mn_{0.6}O_4$ cathode at the constant current density of 700 mA cm^{-2} at 850 °C and using the reaction gas (30% CO/CO_2) streams that contain different H_2S contents. Panels d and e reproduced with permission from ref 10. Copyright 2019 Royal Society of Chemistry. (f) SEM micrographs of the catalyst surface and corresponding particle size histograms for Fe−Ni on $La_{0.5}Sr_{0.4}Fe_{0.1}Ni_{0.1}Ti_{0.6}O_3$. (g) SO_2 poisoning. nTOF values for CO_2 production during introduction of 50 ppm SO_2 in an inlet gas mixture of 0.6% CO and 1% O_2 at time intervals of 15, 30, and 60 min (gray-marked regions) over Fe−Ni on $La_{0.5}Sr_{0.4}Fe_{0.1}Ni_{0.1}Ti_{0.6}O_3$. Panels f and g reproduced with permission from ref 13. Copyright 2019 Springer Nature.

nanoparticles under a CS_2 flow, W is successfully evolved into WS_2 nanoparticles, which in turn significantly enhance the light absorption and photocatalytic performance capabilities during the HER. In another example, Wang *et al.* suggested the phosphatization of ex-solved Ni nanoparticles to form uniformly distributed Ni_2P on the perovskite oxide of $La_{0.8}Sr_{0.2}Cr_{0.69}Ni_{0.31}O_3$ to realize a bifunctional catalyst for the OER and HER.[112] By flowing H_2/Ar over excess NaH_2PO_2 at 600 °C, separately placed ex-solved Ni nanoparticles are adapted into the metal phosphide catalyst. Similarly, Zhang *et al.* reported CoP on perovskite nanofibers to optimize a multifunctional electrocatalyst based on a post-treatment of ex-solved nanoparticles (Figure 13c).[113]

While limited non-metals of O, S, and P are featured in this section, transition metal selenide (Se)[114] also has the potential to be utilized in water splitting. Furthermore, combinations of alloy ex-solutions with post-treatments, such as $Co_{1-x}Fe_xP$, may result in interesting performance outcomes.[108] Moreover, transition metal nitrides are promising candidates as NH_3 synthesis catalysts; therefore, developing a method to adapt ex-solved metal nanoparticles into metal nitrides and to evaluate the practical viability of these techniques may be exciting in the future.[115−117]

https://dx.doi.org/10.1021/acsnano.0c07105
ACS Nano 2021, 15, 81−110

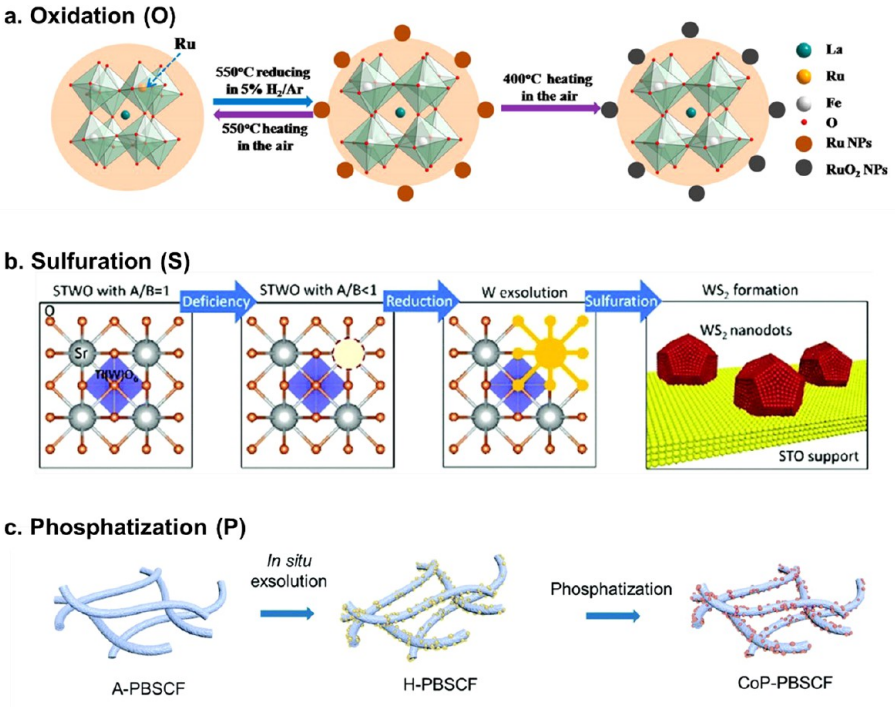

Figure 13. Series of post-treatments to adapt ex-solved metal nanoparticles into desired catalytic applications: (a) oxidation, (b) sulfuration, and (c) phophatization. Panel a reproduced with permission from ref 111. Copyright 2018 American Chemical Society. Panel b reproduced with permission from ref 43. Copyright 2018 Royal Society of Chemistry. Panel c reproduced with permission from ref 113. Copyright 2019 Royal Society of Chemistry.

ALTERNATIVE ATTEMPTS TO CREATE EX-SOLVED NANOPARTICLES

Compared to conventional particle synthesis and dispersion techniques, the ex-solution approach represents a faster and more cost-effective process with a finer particle-size distribution. While the merits of the ex-solution process are considerable, the current ex-solution technique is facing several challenges with regard to expanding it to a wider range of applications. Some of these challenges are summarized below.

(1) High-temperature/long period/reductive gas treatment compelled:

- Usually, a harsh reduction condition of balanced H_2 gas at a high temperature (>800 °C) is conducted to grow and ripen these particles; therefore, the surface area of the support is mainly sacrificed during the process of particle exclusion.
- The most frequently used reducing gas is H_2, which is an important chemical fuel in energy application. Thereby, the process may be inefficient as a lot of H_2 and heat energy (for a long period of time) is consumed.
- Often, reductive gases are flammable, imposing a potential hazard of explosion.

(2) Narrow range of support material and according possible ex-solutes elements:

- The most commonly studied host oxide is a perovskite oxide (ABO_3); there have been relatively a few attempts to ex-solve nanoparticles from other functional oxides, such as fluorites, the Ruddlesden–Popper types, and others.
- Limited numbers of transition metals can be selected to ex-solve nanoparticles. For example, the transition metals of Fe, Co, Ni, and Cu have been widely investigated;[23,83,87,118−127] however, to the best of our knowledge, the element of Mo has never been reported in relation to the ex-solution process, even though the catalytic activity of Mo can be especially appealing for the dry reforming of methane.[128]
- To fully appreciate the benefit of ex-solution, the host oxide and supposed ex-solutes should make a homogeneous solid solution. As a consequence, when the ex-solutes have insufficient solubility in host oxide, the loading amounts of nanoparticles will be largely restricted.

(3) Other drawbacks:

- Significant amounts of nanoparticles can be trapped in the host crystal. Therefore, the mass activity of metal nanoparticles can be compensated.
- Extreme reductive conditions may yield the disruption of host phase, therefore it is difficult to control the material characteristics of host oxide itself. Hence, the implementation of the ex-solution technique was hindered to the applications where reduction-vulnerable host materials are used, such as SOC air electrodes.

Due to these hurdles, researchers have endeavored to find alternative approaches to create ex-solved nanoparticles while maintaining the key virtues of anchored nanoparticles (Figure 14). In this section, valuable efforts to innovate with the ex-solution process will be appraised, while the key benefits of each method are summarized in Table 2.

ELECTROCHEMICAL SWITCHING

As mentioned earlier, reduction by hydrogen is usually conducted to achieve anchored nanoparticles. However, Myung *et al.* pointed out that this process can be tediously

https://dx.doi.org/10.1021/acsnano.0c07105
ACS Nano 2021, 15, 81−110

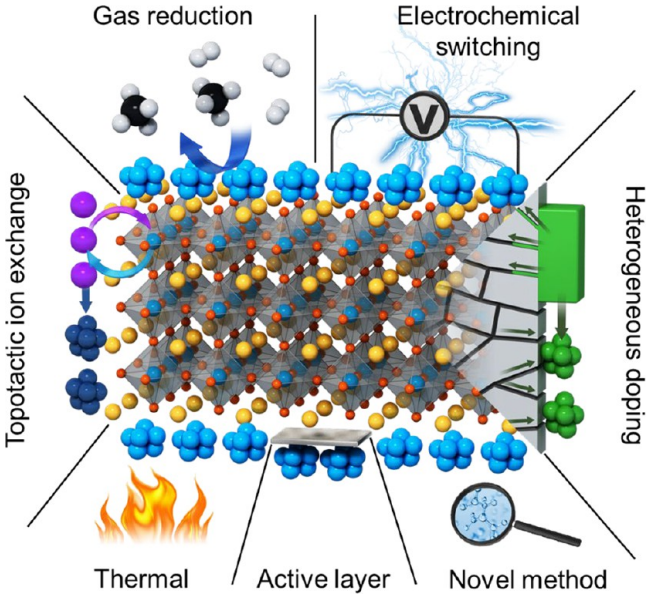

Figure 14. Alternative approaches to synthesize ex-solved nanoparticles.

Table 2. Representative Examples of Alternative Attempts to Innovate the Ex-solution Process

alternative attempts	advantages
electrochemical switching[47]	• ex-solution without the use of reducing gas
	• faster ex-solution speed
	• creating a lower oxygen partial pressure *via* voltage control which is hard to achieve with typical reducing gas
thermal reduction[129]	• ex-solution without the use of reducing gas
	• prospects on vacuum annealing, rapid thermal annealing ex-solution
heterogeneous doping[3]	• usage of grain boundary as favorable nucleation site which achieves low-temperature ex-solution
	• faster ex-solution speed
	• ex-solutes do not largely affect by solubility to host crystal which results in increased number of combinations of host and ex-solute materials
	• largely independent of loading method
active layer deposition[130−133]	• high surface areal material can be used as support
	• nanoscale ex-solution enables higher mass activity of metal catalyst
topotactic ion exchange[57,75]	• infiltrated ions fill in the ex-solute ion vacancy of host oxide, which support the phase stability of parent oxide
	• larger number density of ex-solution nanoparticles
	• prospects on alloy catalysts which cannot be achieved solely with conventional ex-solution process

sluggish (>10 h) and accordingly slow-moving ions in the oxide crystal may result in an unimpressive population of ex-solved nanoparticles. Alternately, the research team used electrical reduction (electrical bias of 2 V in 50% H_2O/N_2) which almost instantly led to a numerous amount of ex-solved nanoparticles (150 s) on $La_{0.43}Ca_{0.37}Ni_{0.06}Ti_{0.94}O_{3-\delta}$.[47] They referred to this technique as "electrochemical switching" and utilized the process to create socketed nanoparticles facilely through an applied voltage (Figure 15). Despite the shared phenomenology between hydrogen reduction and electrochemical switching, the basic science is dictated by the same law, which is the p_{O_2} gradient between the oxide and the external stimuli. Indeed, the applied voltage of 2 (2V) is estimated to be around 10^{-35} atm according to the Nernst equation, much lower than that of the typical balanced H_2 reduction (10^{-19} atm). This larger driving force may result in an ultrafast ex-solution process. In addition to the fast speed, the voltage-driven ex-solution allows one also to achieve morphology and performance superior to that of ex-solution driven by H_2 reduction. For instance, the particle density is nearly double (6.2×10^{-7} Ni nanoparticles μm^{-2} *vs* 3.7×10^{-7} Ni nanoparticles μm^{-2}), and the subsequent peak power density was increased by 7-fold (1.3 W cm^{-2} *vs* 0.2 W cm^{-2}). This brilliant concept brings forth an interesting approach to realize best-in-class reversible solid oxide cells along with a simplified and rapid preparation method. Although the aforementioned case is one in which electrochemical switching is implemented on the fuel electrode, Zhou *et al.* reported earlier that high cathodic polarization applied to a cathode material can result in similar electrochemical switching of active nanoparticles.[134] In the Ag-doped perovskite of $(La_{0.8}Sr_{0.2})_{0.95}Ag_{0.05}MnO_{3-\delta}$, Ag can be ex-solved under cathodic bias, enhancing the oxygen reduction reaction catalytic activity significantly. Therefore, the concepts presented in these studies suggest that electric bias can be a highly efficient route by which to synthesize active metal nanoparticles *operando*.

THERMALLY INDUCED EX-SOLUTION

Other than the voltage-driven ex-solution process, a thermally driven ex-solution process has been proposed as well. Tan *et al.* substituted a small portion of Gd into Ni in $Gd_xCe_{1-x}O_{2-\delta}$ (GDC) to form Ni:Gd co-doped ceria ($Gd_{1.5}Ni_{0.5}Ce_{0.8}O_{2-\delta}$, GNDC5).[129] While Ni of 5 mol % can be successfully doped into the ceria lattice, thermal annealing at 1250 °C induces the growth of NiO nanoparticles onto the GDC surface. This may be a reflection of the thermal reduction of the ceria lattice, as the elevated temperature can be the driving force to decrease the oxygen content in the oxide crystal. Indeed, the reduction of oxide (and therefore the decreasing oxygen nonstoichiometry) is typically observed as the temperature escalates because of the entropy aspect. The advantage of thermal reduction, which originates from the absence of reduction gas, has many auspicious implications. Since many reductive gases (H_2, CH_4, and so on), typically rendered as explosive and/or flammable gases, therefore inevitably accompanies the safety issues. Hence, the samples and, of course, the reaction chamber should be handled heedfully with the appropriate equipment of gas leak sensors. Therefore, finding other methodologies to avoid/minimize the usage of hazardous gases but simultaneously acquire a sufficient amount of metal nanoparticles will be critical. However, as the thermal reduction does not convey the aforementioned issues, ex-solution can be carried out more simply and has the potential to be extended as vacuum annealing to ex-solve metal nanoparticles.[65] Moreover, the ramping rate of the thermal reduction will be central to tune the growth of the nanoparticles in this case, as the sizes of the particles become smaller, while their density increases when the ramping rate increases.[40]

However, compared to reduction by H_2 or electrochemical switching, the thermally driven ex-solution process may relinquish the surface area of the support considerably, as a

https://dx.doi.org/10.1021/acsnano.0c07105
ACS Nano 2021, 15, 81−110

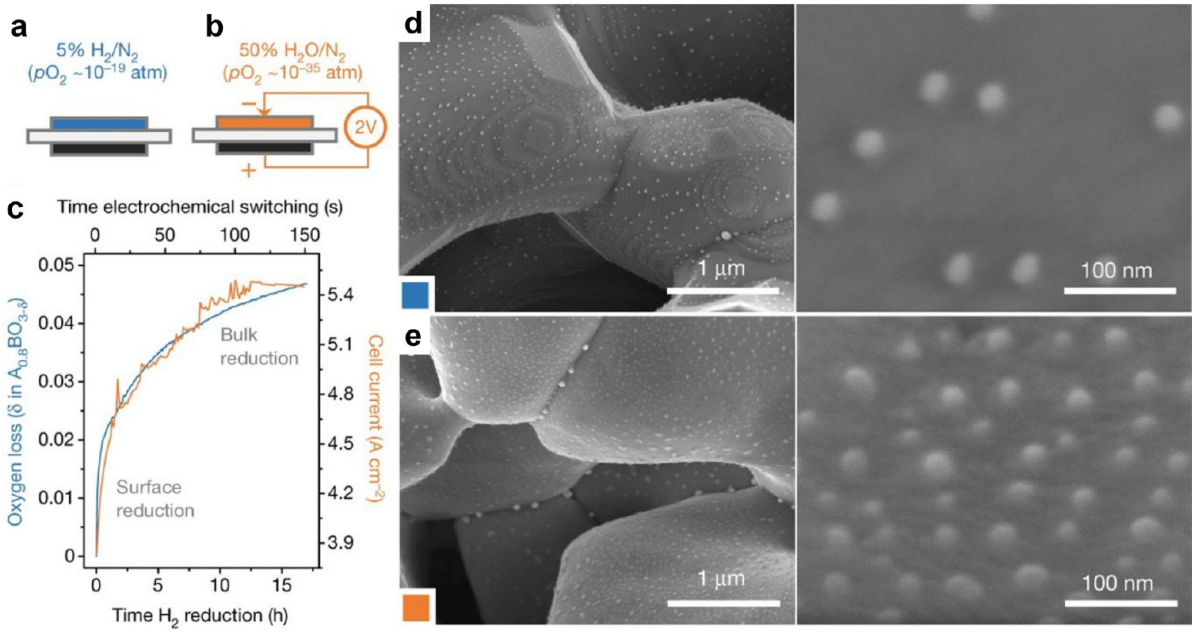

Figure 15. Electrochemical switching: conditions used to trigger ex-solution in a solid oxide electrochemical cell at the fuel electrode by (a) reduction in 5% H_2/N_2 or (b) electrochemical switching while applying 2 V across the cell. (c) In blue, thermogravimetric analysis data showing oxygen loss upon reduction by hydrogen as a function of time; in orange, cell current upon application of 2 V, also as a function of time. SEM micrographs of $La_{0.43}Ca_{0.37}Ni_{0.06}Ti_{0.94}O_{3-\delta}$ electrodes produced by (d) reduction by hydrogen at 900 °C for 20 h and (e) electrochemical switching, under 50% H_2O/N_2 at 900 °C for 150 s. Panels a–e reproduced with permission from ref 47. Copyright 2016 Springer Nature.

significantly high temperature is required to build up enough of a p_{O_2} gradient to ex-solve metal nanoparticles. Therefore, an advantage can be found where the support should be dense and compact, such as in gas separation and/or with a permeation membrane.[135] Furthermore, the thermally induced ex-solution may find merits where the extreme temperature gradient is routine such as in chemical looping combustion or solar thermal applications.[136−138]

HETEROGENEOUS DOPING

Heterogeneous doping offers another effective option by which to synthesize nanoparticles into the range of functional oxides beyond perovskite oxides, including CeO_2 and ZrO_2.[3] Heterogeneous doping refers to a methodology which involves the feeding of metal sources into the grain boundaries of oxides, where the host lattice does not intrinsically contain any metal sources (Figure 16). In this case, the metal source is initially sputtered onto the oxide and then annealed in air at 700 °C. During this process, metal cations diffuse through the grain boundaries, as cation diffusion can occur much more rapidly through the grain boundary as opposed to bulk diffusion.[139,140] These heterogeneously doped metal cations are accommodated in the crystallographically defective grain boundaries, and when a reductive heat treatment is carried out, they nucleate in the corners of the grain boundaries. Typically, it is well-known that to ex-solve particles with the stoichiometric oxide with a fluorite structure is more difficult. For example, only a small number of nanoparticles ($<5/\mu m^2$) can be confirmed in ceria surfaces. However, with heterogeneous doping, an impressive number density of nanoparticles can be formed.

Since the technique is based on grain boundary diffusion with excellent selectivity, thus the following points can be emphasized: (1) It does not require uniform coating of a metal source, (2) targeted metal ions can be uniformly distributed in the grain boundaries of the oxide only by an appropriate heat treatment, and (3) it does not require complete etching of the metal source afterward. These three aspects make this technique have general applicability which can be transferred to a variety of fields in practice to produce functional nanocrystalline oxides. Since grain boundaries have a substantially higher transitional metal storage capacity than the bulk, it is possible to produce an adequate amount of metal particles with a limited grain boundary density. Coupled with a number of state-of-the-art synthesis techniques for fabricating porous nano-polycrystalline oxide structures with high specific surface areas makes the approach practical. The methodology can be especially useful when the desired metal sources have insufficient solubility in the host oxide. Moreover, it offers the advantage of a lower ex-solution temperature (*e.g.*, 700 °C), as the grain boundary serves as a favorable spot for heterogeneous nucleation.

THIN-FILM PEROVSKITE COATING

As discussed above, one of the shortcomings of the ex-solution process is the low surface area of the perovskite support. Typically, perovskites are prepared *via* a solid-state reaction or a sol−gel method.[142,143] During the synthesis process, high-temperature calcination (*e.g.*, >900 °C) is conducted to ensure cation blending and phase purity. Hence, the surface area of the perovskite support is usually less than 10 m^2/g.[144] Additionally, a reductive heat treatment with which to grow nanoparticles will likely result in further sintering of the supporting frameworks. In other words, there is ample room for improvement in the catalytic activity if high-surface-areal perovskites are chosen to support ex-solved nanoparticles.

To address this, thin-film perovskites coated onto highly porous supports such as spinel $MgAl_2O_4$ (surface area > ~60

https://dx.doi.org/10.1021/acsnano.0c07105
ACS Nano 2021, 15, 81−110

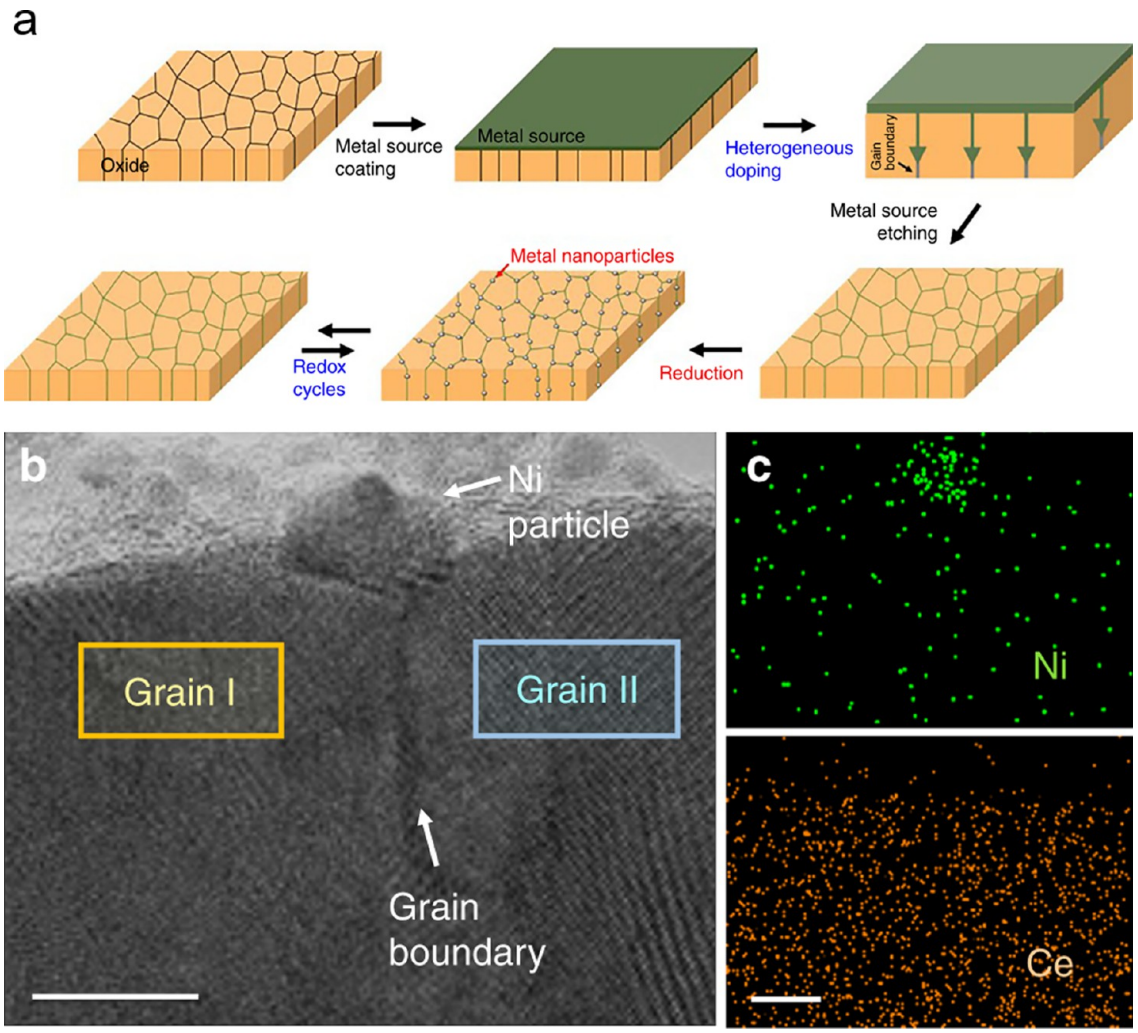

Figure 16. Heterogeneous doping: (a) synthesis of metal nanoparticles (schematic diagram of the overall synthesis procedure of metal nanoparticles and their self-regenerative tendency according to the redox cycles), (b) cross-sectional scanning transmission electron microscope (STEM) image, and (c) energy-dispersive X-ray spectroscopy (EDS) mapping results of Sm-doped CeO_2 (SDC) film with a Ni particle (scale bars; (a) 500 nm; (b, c) 10 nm). Panels a–c reproduced with permission from ref 3. Copyright 2018 The Authors under a Creative Commons CC-BY 4.0 license (https://creativecommons.org/licenses/by/4.0/), published by Springer Nature.

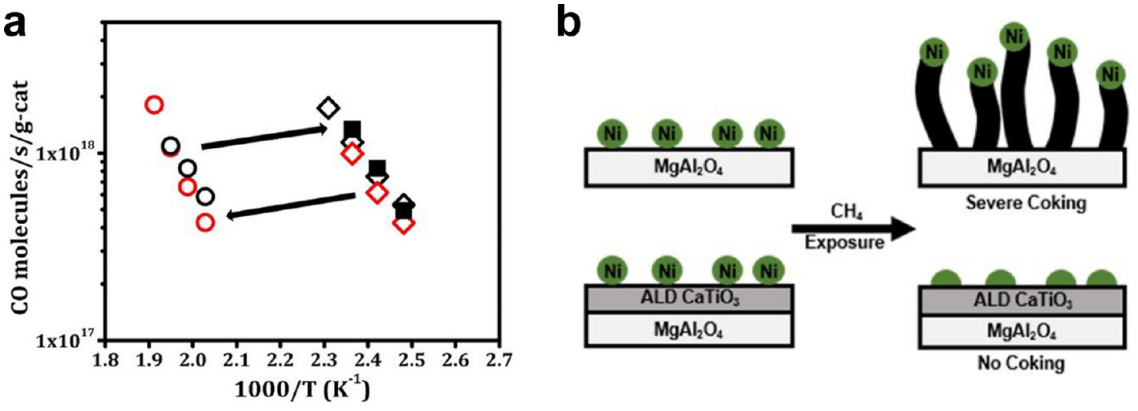

Figure 17. (a) Steady-state, differential reaction rates for CO oxidation with 25 Torr CO and 12.5 Torr O_2 for a 0.1 g sample of Pt/$LaFeO_3$/$MgAl_2O_4$. Rates measured on the as-prepared sample are marked in solid squares. Rates measured on the sample after oxidation in 10% O_2–He at 1073 K for 1 h are marked in circles; rates measured on the sample after reduction in 10% H_2–He at 1073 K for 1 h are marked in diamonds. Black symbols denote the first redox cycle, whereas red symbols denote the fifth cycle. Reproduced with permission from ref 141. Copyright 2020 American Chemical Society. (b) Schematics of illustrating the coking resistance of an intelligent catalyst supported on a thin-film perovskite which is deposited on $MgAl_2O_4$. Reproduced with permission from ref 131. Copyright 2018 American Chemical Society.

https://dx.doi.org/10.1021/acsnano.0c07105
ACS Nano 2021, 15, 81–110

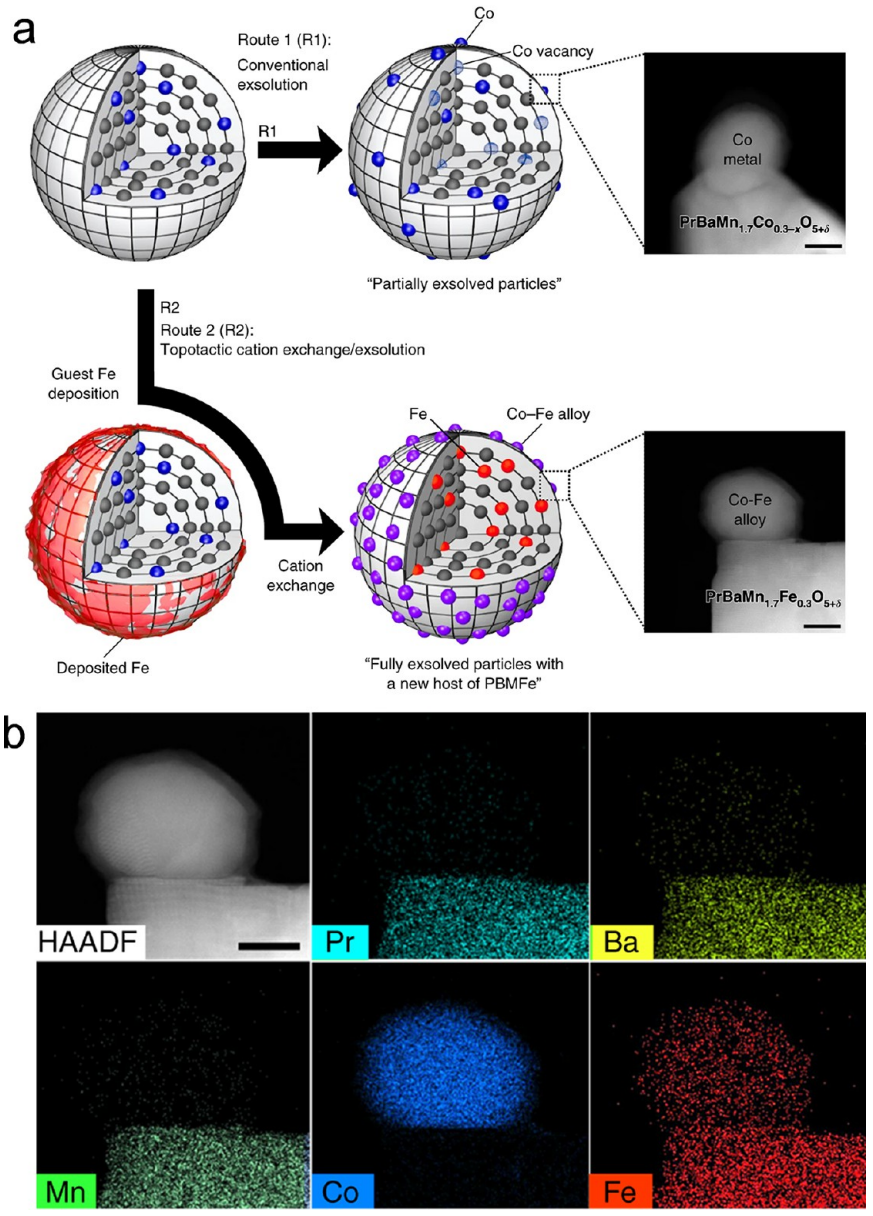

Figure 18. Topotactic ion exchange with infiltration to introduce guest cations: (a) ex-solution process without and with topotactic ion exchange of Fe guest ion on $PrBaMn_{1.7}Co_{0.3}O_{5+\delta}$. (b) EDS elemental maps of Pr, Ba, Mn, Co, and Fe (scale bar, 20 nm). Reproduced with permission from ref 57. Copyright 2019 The Authors under a Creative Commons CC-BY 4.0 license (https://creativecommons.org/licenses/by/4.0/), published by Springer Nature.

m^2/g) by means of atomic layer deposition (ALD) have been reported multiple times.[130−133] ALD has the merit of being able to create a uniform and conformal coatings that are not largely affected by the support morphology, even with pores of a low aspect ratio, making this an appropriate method for tackling this challenge.[145] With the metal nanoparticles/perovskite/$MgAl_2O_4$ configuration, encouraging demonstrations of ex-solved catalysts have been published. Indeed, nanoparticles supported on perovskite/$MgAl_2O_4$ demonstrate regenerating catalytic behavior between the redox cycle (Pt/$LaFeO_3$/ $MgAl_2O_4$, Figure 17a),[141] or anticoking capabilities (Ni/$CaTiO_3$/$MgAl_2O_4$, Figure 17b),[131] neither of which can be reproduced on nanoparticles directly supported on $MgAl_2O_4$.

TOPOTACTIC ION EXCHANGE

It has become clear lately that factors such as the modality, size, distribution, morphology, content, architecture, and catalyst−support interaction of nanoparticles are highly significant in the pursuit of ideal catalysis, and the topotactic ion-exchange process represents an important step forward for the ex-solution technique, as it encompasses the key benefits of both infiltration and ex-solution simultaneously (Figure 18).[57,146] Infiltration refers to a surface engineering technique in which a liquid solution containing stoichiometric metal salt precursors is introduced onto a prefired backbone.[147] During this process, a broad range of metal salts of varying compositions can be dissolved into the solution and subsequently fired to achieve catalyst coatings. Therefore, infiltration has advantages over the ex-solution process in terms of the selection of the catalyst material. However, optimizing

https://dx.doi.org/10.1021/acsnano.0c07105
ACS Nano 2021, 15, 81−110

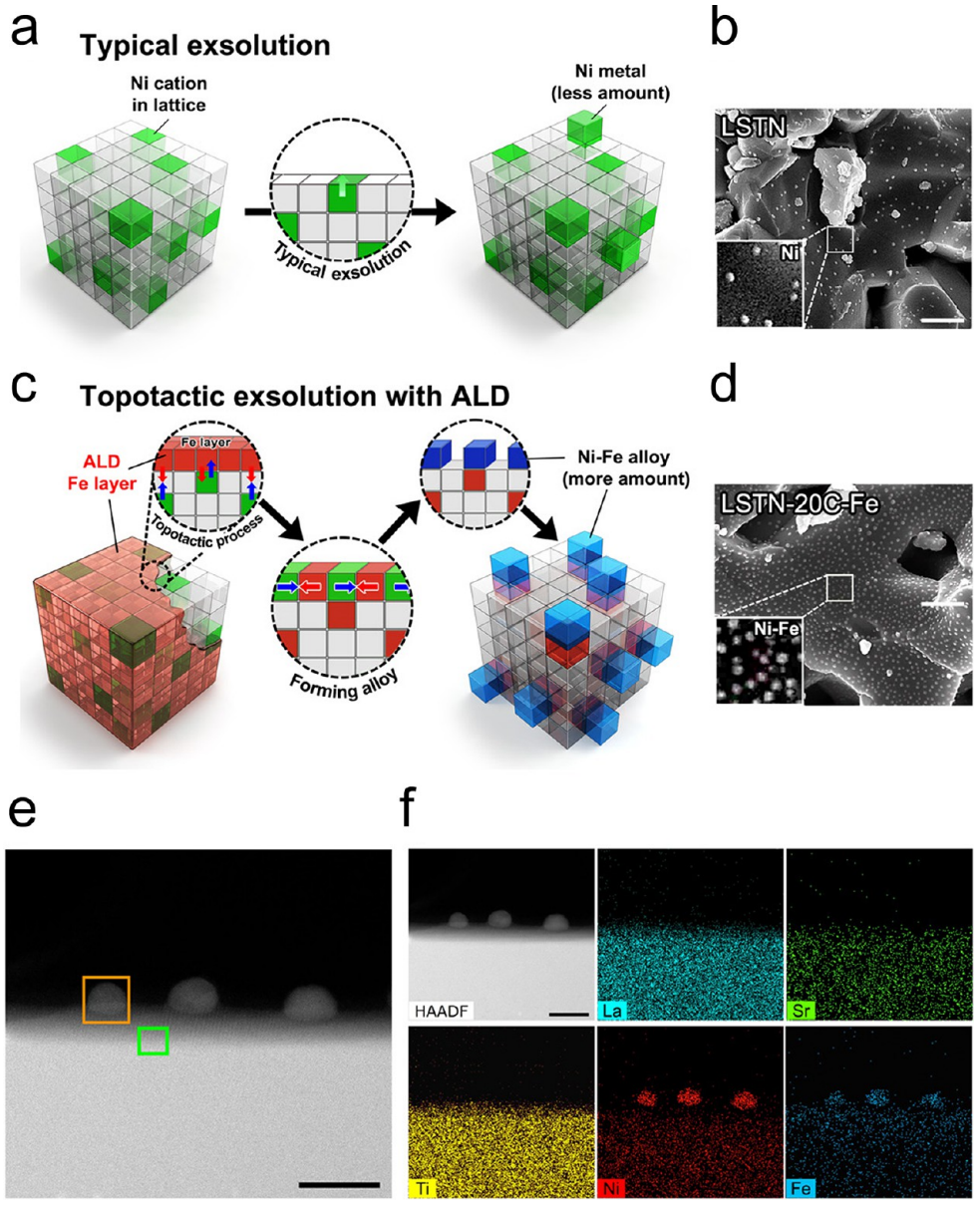

Figure 19. Topotactic ion exchange with ALD to introduce guest cations: (a) conventional ex-solution for $La_{0.6}Sr_{0.2}Ti_{0.85}Ni_{0.15}O_{3-\delta}$ (LSTN) and (b) corresponding SEM image (scale bar, 500 nm); (c) topotactic ex-solution *via* ALD for LSTN with 20 cycles of Fe deposition (LSTN-20C-Fe) and (d) corresponding SEM image (scale bar, 500 nm); (e) HAADF STEM image of LSTN-20C-Fe (scale bar, 40 nm); (f) EDS elemental map of La, Sr, Ti, Ni, and Fe (scale bar, 40 nm). Panels a–f reproduced with permission from ref 75. Copyright 2020 under a Creative Commons CC-BY 4.0 license (https://creativecommons.org/licenses/by/4.0/), published by American Association for the Advancement of Science.

the particle size and distribution through the infiltration technique can be extremely difficult and may require several instances of trial and error or several repetitions of infiltration–thermal heat cycles to procure the desired morphologies. On the other hand, the ex-solution approach is restricted in terms of the choice of materials, as previously noted. However, control over the size and distribution of the nanoparticles is superior compared to the infiltration process. In an effort to combine these critical factors, Joo *et al.* proposed the topotactic ion-exchange approach.[57] This protocol involves the following steps: (1) preparation of a porous electrode backbone which contains the ex-solute with a high segregation energy level; (2) infiltration of the guest cation with lower segregation energy; and (3) a subsequent reductive thermal treatment, where the infiltrate intercalates into the host oxide lattice while the host cations extrude onto the surface. Eventually, the ex-solute and infiltrate components form alloy catalysts *in situ*. In more detail, the authors infiltrated Fe guest cations (co-segregation energy of −0.15 eV) onto $PrBaMn_{1.7}Co_{0.3}O_{5+\delta}$ as a host oxide, during which the host cation of Co has co-segregation energy of −0.55 eV.[57] During the Co ex-solution process, a significant number of B-site vacancies can be generated, which may critically affect the ionic and electrical conduction of double perovskites. However, through a topotactic ion-exchange step, Fe guest ions are incorporated into the host lattice to fill the B-site vacancies (as Fe has low segregation energy), preserving the structure of the host oxide. Such a topotactic ion-exchange brings two advantages: (1) the ex-solution of Co would not create any B-site vacancies, thus leaving no detrimental effects on the

https://dx.doi.org/10.1021/acsnano.0c07105
ACS Nano 2021, 15, 81–110

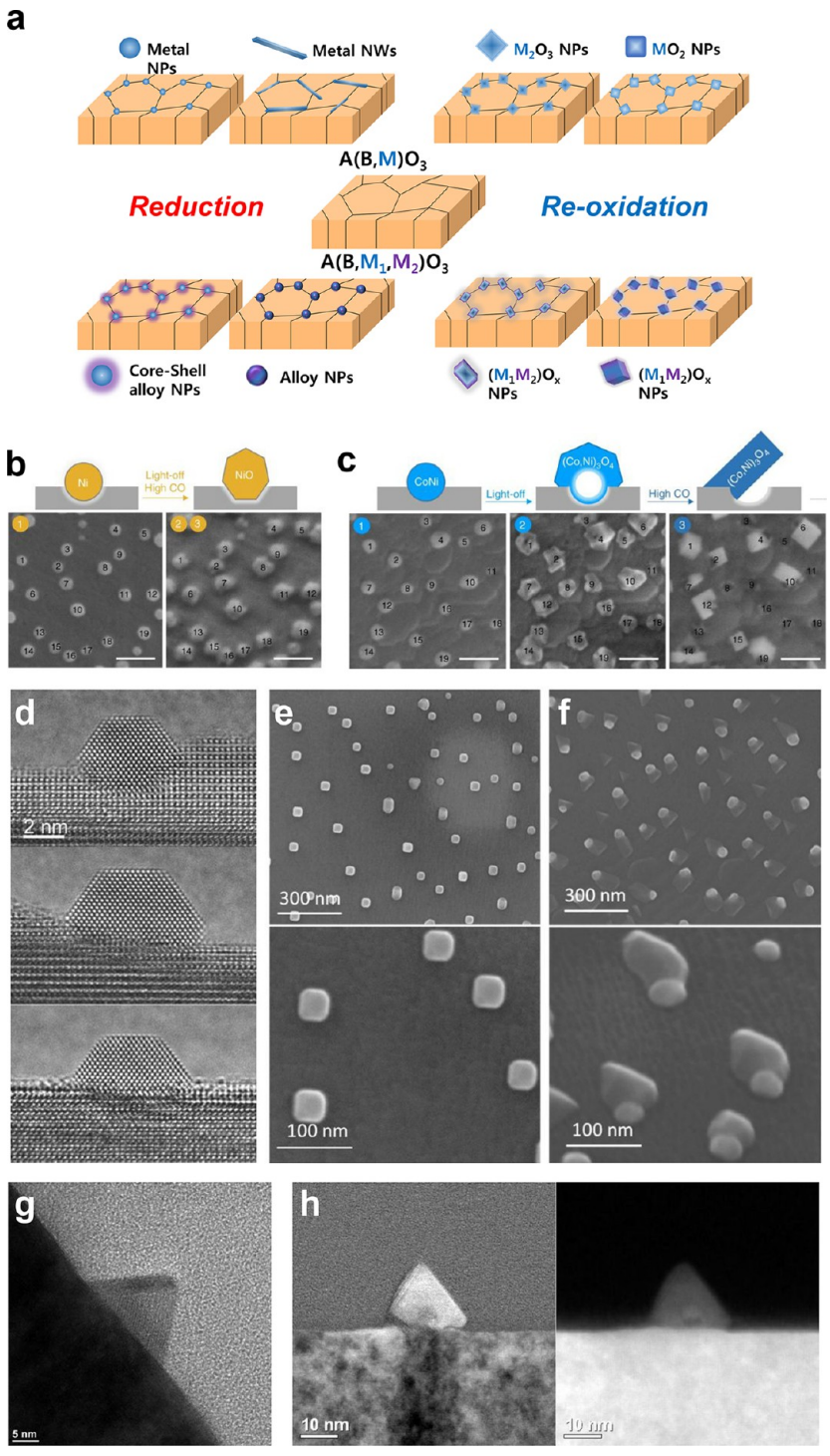

Figure 20. (a) Schematics of shape control of ex-solved nanoparticles leading to advanced nanostructures. (b) SEM micrographs of as-prepared Ni metal particles and NiO particles after light-off and CO kinetic experiments (scale bar, 100 nm). (c) SEM micrographs of as-prepared CoNi particles and after the light-off step. Cubic-like structures formed during the CO kinetic experiment and the final cube microstructure after completion of the CO kinetic experiment (scale bar, 100 nm). Panels b and c reproduced with permission from ref 91. Copyright 2017 The Authors under a Creative Commons CC-BY 4.0 license (https://creativecommons.org/licenses/by/4.0/), published by Springer Nature. (d) Faceted particles grown under a vacuum in environmental TEM at 900 °C from $La_{0.43}Ca_{0.37}Ti_{0.94}Ni_{0.06}O_3$. (e) Cubic-shaped particles grown in a 5% CO atmosphere at 900 °C for 10 h from $La_{0.8}Ce_{0.1}Ti_{0.6}Ni_{0.4}O_3$. (f) Ellipsoid-shaped particles interfaced with as-grown oxide (La_2TiO_5) in a 2.5% H_2O/5% H_2 atmosphere at 1000 °C for 10 h from $La_{0.8}Ce_{0.1}Ti_{0.6}Ni_{0.4}O_3$. Panels d–f reproduced with permission from ref 65. Copyright 2019 American Chemical Society. (g) TEM images of cone-shaped CoFe alloy nanoparticles obtained from $Sr_{0.95}Ti_{0.75}Co_{0.0125}Fe_{0.2375}O_3$ thin film after a reductive heat treatment at 750 °C and with $p_{O_2} = 10^{-23}$ atm (H_2/H_2O mixture) for 30 h. (h) TEM images of cone-shaped core–shell CoFe alloy nanoparticles obtained from $Sr_{0.95}Ti_{0.75}Co_{0.0125}Fe_{0.2375}O_3$ thin film after a reductive heat treatment of 800 °C and $p_{O_2} = 10^{-23}$ atm (H_2/H_2O mixture) for 30 h.

https://dx.doi.org/10.1021/acsnano.0c07105
ACS Nano 2021, 15, 81–110

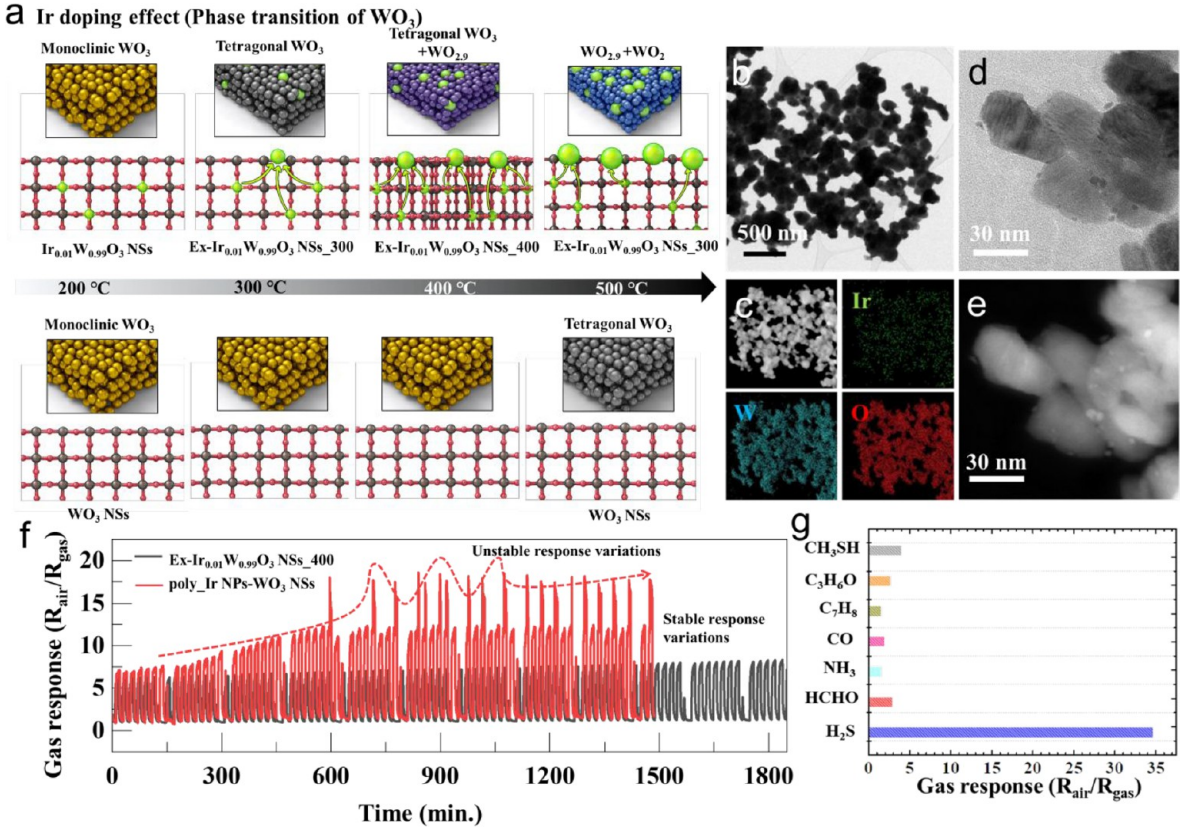

Figure 21. (a) Schematic illustration of the Ir doping effect on the phase transitions of the WO_3 host oxide. (b) Transmission electron microscopy (TEM) image of $Ir_{0.01}W_{0.99}O_3$ nanosheets (NSs). (c) Energy-dispersive X-ray spectroscopy elemental mapping analysis of $Ir_{0.01}W_{0.99}O_3$ NSs; (d) *In situ* TEM image of $Ir_{0.01}W_{0.99}O_3$ NSs annealed in 4% H_2/Ar at 300 °C (referred to as ex-$Ir_{0.01}W_{0.99}O_3$ NSs_300). (e) STEM image of ex-$Ir_{0.01}W_{0.99}O_3$ NSs_300. (f) Cyclic sensing response of ex-$Ir_{0.01}W_{0.99}O_3$ NSs_400 and Ir particles decorated WO_3 NSs at 1 ppm H_2S. (g) Selectivity characteristics of ex-$Ir_{0.01}W_{0.99}O_3$ NSs_400. Panels a−g reproduced with permission from ref 152. Copyright 2020 Wiley.

oxygen ion conduction and electron conduction paths; (2) the concentration of ex-solved Co nanoparticles would be, in principle, higher if the exchange of Co with Fe is favorable, transforming the perovskite from $PrBaMn_{1.7}Co_{0.3}O_{5+\delta}$ into $PrBaMn_{1.7}Fe_{0.3}O_{5+\delta}$. This method may lead to opportunities to utilize multiple combinations of metal cations, an advance which was impossible to achieve solely with the ex-solution process.

Recently, an advanced technique of topotactic ion-exchange ex-solution (topotactic ex-solution) was reported, which employs atomic layer deposition (ALD) instead of infiltration as a method to introducing guest cation (Figure 19).[75] As previously noted, ALD is a thin-film technique which offers a high specific surface area and fast diffusion rate of the target material which makes the material deposition with nanoscale control possible. Therefore, the guest layer introduced through ALD should be highly uniform with controlled thickness. In topotactic exchange, the diffusion rate of the deposited guest cation is an important factor. Therefore, when the guest cation is deposited through ALD, the topotactic ex-solution phenomenon can be accelerated, which produces a finely dispersed array of anchored alloy metal nanoparticles with increased population density. However, currently, only a limited assortment of metal cations can be found in the literature (*i.e.*, Ni−Fe); therefore, we hope that much attention will be directed toward this strategy to develop rationally designed, advanced catalyst systems.

OTHER OPPORTUNITIES

While the most familiar form of pinned particles is the semispherical shape, particles with exotic geometries are occasionally reported. These irregular particles are sometimes faceted, cubic, ellipsoidal, or cone-shaped with control of the type of exposure gas, p_{O_2}, and temperature. For example, by exposing ex-solved Ni particles to a CO-rich atmosphere, rounded particles evolve into more faceted ones (Figure 20b).[91] When CoNi alloy particles are exposed to a CO-rich atmosphere, however, the particles show cubic structures, presumably due to the Kirkendall effect (Figure 20c).[148−150] These examples of restructuring are not only exquisite in terms of the morphologies but also hold great promise with regard to the engineering of functional metal−metal oxides with desirable facets. Indeed, different metal facets may result in greatly distinguished catalytic activities, such as CO_2 reduction.[151] Therefore, shape control of ex-solved nanoparticles will be a fascinating topic to explore. In relation to this, Neagu *et al.* reported highly faceted Ni under high-vacuum conditions as opposed to reduction *via* H_2 (Figure 20d), while observing nanocubes on a controlled scale when CO gas is used as the reduction gas (Figure 20e).[65] Moreover, ellipsoidal particle−metal oxide heterointerfaces were achieved when balanced wet H_2 is utilized (Figure 20f). While most ex-solution processes described thus far heavily rely on balanced H_2, the aforementioned results imply that the presence of H_2 is not always required. Taking into account that myriad types of

https://dx.doi.org/10.1021/acsnano.0c07105
ACS Nano 2021, 15, 81−110

gases are available (*e.g.*, N_2, CO, CO_2, CH_4, and NH_3) for rendering mild reduction conditions, an advanced form of ex-solved nanoparticles may appear in the future (Figure 20a). Accordingly, we provide cone-shaped CoFe alloy nanoparticles grown from a PLD-$Sr_{0.95}Ti_{0.75}Co_{0.0125}Fe_{0.2375}O_3$ perovskite oxide when reduction is carried out with a rationally controlled p_{O_2} value of 10^{-23} atm at 750 °C (Figure 20g). It should be noted that when a higher temperature of 800 °C is utilized, restructuring occurs amidst the cones; therefore, a core−shell shape can arise. Again, these results emphasize the parameters pivotal for ex-solved nanoparticles when manipulating nano-architectures.

Phase-transition-induced ex-solution is another strategy that provides an important opportunity to broaden the scope of ex-solution-based applications.[153] In particular, it is believed that the reconstruction of the crystal structure in the host oxide would serve as an effective trigger for facilitating the formation of ex-solved nanoparticles. While this strategy was originally applied to the case of perovskite oxides (*i.e.*, reconstruction of ABO_3 into $AA'BB'O_6$), it was found that WO_3 is also a suitable candidate for phase-transition induced ex-solution. On the basis of this discovery, Jang *et al.* recently demonstrated a highly stable chemiresistive sensor which employs Ir as the ex-solution catalyst on two-dimensional (2D) WO_3 nanosheets (NSs).[152] Specifically, the substitution of W with Ir led to an improved reducibility of the WO_3 host oxide, enabling the ex-solution at significantly low temperatures (300 °C) as compared to those in other approaches. As shown in Figure 21a, the extraction of Ir nanoparticles from the host WO_3 at a low temperature was accelerated due to the phase transformation of the host WO_3 from monoclinic to tetragonal WO_3 and $WO_{2.9}$ phases during the reduction process. The resulting composite material, consisting of Ir nanoparticles that were tightly anchored and finely distributed on WO_3 NSs, exhibited much improved sensing performance and high stability toward the repetitive H_2S sensing compared with that of conventional sensors based on 2D WO_3 NSs decorated with Ir nanoparticles synthesized by a simple polyol route. This result offers insight on the capability of phase-transition induced ex-solution at very low temperatures, signifying their potential application as highly stable chemical sensors (Figure 21).

COMPUTATIONAL PERSPECTIVES FOR MODELING AND MATERIAL DESIGN

In the area of ex-solution, atomistic calculations have focused on understanding the mechanism underlying the energetics of nanoparticle egress. Works searching for perovskite compositions that promote the ex-solution process have yet to be reported. This may be largely due to the lack of suitable descriptors that can predict the segregation energy, E_{seg}, of B-site elements as defined in eq 10. Incidentally, a similar approach has been developed for the catalysis of oxygen reduction and evolution reactions. For perovskites, a higher electrocatalytic activity has been associated to an oxygen *p*-band center closer to the Fermi level and a smaller vacancy formation energy.[154,155] One interesting topic of future research is the construction of descriptors that correlate certain combination of bulk properties to the E_{seg} computed using the more "expensive" slab models. One possible descriptor is the grand potential difference, $\Delta\Omega$, given in eq 7.[50] One must note that $\Delta\Omega$ only depends on the bulk Helmholtz free energy and the composition. Both quantities can be obtained, in principle, from an online database (*e.g.*, Materials Project,[156] the Open Quantum Materials Database[157]).

Although existing materials databases feature thousands of compositions, only a fraction of all possible perovskites is included. Covering the entire compositional space computationally may prove to be an insurmountable task. One option to overcome this challenge is to leverage artificial intelligence (AI) by developing a trained neural network that can predict certain materials properties, such as the $\Delta\Omega$. A number of articles have emerged in the past two years on the AI-based prediction of these properties. Published neural networks include the crystal graph convolutional neural networks (CGCNN),[158,159] the SchNet,[160] and the MatErials Graph network (MEGNet).[161] In these AI-based frameworks, the crystal structures and compositions can be embedded in a given deep neural network architecture, which is capable, after training, of predicting material properties (*i.e.*, band gap, energy above hull, and so on) with an accuracy comparable to that of DFT. As such, one can use the trained neural networks to predict the descriptors, such as the $\Delta\Omega$, in a fraction of the time needed to run the DFT calculations. One giant leap forward would be the exploration of the compositional space using the trained neural network in order to optimize the perovskite composition. One should also note that this approach can further be extended to other properties, including the formation energies of O vacancies, and migration barriers of B-site metals provided that the databases used for training the networks are appropriately expanded.

To unravel the mechanism behind ex-solution, atomistic models have played an important role. However, the computational effort required by such models renders them impractical if they are enlarged beyond a few hundred atoms. In fact, DFT computations scale cubically with the number of electrons, making conventional computations prohibitive even with a thousand atoms. Furthermore, conventional DFT calculates ground-state densities and is therefore not suitable to reveal kinetic or dynamic processes taking place during the ex-solution. To handle the kinetics, molecular dynamics (MD) simulations can be used. However, due to their computational complexity, *ab initio* MD simulations are typically limited to only a few hundreds of atoms. This constraint may be alleviated by artificial intelligence. Indeed, machine-learning-based force fields can accelerate force evaluations, thereby enabling simulations of larger systems. Researchers have leveraged generalized neural networks,[162] Bayesian inference,[163] and least absolute shrinkage and selection operator (LASSO)[164] to devise force fields. Despite their significant promise, MD simulations, even in the least computationally taxing scenario, are restrained to runs of less than a few hundreds of nanoseconds. These time scales are too short to successfully model the ex-solution dynamics.[165] In contrast, continuum models are time efficient. However, they suffer from inadequate accuracy, particularly when defects are involved.[166] Bridging microscale and macroscale models is key for capturing the macroscopic behavior while representing accurately the microscale kinetics of the system. To this end, multiscale models, that have been developed for other fields, could be used to accurately model microscopic models while retaining the needed speed.[166,167]

Bridging the gap between experimental and atomistic time scales is possible if the phase-field crystal (PFC) model is used.

https://dx.doi.org/10.1021/acsnano.0c07105
ACS Nano 2021, 15, 81−110

The PFC framework can describe the crystal evolution and self-organization,[168] linking atomic and mesoscopic scales.[169] In fact, this method combines thermodynamics at the atomic scale with diffusional time scales typical of phase transformations.[165,168,170,171] Importantly, due to their ease of implementation and lower computational burden compared to MD simulations, PFC models can be run over relatively large length scales and time scales,[168] making them well-suited to ex-solution modeling. Potential applications include combining PFC models and *in situ* characterizations. A similar strategy has been implemented in the metallurgy literature, where integrating phase-field models were integrated with *operando* X-ray tomography.[172] Combining PFC simulations with real-time observation (*e.g.*, with *in situ* TEM) and control of nanoparticle size can ultimately unravel the mechanisms underpinning ex-solution. The resulting insights would be a cornerstone for advancing the field, ultimately allowing the PFC method to design compositions that lead to optimal nanoparticle size and coverage.

CONCLUDING REMARKS

Through these different examples, it is now clear that the ex-solution process has invigorated a tremendous number of chemical-electrochemical applications along with valuable academic investigations. Indeed, various parent oxide materials and different combinations of metal nanoparticles have been examined with the ex-solution technique to demonstrate markedly promoted catalytic properties. However, even with these great contributions, the full potential of the ex-solution process is yet to be unlocked, and more research is therefore imperative. Given this perspective, we provide milestones here for researchers who seek to improve the functionality and broaden the applications of the ex-solution technique. Additionally, alternative attempts to push the limits of the current ex-solution process have been reviewed. Each and every attempt critically loosened the constraints of current techniques; therefore, the aforementioned problems of engaging H_2 reductions or the limited choice of the parent oxide and/or ex-solute have largely been overcome. The concurrent implementation of the featured techniques may develop intriguing and improved results in the future as well. Nevertheless, the application of the ex-solution process has thus far exceedingly focused on fuel electrodes, with relatively scant attention paid to air electrodes to utilize the electrocatalytic value of anchored nanoparticles.[143,173] The authors firmly believe that hitherto unknown strategies to obtain extruded nanoparticles under more oxidizing conditions will expand the boundaries of ex-solution technology even further.

AUTHOR INFORMATION

Corresponding Authors

WooChul Jung − *Department of Materials Science and Engineering, Korea Advanced Institute of Science and Technology (KAIST), Daejeon 34141, Republic of Korea;* orcid.org/0000-0001-5266-3795; Email: wcjung@kaist.ac.kr

Francesco Ciucci − *Department of Mechanical and Aerospace Engineering and Department of Chemical and Biological Engineering, The Hong Kong University of Science and Technology, Kowloon, Hong Kong, China;* Email: francesco.ciucci@ust.hk

Authors

Jun Hyuk Kim − *Department of Materials Science and Engineering, Korea Advanced Institute of Science and Technology (KAIST), Daejeon 34141, Republic of Korea*

Jun Kyu Kim − *Department of Materials Science and Engineering, Korea Advanced Institute of Science and Technology (KAIST), Daejeon 34141, Republic of Korea*

Jiapeng Liu − *Department of Mechanical and Aerospace Engineering, The Hong Kong University of Science and Technology, Kowloon, Hong Kong, China;* orcid.org/0000-0001-8667-1929

Antonino Curcio − *Department of Mechanical and Aerospace Engineering, The Hong Kong University of Science and Technology, Kowloon, Hong Kong, China*

Ji-Soo Jang − *Department of Materials Science and Engineering, Korea Advanced Institute of Science and Technology (KAIST), Daejeon 34141, Republic of Korea;* orcid.org/0000-0001-6018-7231

Il-Doo Kim − *Department of Materials Science and Engineering, Korea Advanced Institute of Science and Technology (KAIST), Daejeon 34141, Republic of Korea;* orcid.org/0000-0002-9970-2218

Complete contact information is available at: https://pubs.acs.org/10.1021/acsnano.0c07105

Author Contributions

[‖]J.H.K., J.K.K., and J.L. contributed equally to this work.

Notes

The authors declare no competing financial interest.

ACKNOWLEDGMENTS

This work was supported by Samsung Research Funding & Incubation Center of Samsung Electronics under Project No. SRFC-MA1502-52 and the National Research Foundations of Korea (NRF), Grant No. 2019M3D1A2104100. Also, F.C., A.C., and J.L. gratefully acknowledge the support from the Research Grants Council of Hong Kong through the General Research Fund projects 16227016, 16204517, and 16206019. A.C. also thanks the Hong Kong PhD Fellowship for financial support.

VOCABULARY

Alloy, combination of metals or metals with one or more other elements; Ex-solution, spontaneous emergence of metal (in some cases, oxide) nanoparticles onto the oxide supports; Heterogeneous catalysis, catalysis where the phase of catalysts differs from that of the reactants or products; Nucleation, the first step in the formation of either a new thermodynamic phase or a new structure; Point defects, deviations from the perfect atomic arrangement such as missing ions, substituted ions, interstitial ions, and their associated valence electrons in all crystalline materials

REFERENCES

(1) Koo, B.; Kim, K.; Kim, J. K.; Kwon, H.; Han, J. W.; Jung, W. Sr Segregation in Perovskite Oxides: Why It Happens and How It Exists. *Joule* **2018**, *2* (8), 1476−1499.

(2) van Deelen, T. W.; Hernández Mejía, C.; de Jong, K. P. Control of Metal-Support Interactions in Heterogeneous Catalysts to Enhance Activity and Selectivity. *Nat. Catal.* **2019**, *2* (11), 955−970.

(3) Kwak, N. W.; Jeong, S. J.; Seo, H. G.; Lee, S.; Kim, Y.; Kim, J. K.; Byeon, P.; Chung, S. Y.; Jung, W. *In Situ* Synthesis of Supported

Metal Nanocatalysts through Heterogeneous Doping. *Nat. Commun.* **2018**, *9* (1), 4829.
(4) Li, X.; Dai, L.; He, Z.; Meng, W.; Li, Y.; Wang, L. Enhancing NH_3 Sensing Performance of Mixed Potential Type Sensors by Chemical Exsolution of Ag Nanoparticle on $AgNbO_3$ Sensing Electrode. *Sens. Actuators, B* **2019**, *298*, 126854.
(5) Kyriakou, V.; Neagu, D.; Papaioannou, E. I.; Metcalfe, I. S.; van de Sanden, M. C. M.; Tsampas, M. N. Co-electrolysis of H_2O and CO_2 on Exsolved Ni Nanoparticles for Efficient Syngas Generation at Controllable H_2/CO Ratios. *Appl. Catal., B* **2019**, *258*, 117950.
(6) Nishihata, Y.; Mizuki, J.; Akao, T.; Tanaka, H.; Uenishi, M.; Kimura, M.; Okamoto, T.; Hamada, N. Self-Regeneration of a Pd-Perovskite Catalyst for Automotive Emissions Control. *Nature* **2002**, *418* (6894), 164−167.
(7) Irvine, J. T. S.; Neagu, D.; Verbraeken, M. C.; Chatzichristodoulou, C.; Graves, C.; Mogensen, M. B. Evolution of the Electrochemical Interface in High-Temperature Fuel Cells and Electrolysers. *Nat. Energy* **2016**, *1*, 15014.
(8) Jeon, Y.; Ji, Y.; Cho, Y. I.; Lee, C.; Park, D. H.; Shul, Y. G. Oxide-Carbon Nanofibrous Composite Support for a Highly Active and Stable Polymer Electrolyte Membrane Fuel-Cell Catalyst. *ACS Nano* **2018**, *12* (7), 6819−6829.
(9) Newton, M. A. Dynamic Adsorbate/Reaction Induced Structural Change of Supported Metal Nanoparticles: Heterogeneous Catalysis and Beyond. *Chem. Soc. Rev.* **2008**, *37* (12), 2644−2657.
(10) Park, S.; Kim, Y.; Noh, Y.; Kim, T.; Han, H.; Yoon, W.; Choi, J.; Yi, S.-H.; Lee, W.-J.; Kim, W. B. A Sulfur-Tolerant Cathode Catalyst Fabricated with *in Situ* Exsolved CoNi Alloy Nanoparticles Anchored on a Ruddlesden-Popper Support for CO_2 Electrolysis. *J. Mater. Chem. A* **2020**, *8* (1), 138−148.
(11) Neagu, D.; Oh, T. S.; Miller, D. N.; Menard, H.; Bukhari, S. M.; Gamble, S. R.; Gorte, R. J.; Vohs, J. M.; Irvine, J. T. S. Nano-Socketed Nickel Particles with Enhanced Coking Resistance Grown *in Situ* by Redox Exsolution. *Nat. Commun.* **2015**, *6*, 8120.
(12) Oh, T. S.; Rahani, E. K.; Neagu, D.; Irvine, J. T.; Shenoy, V. B.; Gorte, R. J.; Vohs, J. M. Evidence and Model for Strain-Driven Release of Metal Nanocatalysts from Perovskites during Exsolution. *J. Phys. Chem. Lett.* **2015**, *6* (24), 5106−5110.
(13) Papaioannou, E. I.; Neagu, D.; Ramli, W. K. W.; Irvine, J. T. S.; Metcalfe, I. S. Sulfur-Tolerant, Exsolved Fe-Ni Alloy Nanoparticles for CO Oxidation. *Top. Catal.* **2019**, *62* (17−20), 1149−1156.
(14) Neagu, D.; Tsekouras, G.; Miller, D. N.; Menard, H.; Irvine, J. T. *In Situ* Growth of Nanoparticles through Control of Non-Stoichiometry. *Nat. Chem.* **2013**, *5* (11), 916−923.
(15) Zhao, C.; Li, Y.; Zhang, W.; Zheng, Y.; Lou, X.; Yu, B.; Chen, J.; Chen, Y.; Liu, M.; Wang, J. Heterointerface Engineering for Enhancing the Electrochemical Performance of Solid Oxide Cells. *Energy Environ. Sci.* **2020**, *13*, 53−85.
(16) Zhu, Y.; Liu, X.; Jin, S.; Chen, H.; Lee, W.; Liu, M.; Chen, Y. Anionic Defect Engineering of Transition Metal Oxides for Oxygen Reduction and Evolution Reactions. *J. Mater. Chem. A* **2019**, *7* (11), 5875−5897.
(17) Li, Y.; Zhang, W.; Zheng, Y.; Chen, J.; Yu, B.; Chen, Y.; Liu, M. Controlling Cation Segregation in Perovskite-Based Electrodes for High Electro-Catalytic Activity and Durability. *Chem. Soc. Rev.* **2017**, *46* (20), 6345−6378.
(18) Kwon, O.; Joo, S.; Choi, S.; Sengodan, S.; Kim, G. Review on Exsolution and Its Driving Forces in Perovskites. *JPhys. Energy* **2020**, *2*, 032001.
(19) Tsekouras, G.; Neagu, D.; Irvine, J. T. Step-Change in High Temperature Steam Electrolysis Performance of Perovskite Oxide Cathodes with Exsolution of B-Site Dopants. *Energy Environ. Sci.* **2013**, *6* (1), 256−266.
(20) Schmalzried, H.; Backhaus-Ricoult, M. Internal Solid State Reactions. *Prog. Solid State Chem.* **1993**, *22* (1), 1−57.
(21) Takehira, K. Highly Dispersed and Stable Supported Metal Catalysts Prepared by Solid Phase Crystallization Method. *Catal. Surv. Asia* **2002**, *6* (1−2), 19−32.
(22) Madsen, B. D.; Kobsiriphat, W.; Wang, Y.; Marks, L. D.; Barnett, S. A. Nucleation of Nanometer-Scale Electrocatalyst Particles in Solid Oxide Fuel Cell Anodes. *J. Power Sources* **2007**, *166* (1), 64−67.
(23) Du, Z.; Zhao, H.; Yi, S.; Xia, Q.; Gong, Y.; Zhang, Y.; Cheng, X.; Li, Y.; Gu, L.; Swierczek, K. High-Performance Anode Material $Sr_2FeMo_{0.65}Ni_{0.35}O_{6-\delta}$ with *in Situ* Exsolved Nanoparticle Catalyst. *ACS Nano* **2016**, *10* (9), 8660−8669.
(24) Kim, K. J.; Rath, M. K.; Kwak, H. H.; Kim, H. J.; Han, J. W.; Hong, S.-T.; Lee, K. T. A Highly Active and Redox-Stable $SrGdNi_{0.2}Mn_{0.8}O_{4\pm\delta}$ Anode with *in Situ* Exsolution of Nanocatalysts. *ACS Catal.* **2019**, *9* (2), 1172−1182.
(25) Xue, S.; Shi, N.; Wan, Y.; Xu, Z.; Huan, D.; Zhang, S.; Xia, C.; Peng, R.; Lu, Y. Novel Carbon and Sulfur-Tolerant Anode Material $FeNi_3$@$PrBa(Fe,Ni)_{1.9}Mo_{0.1}O_{5+\delta}$ for Intermediate Temperature Solid Oxide Fuel Cells. *J. Mater. Chem. A* **2019**, *7* (38), 21783−21793.
(26) Zhu, T.; Troiani, H. E.; Mogni, L. V.; Han, M.; Barnett, S. A. Ni-Substituted $Sr(Ti, Fe)O_3$ SOFC Anodes: Achieving High Performance *via* Metal Alloy Nanoparticle Exsolution. *Joule* **2018**, *2* (3), 478−496.
(27) Li, Y.; Xie, K.; Chen, S.; Li, H.; Zhang, Y.; Wu, Y. Efficient Carbon Dioxide Electrolysis Based on Perovskite Cathode Enhanced with Nickel Nanocatalyst. *Electrochim. Acta* **2015**, *153*, 325−333.
(28) Park, S.; Kim, Y.; Han, H.; Chung, Y. S.; Yoon, W.; Choi, J.; Kim, W. B. *In Situ* Exsolved Co Nanoparticles on Ruddlesden-Popper Material as Highly Active Catalyst for CO_2 Electrolysis to CO. *Appl. Catal., B* **2019**, *248*, 147−156.
(29) Lv, H.; Lin, L.; Zhang, X.; Song, Y.; Matsumoto, H.; Zeng, C.; Ta, N.; Liu, W.; Gao, D.; Wang, G.; Bao, X. *In Situ* Investigation of Reversible Exsolution/Dissolution of CoFe Alloy Nanoparticles in a Co-Doped $Sr_2Fe_{1.5}Mo_{0.5}O_{6-\delta}$ Cathode for CO_2 Electrolysis. *Adv. Mater.* **2020**, *32*, 1906193.
(30) Liu, T.; Zhao, Y.; Zhang, X.; Zhang, H.; Jiang, G.; Zhao, W.; Guo, J.; Chen, F.; Yan, M.; Zhang, Y.; Wang, Y. Robust Redox-Reversible Perovskite Type Steam Electrolyser Electrode Decorated with *in Situ* Exsolved Metallic Nanoparticles. *J. Mater. Chem. A* **2020**, *8* (2), 582−591.
(31) Qi, W.; Ruan, C.; Wu, G.; Zhang, Y.; Wang, Y.; Xie, K.; Wu, Y. Reversibly *in Situ* Anchoring Copper Nanocatalyst in Perovskite Titanate Cathode for Direct High-Temperature Steam Electrolysis. *Int. J. Hydrogen Energy* **2014**, *39* (11), 5485−5496.
(32) Zhu, C.; Hou, S.; Hu, X.; Lu, J.; Chen, F.; Xie, K. Electrochemical Conversion of Methane to Ethylene in a Solid Oxide Electrolyzer. *Nat. Commun.* **2019**, *10* (1), 1173.
(33) Papargyriou, D.; Miller, D. N.; Sirr Irvine, J. T. Exsolution of Fe-Ni Alloy Nanoparticles from $(La,Sr)(Cr,Fe,Ni)O_3$ Perovskites as Potential Oxygen Transport Membrane Catalysts for Methane Reforming. *J. Mater. Chem. A* **2019**, *7* (26), 15812−15822.
(34) Dimitrakopoulos, G.; Ghoniem, A. F.; Yildiz, B. *In Situ* Catalyst Exsolution on Perovskite Oxides for the Production of CO and Synthesis Gas in Ceramic Membrane Reactors. *Sustain. Energy Fuels* **2019**, *3* (9), 2347−2355.
(35) Zeng, D.; Cui, D.; Lv, Y.; Qiu, Y.; Li, M.; Zhang, S.; Xiao, R. A Mixed Spinel Oxygen Carrier with Both High Reduction Degree and Redox Stability for Chemical Looping H_2 Production. *Int. J. Hydrogen Energy* **2020**, *45* (3), 1444−1452.
(36) Hosseini, D.; Donat, F.; Abdala, P. M.; Kim, S. M.; Kierzkowska, A. M.; Muller, C. R. Reversible Exsolution of Dopant Improves the Performance of $Ca_2Fe_2O_5$ for Chemical Looping Hydrogen Production. *ACS Appl. Mater. Interfaces* **2019**, *11* (20), 18276−18284.
(37) Cui, D.; Qiu, Y.; Lv, Y.; Li, M.; Zhang, S.; Tippayawong, N.; Zeng, D.; Xiao, R. A High-Performance Oxygen Carrier with High Oxygen Transport Capacity and Redox Stability for Chemical Looping Combustion. *Energy Convers. Manage.* **2019**, *202*, 112209.
(38) Tang, C.; Kousi, K.; Neagu, D.; Portoles, J.; Papaioannou, E. I.; Metcalfe, I. S. Towards Efficient Use of Noble Metals *via* Exsolution Exemplified for CO Oxidation. *Nanoscale* **2019**, *11* (36), 16935−16944.

https://dx.doi.org/10.1021/acsnano.0c07105
ACS Nano 2021, 15, 81−110

(39) Jo, Y. R.; Koo, B.; Seo, M. J.; Kim, J. K.; Lee, S.; Kim, K.; Han, J. W.; Jung, W.; Kim, B. J. Growth Kinetics of Individual Co Particles Ex-Solved on $SrTi_{0.75}Co_{0.25}O_{3-\delta}$ Polycrystalline Perovskite Thin Films. *J. Am. Chem. Soc.* **2019**, *141* (16), 6690−6697.
(40) Kim, J. K.; Jo, Y.-R.; Kim, S.; Koo, B.; Kim, J. H.; Kim, B.-J.; Jung, W. Exceptional Tunability over Size and Density of Spontaneously Formed Nanoparticles *via* Nucleation Dynamics. *ACS Appl. Mater. Interfaces* **2020**, *12* (21), 24039−24047.
(41) Lee, J. G.; Myung, J. H.; Naden, A. B.; Jeon, O. S.; Shul, Y. G.; Irvine, J. T. Replacement of Ca by Ni in a Perovskite Titanate to Yield a Novel Perovskite Exsolution Architecture for Oxygen-Evolution Reactions. *Adv. Energy Mater.* **2020**, *10* (10), 1903693 1−6.
(42) Yu, J.; Zhang, L.; Qian, J.; Zhu, Z.; Ni, S.; Liu, G.; Xu, X. *In Situ* Exsolution of Silver Nanoparticles on $AgTaO_3$-$SrTiO_3$ Solid Solutions as Efficient Plasmonic Photocatalysts for Water Splitting. *Appl. Catal., B* **2019**, *256*, 117818.
(43) Sun, Y. F.; Yang, Y. L.; Chen, J.; Li, M.; Zhang, Y. Q.; Li, J. H.; Hua, B.; Luo, J. L. Toward a Rational Photocatalyst Design: A New Formation Strategy of Co-Catalyst/Semiconductor Heterostructures *via in Situ* Exsolution. *Chem. Commun. (Cambridge, U. K.)* **2018**, *54* (12), 1505−1508.
(44) Gao, Y.; Chen, D.; Saccoccio, M.; Lu, Z.; Ciucci, F. From Material Design to Mechanism Study: Nanoscale Ni Exsolution on a Highly Active A-Site Deficient Anode Material for Solid Oxide Fuel Cells. *Nano Energy* **2016**, *27*, 499−508.
(45) Lai, K.-Y.; Manthiram, A. Self-Regenerating Co-Fe Nanoparticles on Perovskite Oxides as a Hydrocarbon Fuel Oxidation Catalyst in Solid Oxide Fuel Cells. *Chem. Mater.* **2018**, *30* (8), 2515−2525.
(46) Ma, Q.; Tietz, F.; Stöver, D. Nonstoichiometric Y-Substituted SrTiO3Materials as Anodes for Solid Oxide Fuel Cells. *Solid State Ionics* **2011**, *192* (1), 535−539.
(47) Myung, J. H.; Neagu, D.; Miller, D. N.; Irvine, J. T. Switching On Electrocatalytic Activity in Solid Oxide Cells. *Nature* **2016**, *537* (7621), 528−531.
(48) Hamada, I.; Uozumi, A.; Morikawa, Y.; Yanase, A.; Katayama-Yoshida, H. A Density Functional Theory Study of Self-Regenerating Catalysts $LaFe_{1-x}M_xO_{3-y}$ (M = Pd, Rh, Pt). *J. Am. Chem. Soc.* **2011**, *133* (46), 18506−18509.
(49) Kizaki, H.; Kusakabe, K.; Nogami, S.; Katayama-Yoshida, H. Generation of Nano-Catalyst Particles by Spinodal Nano-Decomposition in Perovskite. *Appl. Phys. Express* **2008**, *1*, 104001.
(50) Yanagisawa, S.; Uozumi, A.; Hamada, I.; Morikawa, Y. Search for a Self-Regenerating Perovskite Catalyst Using *ab Initio* Thermodynamics Calculations. *J. Phys. Chem. C* **2013**, *117* (3), 1278−1286.
(51) TAN, I.; TANAKA, H.; UENISHI, M.; KANEKO, K.; MITACHI, S. Structural Stability of Pd-Perovskite Catalysts after Heat Treatment under Redox Condition. *Nippon Seramikkusu Kyokai Gakujutsu Ronbunshi* **2005**, *113* (1313), 71−76.
(52) Tanaka, H.; Taniguchi, M.; Uenishi, M.; Kajita, N.; Tan, I.; Nishihata, Y.; Mizuki, J. i.; Narita, K.; Kimura, M.; Kaneko, K. Self-Regenerating Rh-and Pt-Based Perovskite Catalysts for Automotive-Emissions Control. *Angew. Chem., Int. Ed.* **2006**, *45* (36), 5998−6002.
(53) Tian, Z. X.; Uozumi, A.; Hamada, I.; Yanagisawa, S.; Kizaki, H.; Inagaki, K.; Morikawa, Y. First-Principles Investigation on the Segregation of Pd at $LaFe_{1-x}Pd_xO_{3-y}$ Surfaces. *Nanoscale Res. Lett.* **2013**, *8* (1), 203.
(54) Gao, Y.; Lu, Z.; You, T. L.; Wang, J.; Xie, L.; He, J.; Ciucci, F. Energetics of Nanoparticle Exsolution from Perovskite Oxides. *J. Phys. Chem. Lett.* **2018**, *9* (13), 3772−3778.
(55) Kröger, F.; Vink, H., Relations between the Concentrations of Imperfections in Crystalline Solids. *Solid State Physics*; Elsevier, 1956; Vol. 3, pp 307−435, DOI: 10.1016/S0081-1947(08)60135-6.
(56) Kwon, O.; Kim, K.; Joo, S.; Jeong, H. Y.; Shin, J.; Han, J. W.; Sengodan, S.; Kim, G. Self-Assembled Alloy Nanoparticles in a Layered Double Perovskite as a Fuel Oxidation Catalyst for Solid Oxide Fuel Cells. *J. Mater. Chem. A* **2018**, *6* (33), 15947−15953.
(57) Joo, S.; Kwon, O.; Kim, K.; Kim, S.; Kim, H.; Shin, J.; Jeong, H. Y.; Sengodan, S.; Han, J. W.; Kim, G. Cation-Swapped Homogeneous Nanoparticles in Perovskite Oxides for High Power Density. *Nat. Commun.* **2019**, *10* (1), 697.
(58) Kwon, O.; Sengodan, S.; Kim, K.; Kim, G.; Jeong, H. Y.; Shin, J.; Ju, Y. W.; Han, J. W.; Kim, G. Exsolution Trends and Co-segregation Aspects of Self-Grown Catalyst Nanoparticles in Perovskites. *Nat. Commun.* **2017**, *8*, 15967.
(59) Sun, Y. F.; Zhang, Y. Q.; Chen, J.; Li, J. H.; Zhu, Y. T.; Zeng, Y. M.; Amirkhiz, B. S.; Li, J.; Hua, B.; Luo, J. L. New Opportunity for *in Situ* Exsolution of Metallic Nanoparticles on Perovskite Parent. *Nano Lett.* **2016**, *16* (8), 5303−5309.
(60) Han, H.; Park, J.; Nam, S. Y.; Kim, K. J.; Choi, G. M.; Parkin, S. S.; Jang, H. M.; Irvine, J. T. Lattice Strain-Enhanced Exsolution of Nanoparticles in Thin Films. *Nat. Commun.* **2019**, *10* (1), 1471.
(61) Adamson, A. W.; Gast, A. P. *Physical Chemistry of Surfaces*, 2nd ed.; Interscience: New York, 1967; Vol. *150*, 180.
(62) Blander, M.; Katz, J. L. Bubble Nucleation in Liquids. *AIChE J.* **1975**, *21* (5), 833−848.
(63) Kelchner, C. L.; Plimpton, S.; Hamilton, J. Dislocation Nucleation and Defect Structure During Surface Indentation. *Phys. Rev. B: Condens. Matter Mater. Phys.* **1998**, *58* (17), 11085−11088.
(64) Buharon, M.; Singh, S.; Komarala, E. P.; Rosen, B. A. Expanding Possibilities for Solid-Phase Crystallization by Exsolving Tunable Pd-NiO Core-Shell Nanostructures. *CrystEngComm* **2018**, *20* (41), 6372−6376.
(65) Neagu, D.; Kyriakou, V.; Roiban, I. L.; Aouine, M.; Tang, C.; Caravaca, A.; Kousi, K.; Schreur-Piet, I.; Metcalfe, I. S.; Vernoux, P.; van de Sanden, M. C. M.; Tsampas, M. N. *In Situ* Observation of Nanoparticle Exsolution from Perovskite Oxides: From Atomic Scale Mechanistic Insight to Nanostructure Tailoring. *ACS Nano* **2019**, *13* (11), 12996−13005.
(66) Mebane, D. S. A Variational Approach to Surface Cation Segregation in Mixed Conducting Perovskites. *Comput. Mater. Sci.* **2015**, *103*, 231−236.
(67) Mebane, D. S.; De Souza, R. A. A Generalised Space-Charge Theory for Extended Defects in Oxygen-Ion Conducting Electrolytes: From Dilute to Concentrated Solid Solutions. *Energy Environ. Sci.* **2015**, *8* (10), 2935−2940.
(68) Tong, X.; Mebane, D. S. Kinetic Modeling of Near-Interface Defect Segregation during Thermal Annealing of Oxygen-Conducting Solid Electrolytes. *Solid State Ionics* **2017**, *299*, 78−81.
(69) Zurhelle, A. F.; Tong, X.; Klein, A.; Mebane, D. S.; De Souza, R. A. A Space-Charge Treatment of the Increased Concentration of Reactive Species at the Surface of a Ceria Solid Solution. *Angew. Chem., Int. Ed.* **2017**, *56* (46), 14516−14520.
(70) Jiang, G.; Yan, F.; Wan, S.; Zhang, Y.; Yan, M. Microstructure Evolution and Kinetics of B-Site Nanoparticle Exsolution from an A-Site-Deficient Perovskite Surface: A Phase-Field Modeling and Simulation Study. *Phys. Chem. Chem. Phys.* **2019**, *21* (21), 10902−10907.
(71) Sun, Y.; Li, J.; Zeng, Y.; Amirkhiz, B. S.; Wang, M.; Behnamian, Y.; Luo, J. A-Site Deficient Perovskite: The Parent for *in Situ* Exsolution of Highly Active, Regenerable Nano-Particles as SOFC Anodes. *J. Mater. Chem. A* **2015**, *3* (20), 11048−11056.
(72) Steiger, P.; Burnat, D.; Madi, H.; Mai, A.; Holzer, L.; Van Herle, J.; Kröcher, O.; Heel, A.; Ferri, D. Sulfur Poisoning Recovery on a Solid Oxide Fuel Cell Anode Material through Reversible Segregation of Nickel. *Chem. Mater.* **2019**, *31* (3), 748−758.
(73) Kobsiriphat, W.; Madsen, B. D.; Wang, Y.; Marks, L. D.; Barnett, S. A. $La_{0.8}Sr_{0.2}Cr_{1-x}Ru_xO_{3-\delta}$-$Gd_{0.1}Ce_{0.9}O_{1.95}$ Solid Oxide Fuel Cell Anodes: Ru Precipitation and Electrochemical Performance. *Solid State Ionics* **2009**, *180* (2), 257−264.
(74) Kim, K. J.; Han, H.; Defferriere, T.; Yoon, D.; Na, S.; Kim, S. J.; Dayaghi, A. M.; Son, J.; Oh, T.-S.; Jang, H. M.; Choi, G. M. Facet-Dependent *in Situ* Growth of Nanoparticles in Epitaxial Thin Films: the Role of Interfacial Energy. *J. Am. Chem. Soc.* **2019**, *141* (18), 7509−7517.

(75) Joo, S.; Seong, A.; Kwon, O.; Kim, K.; Lee, J. H.; Gorte, R. J.; Vohs, J. M.; Han, J. W.; Kim, G. Highly Active Dry Methane Reforming Catalysts with Boosted *in Situ* Grown Ni-Fe Nanoparticles on Perovskite *via* Atomic Layer Deposition. *Sci. Adv.* **2020**, *6* (35), No. eabb1573.
(76) Boldrin, P.; Ruiz-Trejo, E.; Mermelstein, J.; Bermudez Menendez, J. M.; Rami Rez Reina, T.; Brandon, N. P. Strategies for Carbon and Sulfur Tolerant Solid Oxide Fuel Cell Materials, Incorporating Lessons from Heterogeneous Catalysis. *Chem. Rev.* **2016**, *116* (22), 13633−13684.
(77) Cheng, Z.; Wang, J.-H.; Choi, Y.; Yang, L.; Lin, M.-C.; Liu, M. From Ni-YSZ to Sulfur-Tolerant Anode Materials for SOFCs: Electrochemical Behavior, *in Situ* Characterization, Modeling, and Future Perspectives. *Energy Environ. Sci.* **2011**, *4* (11), 4380−4409.
(78) Khzouz, M.; Wood, J.; Pollet, B.; Bujalski, W. Characterization and Activity Test of Commercial Ni/Al_2O_3, Cu/ZnO/Al_2O_3 and Prepared Ni-Cu/Al_2O_3 Catalysts for Hydrogen Production from Methane and Methanol Fuels. *Int. J. Hydrogen Energy* **2013**, *38* (3), 1664−1675.
(79) Meng, X.; Gong, X.; Yang, N.; Yin, Y.; Tan, X.; Ma, Z.-F. Carbon-Resistant Ni-YSZ/Cu-CeO_2-YSZ Dual-Layer Hollow Fiber Anode for Micro Tubular Solid Oxide Fuel Cell. *Int. J. Hydrogen Energy* **2014**, *39* (8), 3879−3886.
(80) Lu, J.; Zhu, C.; Pan, C.; Lin, W.; Lemmon, J. P.; Chen, F.; Li, C.; Xie, K. Highly Efficient Electrochemical Reforming of CH_4/CO_2 in a Solid Oxide Electrolyser. *Sci. Adv.* **2018**, *4* (3), No. eaar5100, 1−8.
(81) Li, J.; Wei, B.; Yue, X.; Lu, Z. A Highly Efficient and Robust Perovskite Anode with Iron-Palladium Co-Exsolutions for Intermediate-Temperature Solid-Oxide Fuel Cells. *ChemSusChem* **2018**, *11* (15), 2593−2603.
(82) Kang, B.; Matsuda, J.; Ishihara, T. Cu-Fe-Ni Nano Alloy Particles Obtained by Exsolution from Cu(Ni)Fe_2O_4 as Active Anode for SOFCs. *J. Mater. Chem. A* **2019**, *7* (45), 26105−26115.
(83) Wei, H.; Xie, K.; Zhang, J.; Zhang, Y.; Wang, Y.; Qin, Y.; Cui, J.; Yan, J.; Wu, Y. *In Situ* Growth of $Ni_{(x)}Cu_{(1-x)}$ Alloy Nanocatalysts on Redox-Reversible Rutile (Nb,Ti)$O_{(4)}$ towards High-Temperature Carbon Dioxide Electrolysis. *Sci. Rep.* **2015**, *4*, 5156.
(84) Wang, W.; Zhu, C.; Xie, K.; Gan, L. High Performance, Coking-Resistant and Sulfur-Tolerant Anode for Solid Oxide Fuel Cell. *J. Power Sources* **2018**, *406*, 1−6.
(85) Liu, S.; Chuang, K. T.; Luo, J.-L. Double-Layered Perovskite Anode with *in Situ* Exsolution of a Co-Fe Alloy to Cogenerate Ethylene and Electricity in a Proton-Conducting Ethane Fuel Cell. *ACS Catal.* **2016**, *6* (2), 760−768.
(86) Liu, S.; Liu, Q.; Luo, J.-L. CO_2-to-CO Conversion on Layered Perovskite with *in Situ* Exsolved Co-Fe Alloy Nanoparticles: An Active and Stable Cathode for Solid Oxide Electrolysis Cells. *J. Mater. Chem. A* **2016**, *4* (44), 17521−17528.
(87) Chen, X.; Ni, W.; Wang, J.; Zhong, Q.; Han, M.; Zhu, T. Exploration of Co-Fe Alloy Precipitation and Electrochemical Behavior Hysteresis Using Lanthanum and Cobalt Co-Substituted $SrFeO_{3-\delta}$ SOFC Anode. *Electrochim. Acta* **2018**, *277*, 226−234.
(88) Song, S.; Zhou, J.; Su, X.; Wang, Y.; Li, J.; Zhang, L.; Xiao, G.; Guan, C.; Liu, R.; Chen, S.; Lin, H.-J.; Zhang, S.; Wang, J.-Q. Operando X-Ray Spectroscopic Tracking of Self-Reconstruction for Anchored Nanoparticles as High-Performance Electrocatalysts towards Oxygen Evolution. *Energy Environ. Sci.* **2018**, *11* (10), 2945−2953.
(89) Zeng, D.; Qiu, Y.; Peng, S.; Chen, C.; Zeng, J.; Zhang, S.; Xiao, R. Enhanced Hydrogen Production Performance through Controllable Redox Exsolution within $CoFeAlO_x$ Spinel Oxygen Carrier Materials. *J. Mater. Chem. A* **2018**, *6* (24), 11306−11316.
(90) Gan, T.; Ding, G.; Zhi, X.; Fan, L.; Hou, N.; Yao, X.; Li, P.; Zhao, Y.; Li, Y. A $LaNi_{0.9}Co_{0.1}O_3$ Coated $Ce_{0.8}Sm_{0.2}O_{1.9}$ Composite Anode for Solid Oxide Fuel Cells Fed with Methanol. *Catal. Today* **2019**, *327*, 220−225.
(91) Neagu, D.; Papaioannou, E. I.; Ramli, W. K. W.; Miller, D. N.; Murdoch, B. J.; Menard, H.; Umar, A.; Barlow, A. J.; Cumpson, P. J.; Irvine, J. T. S.; Metcalfe, I. S. Demonstration of Chemistry at a Point through Restructuring and Catalytic Activation at Anchored Nanoparticles. *Nat. Commun.* **2017**, *8* (1), 1855.
(92) Sun, Y. F.; Li, J. H.; Cui, L.; Hua, B.; Cui, S. H.; Li, J.; Luo, J. L. A-Site-Deficiency Facilitated *in Situ* Growth of Bimetallic Ni-Fe Nano-Alloys: A Novel Coking-Tolerant Fuel Cell Anode Catalyst. *Nanoscale* **2015**, *7* (25), 11173−11181.
(93) Liu, S.; Liu, Q.; Luo, J.-L. Highly Stable and Efficient Catalyst with *in Situ* Exsolved Fe-Ni Alloy Nanospheres Socketed on an Oxygen Deficient Perovskite for Direct CO_2 Electrolysis. *ACS Catal.* **2016**, *6* (9), 6219−6228.
(94) Thalinger, R.; Gocyla, M.; Heggen, M.; Dunin-Borkowski, R.; Grünbacher, M.; Stöger-Pollach, M.; Schmidmair, D.; Klötzer, B.; Penner, S. Ni-Perovskite Interaction and Its Structural and Catalytic Consequences in Methane Steam Reforming and Methanation Reactions. *J. Catal.* **2016**, *337*, 26−35.
(95) Li, J.; Yu, Y.; Yin, Y.-M.; Zhou, N.; Ma, Z.-F. A Novel High Performance Composite Anode with *in Situ* Growth of Fe-Ni Alloy Nanoparticles for Intermediate Solid Oxide Fuel Cells. *Electrochim. Acta* **2017**, *235*, 317−322.
(96) Zubenko, D.; Singh, S.; Rosen, B. A. Exsolution of Re-Alloy Catalysts with Enhanced Stability for Methane Dry Reforming. *Appl. Catal., B* **2017**, *209*, 711−719.
(97) Lo Faro, M.; Reis, R. M.; Saglietti, G. G. A.; Oliveira, V. L.; Zignani, S. C.; Trocino, S.; Maisano, S.; Ticianelli, E. A.; Hodnik, N.; Ruiz-Zepeda, F.; Aricò, A. S. Solid Oxide Fuel Cells Fed with Dry Ethanol: The Effect of a Perovskite Protective Anodic Layer Containing Dispersed Ni-Alloy @ FeO_x Core-Shell Nanoparticles. *Appl. Catal., B* **2018**, *220*, 98−110.
(98) Wang, Y.; Lei, X.; Zhang, Y.; Chen, F.; Liu, T. *In Situ* Growth of Metallic Nanoparticles on Perovskite Parent as a Hydrogen Electrode for Solid Oxide Cells. *J. Power Sources* **2018**, *405*, 114−123.
(99) Gao, Y.; Wang, J.; Lyu, Y.-Q.; Lam, K.; Ciucci, F. *In Situ* Growth of Pt_3Ni Nanoparticles on an A-Site Deficient Perovskite with Enhanced Activity for the Oxygen Reduction Reaction. *J. Mater. Chem. A* **2017**, *5* (14), 6399−6404.
(100) Arandiyan, H.; Wang, Y.; Scott, J.; Mesgari, S.; Dai, H.; Amal, R. *In Situ* Exsolution of Bimetallic Rh-Ni Nanoalloys: a Highly Efficient Catalyst for CO_2 Methanation. *ACS Appl. Mater. Interfaces* **2018**, *10* (19), 16352−16357.
(101) Glaser, R.; Zhu, T.; Troiani, H.; Caneiro, A.; Mogni, L.; Barnett, S. The Enhanced Electrochemical Response of Sr-$(Ti_{0.3}Fe_{0.7}Ru_{0.07})O_{3-\delta}$ Anodes Due to Exsolved Ru-Fe Nanoparticles. *J. Mater. Chem. A* **2018**, *6* (12), 5193−5201.
(102) Choi, Y. M.; Compson, C.; Lin, M. C.; Liu, M. *Ab Initio* Analysis of Sulfur Tolerance of Ni, Cu, and Ni-Cu Alloys for Solid Oxide Fuel Cells. *J. Alloys Compd.* **2007**, *427* (1), 25−29.
(103) Lai, K.-Y.; Manthiram, A. Evolution of Exsolved Nanoparticles on a Perovskite Oxide Surface during a Redox Process. *Chem. Mater.* **2018**, *30* (8), 2838−2847.
(104) Lei, Z.; Wang, T.; Zhao, B.; Cai, W.; Liu, Y.; Jiao, S.; Li, Q.; Cao, R.; Liu, M. Recent Progress in Electrocatalysts for Acidic Water Oxidation. *Adv. Energy Mater.* **2020**, *10*, 2000478.
(105) Hwang, J.; Rao, R. R.; Giordano, L.; Katayama, Y.; Yu, Y.; Shao-Horn, Y. Perovskites in Catalysis and Electrocatalysis. *Science* **2017**, *358* (6364), 751−756.
(106) Suntivich, J.; Gasteiger, H. A.; Yabuuchi, N.; Nakanishi, H.; Goodenough, J. B.; Shao-Horn, Y. Design Principles for Oxygen-Reduction Activity on Perovskite Oxide Catalysts for Fuel Cells and Metal-Air Batteries. *Nat. Chem.* **2011**, *3* (7), 546−550.
(107) Suntivich, J.; May, K. J.; Gasteiger, H. A.; Goodenough, J. B.; Shao-Horn, Y. A Perovskite Oxide Optimized for Oxygen Evolution Catalysis from Molecular Orbital Principles. *Science* **2011**, *334* (6061), 1383−1385.
(108) Kibsgaard, J.; Tsai, C.; Chan, K.; Benck, J. D.; Nørskov, J. K.; Abild-Pedersen, F.; Jaramillo, T. F. Designing an Improved Transition Metal Phosphide Catalyst for Hydrogen Evolution Using Experimental and Theoretical Trends. *Energy Environ. Sci.* **2015**, *8* (10), 3022−3029.

https://dx.doi.org/10.1021/acsnano.0c07105
ACS Nano 2021, 15, 81−110

(109) Wang, T.; Wu, L.; Xu, X.; Sun, Y.; Wang, Y.; Zhong, W.; Du, Y. An Efficient Co_3S_4/CoP Hybrid Catalyst for Electrocatalytic Hydrogen Evolution. *Sci. Rep.* **2017**, *7* (1), 11891.
(110) Zhu, Y.; Dai, J.; Zhou, W.; Zhong, Y.; Wang, H.; Shao, Z. Synergistically Enhanced Hydrogen Evolution Electrocatalysis by *in Situ* Exsolution of Metallic Nanoparticles on Perovskites. *J. Mater. Chem. A* **2018**, *6* (28), 13582−13587.
(111) Jiang, Y.; Geng, Z.; Yuan, L.; Sun, Y.; Cong, Y.; Huang, K.; Wang, L.; Zhang, W. Nanoscale Architecture of RuO_2/$La_{0.9}Fe_{0.92}Ru_{0.08-x}O_{3-\delta}$ Composite *via* Manipulating the Exsolution of Low Ru-Substituted A-Site Deficient Perovskite. *ACS Sustainable Chem. Eng.* **2018**, *6* (9), 11999−12005.
(112) Wang, Y.; Wang, Z.; Jin, C.; Li, C.; Li, X.; Li, Y.; Yang, R.; Liu, M. Enhanced Overall Water Electrolysis on a Bifunctional Perovskite Oxide through Interfacial Engineering. *Electrochim. Acta* **2019**, *318*, 120−129.
(113) Zhang, Y.-Q.; Tao, H.-B.; Chen, Z.; Li, M.; Sun, Y.-F.; Hua, B.; Luo, J.-L. *In Situ* Grown Cobalt Phosphide (CoP) on Perovskite Nanofibers as an Optimized Trifunctional Electrocatalyst for Zn-Air Batteries and Overall Water Splitting. *J. Mater. Chem. A* **2019**, *7* (46), 26607−26617.
(114) Tang, C.; Cheng, N.; Pu, Z.; Xing, W.; Sun, X. NiSe Nanowire Film Supported on Nickel Foam: An Efficient and Stable 3D Bifunctional Electrode for Full Water Splitting. *Angew. Chem., Int. Ed.* **2015**, *54* (32), 9351−9355.
(115) Hargreaves, J. Heterogeneous Catalysis with Metal Nitrides. *Coord. Chem. Rev.* **2013**, *257* (13−14), 2015−2031.
(116) Hargreaves, J. Nitrides as Ammonia Synthesis Catalysts and as Potential Nitrogen Transfer Reagents. *Appl. Petrochem. Res.* **2014**, *4* (1), 3−10.
(117) Abghoui, Y.; Skúlasson, E. Transition Metal Nitride Catalysts for Electrochemical Reduction of Nitrogen to Ammonia at Ambient Conditions. *Procedia Comput. Sci.* **2015**, *51*, 1897−1906.
(118) Chai, Y.; Fu, Y.; Feng, H.; Kong, W.; Yuan, C.; Pan, B.; Zhang, J.; Sun, Y. A Nickel-Based Perovskite Catalyst with a Bimodal Size Distribution of Nickel Particles for Dry Reforming of Methane. *ChemCatChem* **2018**, *10* (9), 2078−2086.
(119) Fang, F.; Feng, N.; Zhao, P.; Chen, C.; Li, X.; Meng, J.; Liu, G.; Chen, L.; Wan, H.; Guan, G. *In Situ* Exsolution of Co/CoO_x Core-Shell Nanoparticles on Double Perovskite Porous Nanotubular Webs: A Synergistically Active Catalyst for Soot Efficient Oxidation. *Chem. Eng. J.* **2019**, *372*, 752−764.
(120) Agüero, F. N.; Beltrán, A. M.; Fernández, M. A.; Cadús, L. E. Surface Nickel Particles Generated by Exsolution from a Perovskite Structure. *J. Solid State Chem.* **2019**, *273*, 75−80.
(121) Ben Mya, O.; dos Santos-Gómez, L.; Porras-Vázquez, J. M.; Omari, M.; Ramos-Barrado, J. R.; Marrero-López, D. $La_{1-x}Sr_xFe_{0.7}Ni_{0.3}O_{3-\delta}$ as Both Cathode and Anode Materials for Solid Oxide Fuel Cells. *Int. J. Hydrogen Energy* **2017**, *42* (36), 23160−23169.
(122) Bian, L.; Duan, C.; Wang, L.; Zhu, L.; O'Hayre, R.; Chou, K.-C. Electrochemical Performance and Stability of $La_{0.5}Sr_{0.5}Fe_{0.9}Nb_{0.1}O_{3-\delta}$ Symmetric Electrode for Solid Oxide Fuel Cells. *J. Power Sources* **2018**, *399*, 398−405.
(123) Chen, M.; Hu, Y.; Chen, D.; Hu, H.; Xu, Q. A Novel Anode for Solid Oxide Fuel Cells Prepared from Phase Conversion of $La_{0.3}Sr_{0.7}Fe_{0.7}Cr_{0.3}O_{3-\delta}$ Perovskite under Humid Hydrogen. *Electrochim. Acta* **2018**, *284*, 303−313.
(124) Chung, Y. S.; Kim, T.; Shin, T. H.; Yoon, H.; Park, S.; Sammes, N. M.; Kim, W. B.; Chung, J. S. *In Situ* Preparation of a $La_{1.2}Sr_{0.8}Mn_{0.4}Fe_{0.6}O_4$ Ruddlesden-Popper Phase with Exsolved Fe Nanoparticles as an Anode for SOFCs. *J. Mater. Chem. A* **2017**, *5* (14), 6437−6446.
(125) Ding, X.; Liu, H.; Gao, Z.; Hua, G.; Wang, L.; Ding, L.; Yuan, G. $La_{0.6}Ca_{0.4}Fe_{0.8}Ni_{0.2}O_{3-\delta}$ - $Sm_{0.2}Ce_{0.8}O_{1.9}$ Composites As Symmetrical Bi-Electrodes for Solid Oxide Fuel Cells through Infiltration and *in Situ* Exsolution. *Int. J. Hydrogen Energy* **2017**, *42* (39), 24968−24977.
(126) Duan, C.; Kee, R. J.; Zhu, H.; Karakaya, C.; Chen, Y.; Ricote, S.; Jarry, A.; Crumlin, E. J.; Hook, D.; Braun, R.; Sullivan, N. P.; O'Hayre, R. Highly Durable, Coking and Sulfur Tolerant, Fuel-Flexible Protonic Ceramic Fuel Cells. *Nature* **2018**, *557* (7704), 217−222.
(127) Feng, J.; Qiao, J.; Wang, W.; Wang, Z.; Sun, W.; Sun, K. Development and Performance of Anode Material Based on A-Site Deficient $Sr_{2-x}Fe_{1.4}Ni_{0.1}Mo_{0.5}O_{6-\delta}$ Perovskites for Solid Oxide Fuel cells. *Electrochim. Acta* **2016**, *215*, 592−599.
(128) Song, Y.; Ozdemir, E.; Ramesh, S.; Adishev, A.; Subramanian, S.; Harale, A.; Albuali, M.; Fadhel, B. A.; Jamal, A.; Moon, D.; Choi, S. H.; Yavuz, C. T. Dry Reforming of Methane by Stable Ni-Mo Nanocatalysts on Single-Crystalline MgO. *Science* **2020**, *367* (6479), 777−781.
(129) Tan, J.; Lee, D.; Ahn, J.; Kim, B.; Kim, J.; Moon, J. Thermally Driven *in Situ* Exsolution of Ni Nanoparticles from (Ni, Gd)CeO_2 for High-Performance Solid Oxide Fuel Cells. *J. Mater. Chem. A* **2018**, *6* (37), 18133−18142.
(130) Onn, T. M.; Monai, M.; Dai, S.; Fonda, E.; Montini, T.; Pan, X.; Graham, G. W.; Fornasiero, P.; Gorte, R. J. Smart Pd Catalyst with Improved Thermal Stability Supported on High-Surface-Area $LaFeO_3$ Prepared by Atomic Layer Deposition. *J. Am. Chem. Soc.* **2018**, *140* (14), 4841−4848.
(131) Lin, C.; Jang, J. B.; Zhang, L.; Stach, E. A.; Gorte, R. J. Improved Coking Resistance of "Intelligent" Ni Catalysts Prepared by Atomic Layer Deposition. *ACS Catal.* **2018**, *8* (8), 7679−7687.
(132) Lin, C.; Foucher, A. C.; Ji, Y.; Curran, C. D.; Stach, E. A.; McIntosh, S.; Gorte, R. J. Intelligent" Pt Catalysts Studied on High-Surface-Area $CaTiO_3$ Films. *ACS Catal.* **2019**, *9* (8), 7318−7327.
(133) Mao, X.; Foucher, A. C.; Stach, E. A.; Gorte, R. J. Intelligent" Pt Catalysts Based on Thin $LaCoO_3$ Films Prepared by Atomic Layer Deposition. *Inorganics* **2019**, *7* (9), 113.
(134) Zhou, W.; Shao, Z.; Liang, F.; Chen, Z.-G.; Zhu, Z.; Jin, W.; Xu, N. A New Cathode for Solid Oxide Fuel Cells Capable of *in Situ* Electrochemical Regeneration. *J. Mater. Chem.* **2011**, *21* (39), 15343−15351.
(135) Chen, M.; Chen, D.; Wang, K.; Xu, Q. Densification and Electrical Conducting Behavior of $BaZr_{0.9}Y_{0.1}O_{3-\delta}$ Proton Conducting Ceramics with NiO Additive. *J. Alloys Compd.* **2019**, *781*, 857−865.
(136) Kousi, K.; Neagu, D.; Bekris, L.; Papaioannou, E. I.; Metcalfe, I. S. Endogenous Nanoparticles Strain Perovskite Host Lattice Providing Oxygen Capacity and Driving Oxygen Exchange and CH_4 Conversion to Syngas. *Angew. Chem., Int. Ed.* **2020**, *59* (6), 2510−2519.
(137) Zhang, X.; Pei, C.; Chang, X.; Chen, S.; Liu, R.; Zhao, Z.-J.; Mu, R.; Gong, J. FeO_6 Octahedral Distortion Activates Lattice Oxygen in Perovskite Ferrite for Methane Partial Oxidation Coupled with CO_2-Splitting. *J. Am. Chem. Soc.* **2020**, *142* (26), 11540−11549.
(138) Carrillo, A. J.; Kim, K. J.; Hood, Z. D.; Bork, A. H.; Rupp, J. L. $La_{0.6}Sr_{0.4}Cr_{0.8}Co_{0.2}O_3$ Perovskite Decorated with Exsolved Co Nanoparticles for Stable CO_2 Splitting and Syngas Production. *ACS Appl. Energy Mater.* **2020**, *3* (5), 4569−4579.
(139) Beschnitt, S.; De Souza, R. A. Impurity Diffusion of Hf and Zr in Gd-Doped CeO_2. *Solid State Ionics* **2017**, *305*, 23−29.
(140) Harvey, S. P.; De Souza, R. A.; Martin, M. Diffusion of La and Mn in $Ba_{0.5}$ $Sr_{0.5}Co_{0.8}Fe_{0.2}O_{3-\delta}$ Polycrystalline Ceramics. *Energy Environ. Sci.* **2012**, *5* (2), 5803−5813.
(141) Mao, X.; Foucher, A. C.; Montini, T.; Stach, E. A.; Fornasiero, P.; Gorte, R. J. Epitaxial and Strong Support Interactions between Pt and $LaFeO_3$ Films Stabilize Pt Dispersion. *J. Am. Chem. Soc.* **2020**, *142* (23), 10373−10382.
(142) Song, Y.; Chen, Y.; Wang, W.; Zhou, C.; Zhong, Y.; Yang, G.; Zhou, W.; Liu, M.; Shao, Z. Self-Assembled Triple-Conducting Nanocomposite as a Superior Protonic Ceramic Fuel Cell Cathode. *Joule* **2019**, *3* (11), 2842−2853.
(143) Kim, J. H.; Kim, J. K.; Seo, H. G.; Lim, D. K.; Jeong, S. J.; Seo, J.; Kim, J.; Jung, W. Ex-Solved Ag Nanocatalysts on a Sr-Free Parent Scaffold Authorize a Highly Efficient Route of Oxygen Reduction. *Adv. Funct. Mater.* **2020**, *30*, 2001326 1−9.

https://dx.doi.org/10.1021/acsnano.0c07105
ACS Nano 2021, 15, 81−110

(144) Keav, S.; Matam, S. K.; Ferri, D.; Weidenkaff, A. Structured Perovskite-Based Catalysts and Their Application as Three-Way Catalytic Converters—A Review. *Catalysts* **2014**, *4* (3), 226−255.
(145) Cremers, V.; Puurunen, R. L.; Dendooven, J. Conformality in Atomic Layer Deposition: Current Status Overview of Analysis and Modelling. *Appl. Phys. Rev.* **2019**, *6* (2), 021302.
(146) Joo, S.; Kwon, O.; Kim, S.; Jeong, H. Y.; Kim, G. Ni-Fe Bimetallic Nanocatalysts Produced by Topotactic Exsolution in Fe Deposited $PrBaMn_{1.7}Ni_{0.3}O_{5+\delta}$ for Dry Reforming of Methane. *J. Electrochem. Soc.* **2020**, *167* (6), 064518.
(147) Ding, D.; Li, X.; Lai, S. Y.; Gerdes, K.; Liu, M. Enhancing SOFC Cathode Performance by Surface Modification through Infiltration. *Energy Environ. Sci.* **2014**, *7* (2), 552−575.
(148) Wan Ramli, W. K.; Papaioannou, E.; Naegu, D.; Metcalfe, I. S. Exsolution of Nickel Alloys Anchored Nanoparticles on Perovskite Oxides for CO Oxidation. *IOP Conf. Ser.: Mater. Sci. Eng.* **2020**, *778*, 012059.
(149) Yin, Y.; Rioux, R. M.; Erdonmez, C. K.; Hughes, S.; Somorjai, G. A.; Alivisatos, A. P. Formation of Hollow Nanocrystals through the Nanoscale Kirkendall Effect. *Science* **2004**, *304* (5671), 711−714.
(150) Ha, D.-H.; Moreau, L. M.; Honrao, S.; Hennig, R. G.; Robinson, R. D. The Oxidation of Cobalt Nanoparticles into Kirkendall-Hollowed CoO and Co_3O_4: The Diffusion Mechanisms and Atomic Structural Transformations. *J. Phys. Chem. C* **2013**, *117* (27), 14303−14312.
(151) Wang, H.; Liang, Z.; Tang, M.; Chen, G.; Li, Y.; Chen, W.; Lin, D.; Zhang, Z.; Zhou, G.; Li, J.; et al. Self-Selective Catalyst Synthesis for CO_2 Reduction. *Joule* **2019**, *3* (8), 1927−1936.
(152) Jang, J. S.; Kim, J. K.; Kim, K.; Jung, W. G.; Lim, C.; Kim, S.; Kim, D. H.; Kim, B. J.; Han, J. W.; Jung, W.; Kim, I.-D. Dopant-Driven Positive Reinforcement in Ex-Solution Process: New Strategy to Develop Highly Capable and Durable Catalytic Materials. *Adv. Mater.* **2020**, *32*, 2003983 1−9.
(153) Sun, Y.-F.; Zhang, Y.-Q.; Chen, J.; Li, J.-H.; Zhu, Y.-T.; Zeng, Y.-M.; Amirkhiz, B. S.; Li, J.; Hua, B.; Luo, J.-L. New Opportunity for *in Situ* Exsolution of Metallic Nanoparticles on Perovskite Parent. *Nano Lett.* **2016**, *16* (8), 5303−5309.
(154) Lee, Y.-L.; Kleis, J.; Rossmeisl, J.; Shao-Horn, Y.; Morgan, D. Prediction of Solid Oxide Fuel Cell Cathode Activity with First-Principles Descriptors. *Energy Environ. Sci.* **2011**, *4* (10), 3966−3970.
(155) Jacobs, R.; Hwang, J.; Shao-Horn, Y.; Morgan, D. Assessing Correlations of Perovskite Catalytic Performance with Electronic Structure Descriptors. *Chem. Mater.* **2019**, *31* (3), 785−797.
(156) Jain, A.; Ong, S. P.; Hautier, G.; Chen, W.; Richards, W. D.; Dacek, S.; Cholia, S.; Gunter, D.; Skinner, D.; Ceder, G.; Persson, K. A. Commentary: The Materials Project: A Materials Genome Approach to Accelerating Materials Innovation. *APL Mater.* **2013**, *1* (1), 011002 1−11.
(157) Saal, J. E.; Kirklin, S.; Aykol, M.; Meredig, B.; Wolverton, C. Materials Design and Discovery with High-Throughput Density Functional Theory: The Open Quantum Materials Database (OQMD). *JOM* **2013**, *65* (11), 1501−1509.
(158) Xie, T.; Grossman, J. C. Crystal Graph Convolutional Neural Networks for an Accurate and Interpretable Prediction of Material Properties. *Phys. Rev. Lett.* **2018**, *120* (14), 145301.
(159) Park, C. W.; Wolverton, C. Developing an Improved Crystal Graph Convolutional Neural Network Framework for Accelerated Materials Discovery. *Phys. Rev. Mater.* **2020**, *4* (6), 063801.
(160) Schütt, K. T.; Sauceda, H. E.; Kindermans, P. J.; Tkatchenko, A.; Müller, K. R. SchNet - A Deep Learning Architecture for Molecules and Materials. *J. Chem. Phys.* **2018**, *148* (24), 241722.
(161) Chen, C.; Ye, W.; Zuo, Y.; Zheng, C.; Ong, S. P. Graph Networks as a Universal Machine Learning Framework for Molecules and Crystals. *Chem. Mater.* **2019**, *31* (9), 3564−3572.
(162) Behler, J.; Parrinello, M. Generalized Neural-Network Representation of High-Dimensional Potential-Energy Surfaces. *Phys. Rev. Lett.* **2007**, *98* (14), 146401.
(163) Jinnouchi, R.; Karsai, F.; Kresse, G. On-The-Fly Machine Learning Force Field Generation: Application to Melting Points. *Phys. Rev. B: Condens. Matter Mater. Phys.* **2019**, *100* (1), 014105.
(164) Seko, A.; Takahashi, A.; Tanaka, I. Sparse Representation for a Potential Energy Surface. *Phys. Rev. B: Condens. Matter Mater. Phys.* **2014**, *90* (2), 024101.
(165) Greenwood, M.; Provatas, N.; Rottler, J. Free Energy Functionals for Efficient Phase Field Crystal Modeling of Structural Phase Transformations. *Phys. Rev. Lett.* **2010**, *105* (4), 045702.
(166) Abdulle, A.; Weinan, E.; Engquist, B.; Vanden-Eijnden, E. The Heterogeneous Multiscale Method. *Acta Numer.* **2012**, *21*, 1−87.
(167) E, W.; Ren, W.; Vanden-Eijnden, E. A General Strategy for Designing Seamless Multiscale Methods. *J. Comput. Phys.* **2009**, *228* (15), 5437−5453.
(168) Wu, K.-A.; Adland, A.; Karma, A. Phase-Field-Crystal Model for FCC Ordering. *Phys. Rev. E* **2010**, *81* (6), 061601.
(169) Emmerich, H.; Löwen, H.; Wittkowski, R.; Gruhn, T.; Tóth, G. I.; Tegze, G.; Gránásy, L. Phase-Field-Crystal Models for Condensed Matter Dynamics on Atomic Length and Diffusive Time Scales: An Overview. *Adv. Phys.* **2012**, *61* (6), 665−743.
(170) Jaatinen, A.; Achim, C. V.; Elder, K. R.; Ala-Nissila, T. Thermodynamics of BCC Metals in Phase-Field-Crystal Models. *Phys. Rev. E* **2009**, *80* (3), 031602.
(171) Elder, K. R.; Provatas, N.; Berry, J.; Stefanovic, P.; Grant, M. Phase-Field Crystal Modeling and Classical Density Functional Theory of Freezing. *Phys. Rev. B: Condens. Matter Mater. Phys.* **2007**, *75* (6), 064107.
(172) Zhang, J.; Poulsen, S. O.; Gibbs, J. W.; Voorhees, P. W.; Poulsen, H. F. Determining Material Parameters Using Phase-Field Simulations and Experiments. *Acta Mater.* **2017**, *129*, 229−238.
(173) Zhu, Y.; Zhou, W.; Ran, R.; Chen, Y.; Shao, Z.; Liu, M. Promotion of Oxygen Reduction by Exsolved Silver Nanoparticles on a Perovskite Scaffold for Low-Temperature Solid Oxide Fuel Cells. *Nano Lett.* **2016**, *16* (1), 512−518.

https://dx.doi.org/10.1021/acsnano.0c07105
ACS Nano 2021, 15, 81−110